

**Monte Carlo calculation of volumetric modulated arc therapy  
and helical tomotherapy dose distributions for stereotactic  
ablative radiotherapy lung treatments**

by

Jason Bélec

B.Sc. (University of Ottawa) 2002

M.Sc. (McGill University) 2004

A thesis submitted to the  
Faculty of Graduate and Postdoctoral Affairs  
in partial fulfillment of the requirements  
for the degree of

Doctor of Philosophy

in

Physics

Ottawa-Carleton Institute for Physics  
Department of Physics, Carleton University  
Ottawa, Ontario

Copyright © 2012, Jason Bélec



Library and Archives  
Canada

Published Heritage  
Branch

395 Wellington Street  
Ottawa ON K1A 0N4  
Canada

Bibliothèque et  
Archives Canada

Direction du  
Patrimoine de l'édition

395, rue Wellington  
Ottawa ON K1A 0N4  
Canada

*Your file Votre référence*

*ISBN: 978-0-494-93664-1*

*Our file Notre référence*

*ISBN: 978-0-494-93664-1*

#### NOTICE:

The author has granted a non-exclusive license allowing Library and Archives Canada to reproduce, publish, archive, preserve, conserve, communicate to the public by telecommunication or on the Internet, loan, distribute and sell theses worldwide, for commercial or non-commercial purposes, in microform, paper, electronic and/or any other formats.

The author retains copyright ownership and moral rights in this thesis. Neither the thesis nor substantial extracts from it may be printed or otherwise reproduced without the author's permission.

#### AVIS:

L'auteur a accordé une licence non exclusive permettant à la Bibliothèque et Archives Canada de reproduire, publier, archiver, sauvegarder, conserver, transmettre au public par télécommunication ou par l'Internet, prêter, distribuer et vendre des thèses partout dans le monde, à des fins commerciales ou autres, sur support microforme, papier, électronique et/ou autres formats.

L'auteur conserve la propriété du droit d'auteur et des droits moraux qui protègent cette thèse. Ni la thèse ni des extraits substantiels de celle-ci ne doivent être imprimés ou autrement reproduits sans son autorisation.

---

In compliance with the Canadian Privacy Act some supporting forms may have been removed from this thesis.

While these forms may be included in the document page count, their removal does not represent any loss of content from the thesis.

Conformément à la loi canadienne sur la protection de la vie privée, quelques formulaires secondaires ont été enlevés de cette thèse.

Bien que ces formulaires aient inclus dans la pagination, il n'y aura aucun contenu manquant.

Canada

## Abstract

The aim of this study was to calculate realistic dose distributions that include the continuous deformation of organs and motion of treatment units using four dimensional Monte Carlo methods for both volumetric modulated arc therapy and helical tomotherapy stereotactic ablative radiotherapy lung treatments.

We present a method to perform position-probability-sampled Monte Carlo dose calculations in the BEAMnrc and DOSXZYnrc user codes of EGSnrc. The method includes full accelerator head simulation of conventional and helical tomotherapy treatment units and a realistic representation of machine continuous motion via the sampling of a time variable. The method simplifies the simulation process, improves the dose calculation accuracy and involves an acceptably small change in computation time. Absolute dose agreement for static fields between Monte Carlo calculations and measurements is within 2 % / 1 mm. Absolute dose agreement between Monte Carlo and treatment planning system for four types of treatment techniques (3D-conformal radiotherapy, step-shoot intensity modulation radiotherapy, helical tomotherapy and volumetric modulated arc therapy) was determined to be within 3 % / 3 mm.

We also present a method to modify the DOSXYZnrc user code to account for the continuous intra-fraction deformation of the patient geometry. We implemented two methods in the user code (density interpolation, density mapping) to update the patient geometry (transport grid densities) as a function of time and two methods (voxel average, voxel center) to map back the energy deposited in the time dependant transport grid to a reference grid. We also provide examples of mathematical phantom tests and experimental measurements used to validate the implementation of these methods.

Finally, we present an example of the application of the method for stereotactic ablative radiotherapy lung treatments with intra-fraction motion. The results show that breathing motion is appropriately addressed with the internal target volume method for the cases studied. For both helical tomotherapy and volumetric modulated arc therapy stereotactic ablative radiotherapy lung treatments, the impact of interplay effects for prescription doses of 54 Gy or 60 Gy resulted in a change of the target dose volume histogram of less than 2 Gy scored at 10 % and 90% of the volume.

## Acknowledgements

The research for this thesis was performed under the auspices of the Carleton University Physics Department and the Ottawa Hospital Cancer Center Medical Physics Department. I would like to express my gratitude to my supervisor, Dr Brenda Clark, for her continued guidance, support and encouragement throughout this project. I would also like to thank several Carleton University physics professors (Dr Paul Johns, Dr Gerald Oakham and Dr Manuella Vincter) for teaching me about physics and striving to get the best out of their students.

I would like to thank Blake Walters and Ali Elsayed for very helpful discussion regarding the BEAMnrc and DOSXYZnrc user codes, Jason Smale and Dr Jason Pantarotto for useful discussion, Dr Dave Rogers for allowing access to the physics computation cluster and G. Wilson for supplying the iCom listening software. I also acknowledge Elekta AB for funding this work and supplying technical details used in the accelerator modeling. I would also like to thank the entire medical physics staff at the Ottawa Hospital Cancer Center who have always been eager to help. In particular, I am grateful to Dr Nicolas Ploquin and Dr Dan La Russa whose assistance was important.

Last, but not least, I must thank my parents, Suzanne and Yvon, for their continuous encouragements and support. I also want to thank the love of my life, Isabelle, for all the support she has given me over the past few years. Finally, I also thank my three beautiful children (Loic, Anne-Sophie and Elliot) for the long sleepless nights.

## **Statement of originality**

This thesis describes the results of the author's research conducted primarily at the Ottawa Hospital Cancer Centre during the course of the Ph.D. program of Carleton University. Most of these results have been published or submitted in either the *Medical Physics* or *Physics in Medicine and Biology* journals, and have been presented at both national and international conferences. The details of where the results of these publications may be found in the thesis, together with the author's contributions, are provided below:

### PAPER I:

➔ J. Belec, N. Ploquin, D. J. La Russa, B. G. Clark: Position-probability-sampled Monte Carlo calculation of VMAT, 3DCRT, step-shoot IMRT, and helical tomotherapy dose distributions using BEAMnrc/DOSXYZnrc *Med. Phys.* 38, 948 (2011)

➔ The results of this paper constitute a part of Chapter 2 which discusses Monte Carlo modeling of accelerator head and external beam radiation treatment delivery. The author performed all of the work, prepared the manuscript for publication, and made the necessary revisions following the review process, all under the supervision of Dr. Brenda Clark. The results from this paper were also presented by the author at the 2010 COMP conference (oral presentation). Dr N. Ploquin provided assistance with the use of the Monaco treatment planning system and Dr D. J. La Russa provided assistance with the compilation of the BEAMnrc / DOSXYZnrc shared library mode.

PAPER II:

➔ (submitted) J. Belec, B. G. Clark: Monte Carlo calculation of VMAT and helical tomotherapy dose distributions for lung stereotactic treatments with intra-fraction motion

Phys. Med. Biol. (2012)

➔ The results of this paper constitute a part of Chapter 3 and Chapter 4 which discusses Monte Carlo modeling of patient deformation. The author performed all of the measurements and prepared the manuscript for publication under the supervision of Dr. Brenda Clark. The results from this paper were also presented by the author at the 2011 AAPM conference (oral presentation).

## **Table of Contents**

Abstract.....	ii
Acknowledgements.....	iv
Statement of originality.....	v
Table of Contents.....	vii
List of Tables.....	ix
List of figures.....	x
Abbreviations.....	xviii
1 Background.....	1
1.1 Introduction.....	1
1.2 Radiation therapy.....	1
1.3 Treatment delivery.....	2
1.3.1 Conventional treatment unit.....	2
1.3.2 Helical tomotherapy treatment unit.....	4
1.3.3 Robotic treatment unit.....	7
1.4 Dose distributions.....	9
1.4.1 Representation of dose distributions.....	9
1.4.2 Measurements of dose distributions.....	12
1.4.3 Calculations of dose distributions.....	25
1.5 Stereotactic ablative radiotherapy (SABR) lung treatment.....	34
1.6 Patient motion.....	38
1.6.1 Setup motion.....	38
1.6.2 Image registration.....	39
1.6.3 Respiratory motion.....	43
1.7 Thesis outline.....	49
2 Treatment unit modeling.....	52
2.1 Introduction.....	52
2.2 Materials and method.....	56
2.2.1 Modifications to BEAMnrc/DOSXYZnrc.....	56
2.2.2 User interface.....	59
2.2.3 Monte Carlo model of a conventional treatment unit.....	64
2.2.4 Monte Carlo model of a HT treatment unit.....	68
2.2.5 Measurements for validating the Monte Carlo models.....	73
2.2.6 Treatment planning systems.....	74
2.3 Results.....	75
2.3.1 Modifications to BEAMnrc/DOSXYZnrc.....	75
2.3.2 Validation of the MC model of a conventional treatment unit.....	77
2.3.3 Validation of the MC model of a HT treatment unit.....	88
2.3.4 Testing the MC model of a conventional treatment unit.....	93
2.3.5 Testing the MC model of a HT treatment unit.....	97
2.4 Discussion.....	100
2.5 Conclusion.....	104
3 Patient modeling.....	106
3.1 Introduction.....	106
3.2 Materials and methods.....	106

3.2.1	Patient geometry .....	106
3.2.2	Registration of energy deposition .....	115
3.2.3	Validation.....	121
3.3	Results.....	127
3.4	Discussion.....	128
3.5	Conclusion .....	132
4	SABR lung treatment planning study .....	134
4.1	Introduction.....	134
4.2	Materials and method.....	135
4.3	Results and Discussion .....	136
4.4	Discussion and conclusion.....	140
5	Summary .....	149
6	References.....	152

## **List of Tables**

Table 1 Effective atomic number $Z_{\text{eff}}$ , number of electrons per gram $\rho_e$ and mass density $\rho_m$ of the phantom materials (Kron, 1999).....	24
Table 2 Overview of patient characteristics used to study the impact of intra-fraction motion in SABR lung treatments. The tumour-isocentre distance is specific to helical tomotherapy and represents the distance between the machine isocenter (center of a transverse CT image) and the location of the tumor center (GTV centroid). A larger tumor-isocentre distance increase the impact of gantry angle discretization as explained in figure 2.11. (Source: Paper II) .....	137

## **List of Figures**

Figure 1.1 Image of a conventional treatment unit –Elekta Synergy- (left) with a multi-leaf collimator (right). .....	3
Figure 1.2 Example of tomotherapy multi-leaf collimator sinogram. The rows show the leaf numbers and the columns show the projection numbers. The color intensity shows the leaf open time. ....	5
Figure 1.3 Illustration of an MLC sinogram with 4 leaves and 1 projection. The gray value represents the open time. The top leaf has a higher open time than the bottom leaf. The open times are centered about the mid-point of each projection so the top leaf will be the first one to be opened and the last one to be closed. ....	6
Figure 1.4 Image of an helical tomotherapy treatment unit (left) with a binary multi-leaf collimator (right). ....	7
Figure 1.5 Image of a robotic treatment unit (left) with an iris collimator (right). ....	9
Figure 1.6 Inplane and crossplane off-axis ratio profiles are respectively defined as perpendicular and parallel to the leaf side. ....	11
Figure 1.7 Schematic representation of electron and photon fluences at 5 cm depth in a large field size for an incident megavoltage photon beam. Lateral equilibrium is established in the central portion of the field. The fluences is shown separately for electrons having motion components towards the left and the right side of the profile. ..	15
Figure 1.8 Schematic representation of the photon and electron fluences at 5 cm depth in a small field size for an incident megavoltage photon beam. Lateral equilibrium is not established in the central portion of the field. The fluences are shown separately for electrons having motion components towards the left and the right side of the profile. ..	15
Figure 1.9 Schematic representation of off-axis ratio (OAR) profile volume averaging. The OAR profile shown is for illustration purposes and is approximated as a Gaussian function. The profile with volume averaging was calculated by convolving the OAR profile with a square function. ....	17
Figure 1.10 On the left, mass energy absorption coefficient ratio for the various detector materials used in this work. The photon energy spectrum of a 10x10 cm <sup>2</sup> field size for a 6 MV photon beam is also plotted for comparison. On the right, restricted mass stopping power ratio for the various detector materials used in this work. ....	19
Figure 1.11 Composition of a double-emulsion radiographic film showing the 10 - 20 μm thick radiation sensitive emulsion layer deposited on either side of a 150 – 200 μm polyester base. ....	20
Figure 1.12 Schematic diagram of a cylindrical chamber showing the central collecting electrode, guard ring and polarizing electrode. ....	23
Figure 1.13 A first approximation assumes that there is no beam divergence and that the pencil beams are parallel and spatially invariant. ....	26

Figure 1.14 Representation of the point kernel C/S dose calculation algorithm. Vector $r$ shows the dose deposition point and the vector $r'$ shows the site of primary photon interaction. ....	28
Figure 1.15 An example of subregion assignment for a simplified flattening filter component module.....	32
Figure 1.16 Coronal view of patient voxelized geometry (left). The gray values are representation of the computed tomography densities and the color values are representation of the positron emitted tomography glucose uptake. The right image is a transverse view of the patient densities where the tumour is clearly visible in the lung..	36
Figure 1.17 Transverse (upper left), coronal (bottom left), sagittal (upper right) and beams-eye-view (bottom right) representation of the patient densities with two beams conforming on the planning target volume. Other beams are not shown for clarity. ....	37
Figure 1.18 Illustration of the interplay effect between a target volume and a multi-leaf collimator. The leaves are sweeping to the right to uniformly cover the internal target volume (blue). The target volume (red) is moving from left to right in the first delivery (top) and from right to left in another delivery (bottom). The dose received by the target volume depends on the relation between the motion of the target and the motion of the leaves. The target is receiving more dose in the first delivery than in the second delivery. ....	46
Figure 2.1 Illustration of the workflow to perform MC dose calculation for a specific patient. First, the patient data (images, plan, contours, dose, MLC sinogram) is extracted, processed and visualized. Second, cumulative probability distribution functions and voxelized geometries are converted as input file. Third, the information is transferred to the calculation cluster and the simulations are steered remotely. Finally, the calculation results are transferred back to the interface for analysis and visualization purposes. ....	60
Figure 2.2 Example of result for the beam modeling component of the interface. Crossplane (left) and inplane (right) measurements of off-axis absolute dose profile (black) are compared against Monte Carlo results (colors) at different depths for a 4 cm field size. An example of gamma error analysis is available at the bottom. The automated beam modeling process attempts to minimize the error function for various field sizes and at different section of the profiles (e.g., penumbra, tail, flat). ....	61
Figure 2.3 Example of cumulative probability distribution functions extracted for 4 different types of treatment techniques: 3D CRT (up-left), step-shoot IMRT (up-right), VMAT (bottom-left), HT (bottom-right). ....	62
Figure 2.4 Crossplane view of the Elekta Synergy accelerator BEAMnrc model (jaws not shown). ....	65
Figure 2.5 Crossplane illustration of the Elekta SynergyS accelerator BEAMnrc model.	67
Figure 2.6 The MLCE component model was modified to define the leaf width on an arc (right) instead of the isocenter plane (left). ....	69
Figure 2.7 Inplane view of the tomotherapy binary multi-leaf collimator geometry (left). A closer view (not to scale) of the interleaf air gap and of the tongue and groove is also shown (right). ....	69

Figure 2.8 Illustration of the impact of primary source shielding. The beam focal spot is shown in red and represents the electron beam impinging on the target. Focused leaf sides are also shown in red and defocused leaf sides are shown in black. The defocused leaf sides are defined as "defocused" because they are focused on a point located above the beam focal spot. The amount of primary source visible (green arrows) in the isocenter plane through off-centered leaf opening is smaller when the leaf sides are defocused. ... 71

Figure 2.9 Example of photon fluence reduction due to primary source shielding when a single leaf is opened. Leaf number 32 and 33 are the central leaves..... 71

Figure 2.10 Example of fluence reduction results (top) based on an analytical code that calculates the amount of photon fluence produced by a finite source that is reaching points in the isocenter plane. In this case, the leaf sides were focused on the beam focal spot so the fluence reduction is similar for centered and off-centered leaves. A closer view of the center leaves is also shown (bottom). The two inner photon traces in yellow (closer to the isocenter position 0) are shown to hit different part of the asymmetric MLC geometry, which explains partially the asymmetry of the fluence reduction from one side of the leaf bank to the other. The dimensions are in cm. .... 72

Figure 2.11 MC-calculated transverse dose distribution for a single tomotherapy projection (~7 degrees) with 3 non-adjacent leaves fully opened for (a) static gantry angle (0 degrees) and (b) continuous gantry angle variation (-3.53 to 3.53 degrees). A comparison between dose profiles extracted at 17 cm from the isocenter (shown by arrow) in the direction perpendicular to both the leaf movement and the beam direction is shown in (c). The phantom coordinate axis perpendicular to the arrow (up to down in the figure) is parallel to the beam direction. (Source: Paper I)..... 77

Figure 2.12 Example of scatter plot for a phase space file extracted at 60 cm from the target. The phase space file is used to calibrate the leaf position by extracting photon fluence profile along the leaf movement direction. The figure shows a leaf opening of 2 cm located off-center (left). Only a few leaves are actually opened and the remaining leaves are closed (right) with a gap to avoid collisions. The X axis is parallel to the leaf movement direction and the Y axis is perpendicular to the leaf movement direction. Both X and Y axes are perpendicular to the beam direction. .... 78

Figure 2.13 Example of leaf calibration result for the Elekta SynergyS MLC. The difference between the field edge and the projected leaf tip position is shown as a function of off-axis position for the two MLC banks along with a polynomial fit. The parabolic shape of the curve is caused by the off-axis variation of the leaf tip transmission and a gradual change in the location of the photon / leaf intersection along the leaf curvature ..... 79

Figure 2.14 (a) MC- simulated and measured absolute dose profiles (crossplane) at 10 cm depth for four different field sizes (left). Gamma analysis for the same profiles is shown on the right. The same measurements are also compared with the Monaco TPS (b) and the XiO TPS (c). (source: Paper I)..... 80

Figure 2.15 Monte Carlo simulation of transmission dose percentage at 5 cm depth for the Elekta Synergy accelerator (normalized to the 10x10 cm<sup>2</sup> open field dose). The leaves

are completely closed and the off-axis distance is perpendicular to the leaf movement direction and relative to the central axis. .... 82

Figure 2.16 Monte Carlo simulation of transmission dose at 5 cm depth for the Elekta SynergyS accelerator (normalized to the 10.4x10.4 cm<sup>2</sup> open field dose). The blue line is for an MLC rotation of 3 degree and the red line is for an MLC rotation of 5 degrees. As explained in section 2.2.3, the MLC is rotated around a crossplane axis to slightly defocus the leaf side with respect to the beam focal spot. The leaves are completely closed and the off-axis distance is perpendicular to the leaf movement direction and relative to the starting position of the phantom located at 160 mm from the central axis. The leaves are starting and ending at distances of 70 cm and 230 cm respectively. .... 83

Figure 2.17 Tongue and groove dose. The tongue & groove dose is obtained by summing the dose calculated for a given set of open leaves and the dose calculated with the opposite field (leaves that were closed are opened and vice versa). The insert shows the dose calculated for one set of open leaves. .... 84

Figure 2.18 Tongue and groove dose. The tongue & groove dose is obtained by summing the dose calculated for a given set of open leaves and the dose calculated with the opposite field (leaves that were closed are opened and vice versa). The blue line is for an MLC rotation of 5 degree and the red line is for an MLC rotation of 3 degrees. Only one of the added profiles is shown in light blue and pink (one for each MLC rotation). .... 85

Figure 2.19 Inplane off-axis dose profile at 10 cm depth, SSD 100 cm for a field size of 4 cm defined on the isocenter plane. The red line is for the convolution-superposition algorithm and the black line represents the measurements. The measured field size (FWHM) is smaller than the treatment planning field size because of the defocused leaf side. .... 86

Figure 2.20 Inplane off-axis dose profile at 5 cm depth, SSD 100 cm for a field size of 1.6 cm defined on the isocenter plane (4 leaves are opened). MC simulation performed with an MLC rotation of 5 degrees and a translation of 2.2 mm (top) matches well the measurements (Omnipro). The agreement is clearly worse for the MC simulation performed without the MLC rotation (bottom). The bottom of each figure shows an error analysis (gamma 1% / 1mm). .... 87

Figure 2.21 (a) HT MC-simulated and measured absolute dose profiles in crossplane (cr) and inplane (inp) directions at 10 cm depth for three different jaw field sizes (left). Gamma analysis for the same profiles is shown on the right. Also shown are comparisons between the Hi-Art HT TPS and. .... 89

Figure 2.22 (a) MC-simulated and measured dose profiles (crossplane) for the helical tomotherapy accelerator for a 1 cm jaw field size and an alternating pattern of 2 closed leaves and 2 opened leaves. Film data at both ends of the measurement are distorted due to film edge effect. (b) Helical tomotherapy accelerator transverse profiles comparison for the largest field size following modifications to the MLCE BEAMnrc component module. (source: Paper I) .... 90

Figure 2.23 Transmission dose at 5 cm depth for the tomotherapy accelerator (normalized to an open field dose for a 5x40 cm<sup>2</sup> field size). Film measurements (normalized with ion chamber) are shown in black and Monte Carlo simulations are shown in yellow. The blue

line and the red line are included to illustrate the impact on the Monte Carlo transmitted dose of sub-mm changes in the MLC geometry parameters..... 91

Figure 2.24 The tongue & groove dose is obtained by summing the dose measured or calculated for two opposing fields having respectively odd and even leaves opened. Film measurements (normalized with ionization chamber reading in the small open section of the field) are shown in black and Monte Carlo simulations are shown in yellow. The blue line and the red line are included to illustrate the impact on the Monte Carlo simulation of sub-mm changes in the MLC geometry parameters. .... 92

Figure 2.25 MC simulation of a modulated field. The couch and the gantry are static and the field contains openings of different sizes (1 leaf, 2 leaves, 3 leaves) at various off-centered positions. Film measurements (normalized with ionization chamber reading in the largest open section of the field) are shown in black, SFD diode measurements are shown in red and Monte Carlo simulations are shown in yellow. The blue line is included to illustrate the impact on the Monte Carlo simulation of sub-mm changes in the MLC geometry parameters. .... 94

Figure 2.26 MC-calculated transverse dose distribution (left) and comparison with the TPS (right) for (a) 3D-conformal, (b) step-shoot IMRT. (source: Paper I)..... 95

Figure 2.27 MC-calculated transverse dose distribution (left) and comparison with the TPS (right) for (a) VMAT prostate case (b) helical tomotherapy brain case. MC-calculated dose for points located in air were zeroed for the helical tomotherapy brain case. (source: Paper I)..... 96

Figure 2.28 MC-calculated transverse dose distribution (left) and comparison with the TPS (right) for a VMAT lung stereotactic treatment. The comparison also includes MC calculations performed with rigid patient motion (sinusoidal function with amplitude of 5 mm and a period of 6 seconds for all three standard motion directions). (source: Paper I) ..... 97

Figure 2.29 MC-calculated transverse dose distribution (insert) for a 3D-CRT double tumour lung stereotactic treatment. Dose volume histogram shows the results of the MC simulation (dotted line) and the treatment planning system dose calculation (solid line).98

Figure 2.30 MC-calculated transverse dose distribution (left) and comparison with the TPS (right) for (a) HT TMI case (b) HT "extreme" case. The comparison also includes MC calculations performed with discrete angles to simulate the TPS algorithm and film measurements for (b). The "extreme" case is used to illustrate the effect of gantry angle discretization: a fast treatment (modulation factor of 1.1) of a 3 cm diameter cylindrical target in a solid water phantom located at about 15 cm from the isocenter. (source: Paper I)..... 99

Figure 2.31 Tomotherapy treatment planning system dose overestimation (calculated / measured) caused by gantry discretization for small target volume treatments performed with low modulation factor (source: TomoTherapy Inc., field safety notice 5089). ..... 101

Figure 3.1 Deformable image registration parameters (top) and example of deformable vector field superimposed on a coronal view of the lung and the diaphragm. Both figures were generated using modified versions of the DIRART open source package. .... 109

Figure 3.2 Histogram of GTV voxel displacement in the sup-inf direction with respect to a reference phase (e.g., exhale) based on deformable image registration. The result based on rigid registration is also shown as a circle for validation purposes. (Source: Paper II) ..... 110

Figure 3.3 Position of the tumour with respect to a reference phase for ten 4D-CT breathing phases and seven breathing phases with equally spaced tumour position. (source: Paper II)..... 111

Figure 3.4 (a) Coronal view of patient voxelized densities. (b) The density profile for breathing phase 5.5 was interpolated between the density profile of breathing phase 5 and 6. (c) The density profile for breathing phase 4 was interpolated between the density profile of breathing phase 1 and 7. The density profile for breathing phase 4 was also mapped with deformable vector fields using the density profile of breathing phase 7 and compared with the exact density profile of breathing phase 4. (source: Paper II)..... 114

Figure 3.5 (a) Deformed reference volume using forward deformable vector fields (DVF). The ratio between the reference grid volume and the transport grid volume is defined as the volume scaling factor (VSF). (b) Collecting volume for the reference voxel using spatially interpolated backward DVF. (c) Another view of the backward DVF as stored in the input file for Monte Carlo simulation (at the corner of each voxel). For the volume average dose mapping method, the location of the particle is randomly sampled along the deposition path and mapped back to the reference grid using a spatially interpolated backward DVF. (d) For the voxel center dose mapping method, the backward DVF is used to find the reference grid voxel. Forward DVF and non-deformed collecting volume (cubes) are used to check that energy deposition should be done in both red and green voxels. (source: Paper II) ..... 115

Figure 3.6 The volume scaling factor (VSF) profile for breathing phase 5.5 was interpolated between the VSF profile of breathing phase 5 and 6. The ratio between the VSF and the exact value is shown for the profile and a histogram shows the range of values for the full patient slice. Similar information is shown for the determinant of the Jacobian of the DVF. See figure 3.4 (a) to visualize the profile location in the patient anatomy. The peak at 6 cm is at the location of the dense tumor and that at 10 cm at the lung/diaphragm interface. (source: Paper II) ..... 120

Figure 3.7 Sagittal representation of the dose distribution and densities for a nasopharynx clinical case treated with helical tomotherapy (left). The right side shows the dose and a large variation in density along a profile. Also shown is the dose calculated with density interpolation / voxel center methods and a deformable vector field of half the voxel size to validate the appropriate use of the density ratio factor in equation 3.1. This dose profile was shifted back by half a voxel to facilitate the comparison. (source: Paper II) ..... 122

Figure 3.8 Gantry angle vs. time for a test treatment. The recorded (iCom) gantry angle (red) and the required treatment planning system gantry angle (blue) are plotted. The difference between the two is also plotted in green. The machine allows a specified amount of error to properly adapt to rapid change in gantry speed (step function)..... 124

Figure 3.9 (a) Measurement setup that includes a programmable moving phantom and a cedar insert with an ionization chamber. The linear accelerator is delivering a sweeping

field in the same direction as the phantom motion. A switch is recording the patient motion, a large volume ionization chamber is recording the transmitted dose and an iCom listening software is used to record the position of the leaves. (b) Example of measurement results after processing (phantom period is 8 seconds). The dose to water in (b) is the dose recorded by the ionization chamber per electrometer sample and it may also be interpreted as a dose rate. (source: Paper II)..... 125

Figure 3.10 (a) Sagittal representation of the cumulative dose distribution and densities for the Monte Carlo phantom simulation (left). Dose profile in moving and non moving parts of the phantom (right). Phantom motion period was 8 seconds and density mapping / voxel average methods were used for this example of Monte Carlo simulation. (b) Dose measurement in the chamber as a function of time compared with pencil beam and Monte Carlo simulations (beams-eye-view fast algorithm is similar but not shown for clarity). Uncertainties were discussed in section 2.3.2 but not shown for clarity. (source: Paper II) ..... 129

Figure 3.11 Comparison between volume weighting and mass weighting when mapping energy deposition from the transport grid to the reference grid. In this method, the use of volume weighting assigns equal weight to the secondary particles depositing energies in two voxels of different densities. (source: Paper II) ..... 131

Figure 4.1 (a) Example of patient treated with a lung stereotactic treatment (patient #5) with a typical tumour motion displayed in both coronal and sagittal planes. (b) GTV dose volume histogram for helical tomotherapy plan simulations using various breathing patterns (blue) with (right) and without (left) a 5 mm setup error. Monte Carlo simulations were done using density interpolation / voxel center methods. Simulations were also performed with no breathing motion on the free breathing and the exhale patient geometries (red) for comparison purposes. The free breathing simulations were performed with both continuous (green) and discrete (yellow – Tomotherapy only-) gantry motion. The free breathing simulations in the right figure do not include the 5 mm setup error to facilitate the appreciation of the changes caused by the setup error. (Source: Paper II) ..... 138

Figure 4.2 Example of patient treated with a lung stereotactic treatment (patient #5) using VMAT. Monte Carlo simulations were also performed with no breathing motion on the free breathing (green) and the exhale patient geometries (red) for comparison purposes. .... 139

Figure 4.3 (a) View of the lung anatomy and target contours (left) for patient #6 treated with a stereotactic lung treatment. Tumour motion is displayed (right) in both coronal and sagittal planes. .... 139

Figure 4.4 (a) View of the lung anatomy and target contours (left) for patient #2 treated with a SABR lung treatment. Tumour motion is displayed (right) in both coronal and sagittal planes. (b) GTV dose volume histogram for VMAT (left) and helical tomotherapy (right) 4D MC simulations using various breathing patterns. Simulations were also performed with no breathing motion on the free breathing and the exhale patient geometries (red) for comparison purposes. The free breathing simulations were performed with both continuous (green) and discrete (yellow) gantry motion. .... 141

Figure 4.5 (a) View of the lung anatomy and target contours (left) for patient #1 treated with a SABR lung treatment. Tumour motion is displayed (right), in both coronal and sagittal planes. (b) GTV dose volume histogram for VMAT (left) and helical tomotherapy (right) 4D MC simulations using various breathing patterns. Simulations were also performed with no breathing motion on the free breathing and the exhale patient geometries (red) for comparison purposes. The free breathing simulations were performed with both continuous (green) and discrete (yellow) gantry motion. .... 142

Figure 4.6 (a) View of the lung anatomy and target contours (left) for patient #3 treated with a SABR lung treatment. Tumour motion is displayed (right), in both coronal and sagittal planes. (b) GTV dose volume histogram for VMAT (left) and helical tomotherapy (right) 4D MC simulations using various breathing patterns. Simulations were also performed with no breathing motion on the free breathing and the exhale patient geometries (red) for comparison purposes. The free breathing simulations were performed with both continuous (green) and discrete (yellow) gantry motion. .... 143

Figure 4.7 (a) View of the lung anatomy and target contours (left) for patient #7 treated with a SABR lung treatment. Tumour motion is displayed (right), in both coronal and sagittal planes. (b) GTV dose volume histogram for VMAT (left) and helical tomotherapy (right) 4D MC simulations using various breathing patterns. Simulations were also performed with no breathing motion on the free breathing and the exhale patient geometries (red) for comparison purposes. The free breathing simulations were performed with both continuous (green) and discrete (yellow) gantry motion. .... 144

Figure 4.8 (a) View of the lung anatomy and target contours (left) for patient #8 treated with a SABR lung treatment. Tumour motion is displayed (right), in both coronal and sagittal planes. (b) GTV dose volume histogram for VMAT (left) and helical tomotherapy (right) 4D MC simulations using various breathing patterns. Simulations were also performed with no breathing motion on the free breathing and the exhale patient geometries (red) for comparison purposes. The free breathing simulations were performed with both continuous (green) and discrete (yellow) gantry motion. .... 145

Figure 4.9 (a) View of the lung anatomy and target contours (left) for patient #8 treated with a SABR lung treatment. A second tumour was artificially created in the left lung to maximize the treatment impact on the first tumour. A combined double tumour HT treatment plan was optimized. The resulting change in the MLC sinogram – from top to bottom - and the dose volume histogram are shown..... 146

## Abbreviations

3D	three dimensional
4D	four dimensional
3D-CRT	three dimensional conformal radiotherapy
4D-CT	four dimensional computer tomography
CBCT	cone beam computer tomography
CM	component module
MU	monitor unit
CPDF	cumulative probability distribution function
CPE	charge particle equilibrium
C/S	convolution superposition
CT	computer tomography
CTV	clinical target volume
DIR	deformable image registration
DVF	deformable vector field
DVH	dose volume histogram
ECUT	electron cut-off energy (including rest mass)
GTV	gross target volume
Gy	Gray
HT	helical tomotherapy
IMRT	intensity-modulated radiotherapy treatment
ITV	internal target volume
linac	linear accelerator
MC	monte carlo
MLC	multi-leaf collimator
MRI	magnetic resonance imaging
MVCT	megavoltage computed tomography
OAR	off-axis ratio
PCUT	photon cut-off energy
PDD	percent depth dose
PET	positron emission tomography
PPS	position-probability-sampling
PTV	planning target volume
RDF	relative dose factor
SABR	stereotactic ablative radiotherapy
SCS	static-component simulation
SSD	source surface distance
TCPE	transient charge particle equilibrium
TMI	total marrow irradiation
TOHCC	the Ottawa Hospital Cancer Center
TPR	tissue phantom ratio
TPS	treatment planning system
VMAT	volumetric modulated arc therapy

# **1 Background**

## ***1.1 Introduction***

Chapter 1 provides background information on several topics related to this thesis. Section 1.2 briefly describes radiation therapy. Section 1.3 provides specific information about various accelerators used for treatment delivery. Section 1.4 describes dose representation, dose measurements and dose calculation for these treatments. Section 1.5 provides specific information about lung cancer and the radiotherapy process for lung stereotactic ablative radiotherapy treatments. Section 1.6 describes image registration and issues related to patient motion. Section 1.7 outlines the thesis structure.

## ***1.2 Radiation therapy***

Radiation has been used for curative and palliative treatments for more than one hundred years. The aim of radiation therapy is to deliver a prescribed dose of ionizing radiation to a target volume to kill the cells by damaging their DNA molecules. The absorbed dose is defined as the energy deposited in a small mass of medium by charged particles divided by the mass of that medium. The main limiting factor in the effectiveness of the radiation treatment is the risk of complications caused by the irradiation of normal tissues surrounding the tumour. To limit those risks to an acceptable level, it is important to choose carefully the appropriate source of radiation and treatment technique. There are many techniques and they are generally categorized in two main branches according to the location of the radiation source: brachytherapy and external beam radiotherapy.

Brachytherapy consists of placing a radioactive source within or close to the tumour while external beam radiotherapy techniques are carried out using a source of radiation located at some distance from the patient (typically 100 cm from the target). The ionizing radiation used for external beam techniques may be generated by high-energy accelerators such as a linear accelerator (linac) or produced by the decay of radioisotopes such as  $^{60}\text{Co}$ . The prescribed dose is generally delivered in several fractions (3-40) spread over multiple days. This thesis is focused on linac-based stereotactic ablative radiotherapy (SABR) for lung cancer, an external photon beam technique used to deliver relatively high doses of ionizing radiation to localized small lung lesions (< 5 cm) in few fractions (3-5).

## ***1.3 Treatment delivery***

### **1.3.1 Conventional treatment unit**

A linac uses microwave technology to accelerate electrons in a waveguide and subsequent collision with a metal target produces high energy x-rays. In a conventional treatment unit, the accelerator is confined in a C-arm gantry (see figure 1.1) and the high energy x-rays are shaped using a multi-leaf collimator (MLC) and pairs of jaws. The MLC is made of pairs (26 to 160) of small opposing leaves (width 3 mm to 1 cm). A moveable treatment couch (translation, rotation) is used to help position the patient at the appropriate location before starting the treatment. The gantry may be rotated around the patient during the treatment delivery and the collimator (jaws, MLC) may also be rotated to improve the field conformality. Different beam orientations are obtained by



**Figure 1.1** Image of a conventional treatment unit –Elekta Synergy- (left) with a multi-leaf collimator (right).

combination of collimator, gantry and treatment couch rotations and the common fixed point of intersection of the rotation axis is referred to as the linac isocenter.

Regardless of the technique, a treatment delivery is generally divided in several treatment segments (~5-200) delivered sequentially. The segments are defined using two control points specifying the amount of radiation to be delivered and the state of the machine at the beginning and at the end of the segment. Machine components are moved approximately linearly between two control points when needed. The simplest treatment technique is 3D conformal radiation therapy (3D-CRT). This technique makes use of a few static beams that may have different gantry, couch and collimator angles. The leaf positions are fixed during each segment delivery and the beam is turned off to allow machine components to move from one segment to another. The two control points for each segment are therefore identical since the machine is not moving during the delivery. This approach is not efficient when a very large number of beams/segments are used. More recent treatment techniques, such as volumetric modulated arc therapy (VMAT) (Otto, 2008), allow variation of dose rate and machine component positions to be moved

during segment delivery. The benefits of using continuous motion of machine components include increased efficiency, simplified planning and superior treatment plan quality in some cases (Popescu *et al.*, 2010).

Most conventional treatment units are equipped with imaging systems to verify patient position before and/or during treatment delivery. A 2D amorphous silicon flat-panel detector is installed on the gantry in-line with the treatment beam and rotates with it to record portal images. Those images consists of low contrast images of the patient superimposed on the shape of the delivered beam to verify to correct alignment of the patient anatomy (bones, skin) with respect to the field edges. Another system called cone-beam computed tomography (CBCT) is also installed on the gantry to obtained 3D or 4D scan of the patient using a kilovoltage x-ray tube (cone beam) and a 2D amorphous silicon based flat-panel detector. CBCT allows superior soft-tissue contrast and volumetric information about the relative position of each organ (Bissonnette *et al.*, 2012). It is routinely used for SABR lung treatments before the start of the treatment delivery and occasionally at one or more intermediate phase of the treatment delivery.

### **1.3.2 Helical tomotherapy treatment unit**

Helical tomotherapy (HT) (Mackie *et al.*, 1993) is a radiation therapy technique using a continuously rotating gantry and a translating couch to irradiate a target volume in a helical manner. The 6 MV linac is confined in a closed circular gantry to allow rotation speeds as high as 30 degrees per second. As the treatment couch moves into the gantry bore, the target volume is irradiated in slices using a slit beam collimated by jaws in the direction of couch motion (opening of 1 cm, 2.5 cm or 5 cm) and by a binary multi-leaf

collimator in the direction perpendicular to the couch motion. The MLC consists of 64 interlaced leaves of 6.25 mm for a total opening of 40 cm defined at the axis of gantry rotation (85 cm from the source). The leaves may be either fully open or fully closed with a transit time of less than 20 ms (Balog *et al.*, 2003). Each gantry rotation during the treatment is divided into 51 equally-spaced projections (~7 degrees) for intensity modulation purposes. Modulation is achieved by assigning a value of open time to each leaf at each of the projection. The open times are centered about the mid-point of each projection and correction factors are used to account for leaf latency and partial photon source shielding. Figure 1.2 shows an example MLC sinogram representing the leaf open times in colors as a function of projection. Figure 1.3 shows an illustration of an MLC sinogram with 4 leaves and 1 projection.

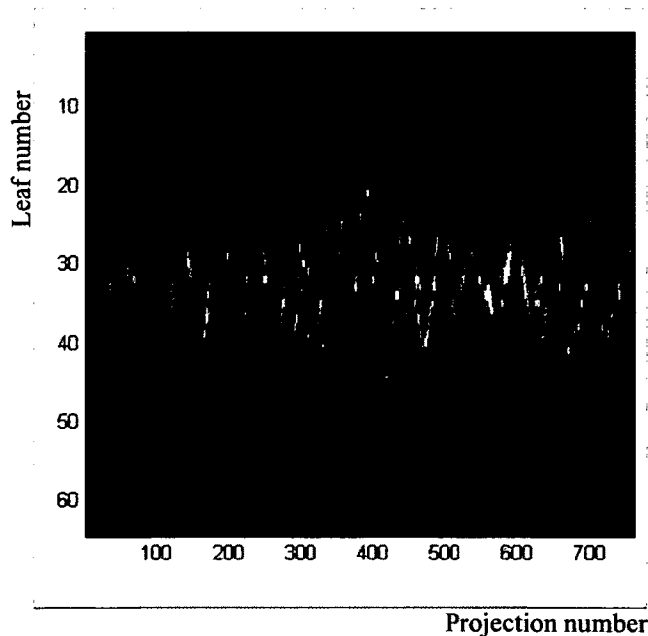


**Figure 1.2 Example of tomotherapy multi-leaf collimator sinogram. The rows show the leaf numbers and the columns show the projection numbers. The color intensity shows the leaf open time.**

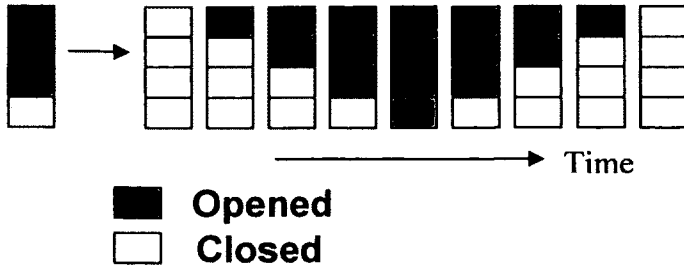


**Figure 1.3** Illustration of an MLC sinogram with 4 leaves and 1 projection. The gray value represents the open time. The top leaf has a higher open time than the bottom leaf. The open times are centered about the mid-point of each projection so the top leaf will be the first one to be opened and the last one to be closed.

The HT treatment unit is equipped with megavoltage computed tomography imaging capacity (MVCT). The MVCT is similar to a CT scanner except that a detuned treatment beam (electron energy lowered to 3.5 MeV) is used for producing the images instead of a regular x-ray tube. The projections are recorded with an on-board detector panel (i.e., xenon chambers) that rotates with the beam. The use of a treatment beam for imaging simplifies the machine construction and makes the reconstruction of patient anatomy less sensitive to metal artifacts. On the other hand, it also implies a lower soft-tissue contrast so the images are mostly used for setup or dose verification before treatment delivery (Vaandering *et al.*, 2009; Langen *et al.*, 2005; Ruchala *et al.*, 2000). The images are rarely used for diagnostic or contouring purposes except for adaptive purposes or palliative treatments.

The HT treatment unit was used in many studies for lung SABR treatments (Russo and Rosen, 2011; Hodge *et al.*, 2006; Dunlap *et al.*, 2010; Chi *et al.*, 2012; Monaco *et al.*, 2012; Yang *et al.*, 2011b; Chi *et al.*, 2011; Hsieh *et al.*, 2010; Tomita *et al.*, 2010). At the Ottawa Hospital Cancer Center (TOHCC), the HT lung SABR treatment times are usually longer than for a conventional treatment unit (10-15 minutes

vs. 5-7 minutes, beam on only) so this modality is usually restricted to cases where intensity modulation provides benefit (larger tumours, critical normal structures very close to target, multiple tumours). The current machine configuration does not allow the use of non coplanar beam delivery or dynamic jaws and the plan quality may occasionally suffer from a larger penumbra in the superior-inferior direction. A recent publication (Sterzing *et al.*, 2010) and private discussion with the company suggest that those limitations will be removed in the near future, which will allow improved treatment plan quality and reduction of treatment times by 50%. The company is also currently testing the possibility of using the dynamic jaws and the leaves to track tumours but the project remains essentially research oriented at this point.



**Figure 1.4** Image of an helical tomotherapy treatment unit (left) with a binary multi-leaf collimator (right).

### **1.3.3 Robotic treatment unit**

The CyberKnife system (Accuray Inc., Sunnyvale, CA) is a robotic treatment unit that was first used to treat a patient in 1994 (Adler *et al.*, 1997; Shimamoto *et al.*, 2002; Chang *et al.*, 2003; Kuo *et al.*, 2003). The system mounts a lightweight 6MV linear

accelerator on an industrial robotic arm with six degrees of freedom. The machine is capable of delivering radiotherapy while being guided in real time by two ceiling-mounted diagnostic x-ray cameras with corresponding orthogonal floor-mounted amorphous silicon detectors. The radiation beam is collimated by cones (or an iris collimator) having a circular opening ranging in size from 5 to 60 mm. The system is optimal to deliver radiation from a large number of different positions in space and it is currently configured to use 101 specific nodes, each with 12 approach angles, thus offering 1212 possible beam directions in both isocentric and nonisocentric configurations. The lightweight and the large number of degrees of freedom make it possible to compensate for patient setup motion but also to track the target (or any related surrogate) both in translation and rotation efficiently in real time. The CyberKnife system was used in many studies for lung SABR treatments (Nuyttens *et al.*, 2006; Brown *et al.*, 2007a; Brown *et al.*, 2007b; Brown *et al.*, 2007c; Gibbs and Loo, 2010; Vahdat *et al.*, 2010). Tracking the tumour allows the reduction or elimination of motion margins which in turn provides safer treatments since the radiation beams are smaller and normal tissues are receiving less dose. In practice, it is difficult to place tumour fiducials (small metal components easily seen on x-ray images) inside the lung because of the risk involved. Therefore, the tumour must be clearly visible on the x-ray images to properly track it. The difficulty of angle imaging must be assessed for each patient prior to the treatment. The lung SABR treatments are also relatively long compared with other modalities (approximately 80 minutes vs. 20 minutes, including patient setup, beam-off time, etc...). At TOHCC, the treatments are usually restricted to patients exhibiting large tumour

motion (~2 cm) and/or patients where the treatment planning is challenging using other treatment modalities (e.g., normal tissue dose higher than prescribed limits).

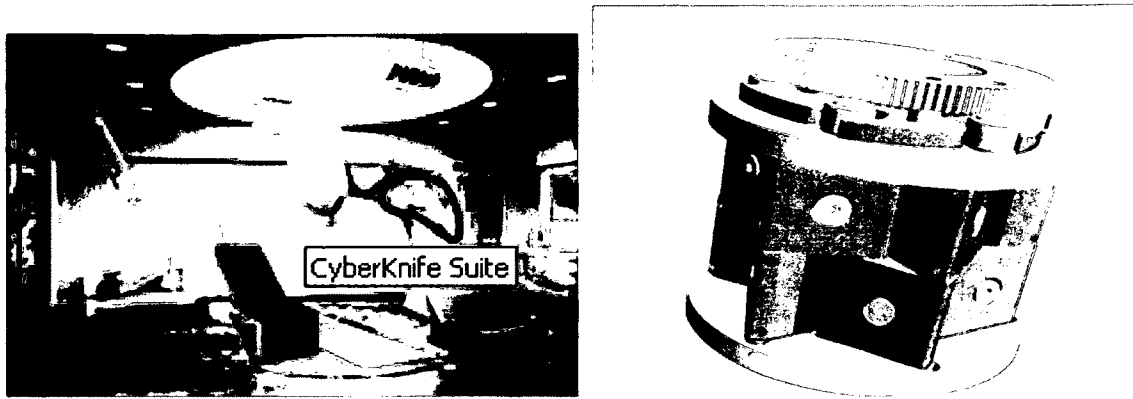


Figure 1.5 Image of a robotic treatment unit (left) with an iris collimator (right).

## **1.4 Dose distributions**

### **1.4.1 Representation of dose distributions**

The absolute value of the absorbed dose at an arbitrary point in a phantom (depth  $d$  and distance  $r$  from the beam central axis) depends on the linac prescribed output  $O$ , the linac output conversion factor  $O_c$  (cGy/MU), the field size  $A$  and the source surface distance (SSD). The linac output  $O$  is specified in monitor units (MU), a user defined quantity related to the amount of electric charges collected by the ionization chambers located in the accelerator head. The linac is calibrated such that its output conversion factor  $O_c$  equals 1.00 cGy per MU in water under calibration conditions defined by the facility protocol (i.e., SSD = 95 cm,  $A = 10 \times 10 \text{ cm}^2$ ,  $r = 0 \text{ cm}$  and  $d = 5 \text{ cm}$ ). This definition may vary from one treatment facility to another. A complete knowledge of the dose distribution within the irradiated phantom requires a three dimensional description. This may be achieved through dosimetry functions which are used to relate the absorbed

dose delivered at an arbitrary point in a given field to the dose determined under calibrating conditions. The dose at any point in a flat phantom may be expressed as follows:

$$D(d,r) = O * O_c * RDF(A) * PDD(A,d) * OAR(r,d) \quad (1.1)$$

The relative dose factor RDF, also referred to as the output factor, relates the dose determined under calibration conditions (for a field size of interest  $A$ ) to the dose determined under calibration conditions for a reference field size (i.e.,  $A=10 \times 10 \text{ cm}^2$ ). The percentage depth dose (PDD) characterizes the variation of dose with depth along the beam central axis. It relates the dose in a given field at the calibration depth to the dose at another depth of interest. The off-axis ratio (OAR) describes how the dose changes in lateral direction with respect to the dose delivered on the central axis at the same depth. In this work, inplane and crossplane off-axis ratio profiles refer to directions that are respectively perpendicular and parallel to the leaf edge (figure 1.6).

For isocentric setup, tissue phantom ratios (TPR) are often used for practical reasons to characterize the depth dose variation in the patient. They are defined as the ratio of doses at the linac isocenter between a depth of interest and the calibration depth. Since the TPR functions are approximately SSD independent, a smaller number of functions is needed to represent all the possible clinical cases. TPR basically accounts for photon attenuation and is often approximated from the PDD by correcting for small phantom scatter changes and differences in beam divergence through an inverse square

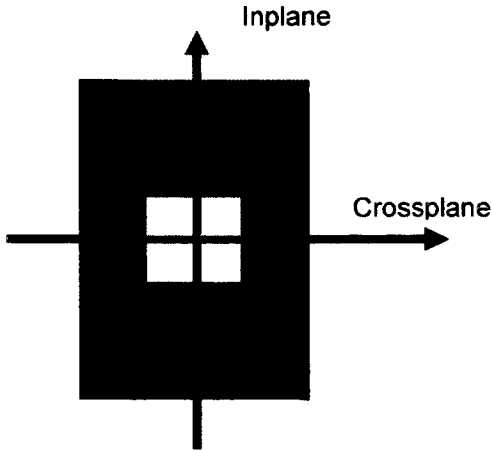


**Figure 1.6 Inplane and crossplane off-axis ratio profiles are respectively defined as perpendicular and parallel to the leaf side.**

factor. Neglecting phantom scatter changes, the dose distribution in a flat phantom may be approximated as follows:

$$D(d, r) = O * O_c * RDF(A) * TPR(A, d) * \left( \frac{100 \text{ cm}}{SSD + d} \right)^2 * OAR(r, d) \quad (1.2)$$

Traditionally, the patient dose distributions were determined by correcting dosimetry functions specified in homogeneous water phantoms for beam modifiers, patient contours and occasionally heterogeneities. Modern approaches generally calculate the dose distributions from first principles. In this case, measurement of dosimetry functions is also needed to set some parameters for the model and provide verification. This approach includes Monte Carlo simulation and convolution/superposition methods discussed in section 1.4.3. For both approaches, accurate and precise measurements of dose distributions and dosimetry functions are required and may be achieved with appropriate dosimeters, discussed in the next section 1.4.2.

## 1.4.2 Measurements of dose distributions

### 1.4.2.1 Considerations for the choice of a dosimeter

A dosimeter is a device capable of providing a reading that is a measure of the absorbed dose deposited in its detection volume. The sensitivity should be independent of dose rate, angle of incidence and energy to give a linear dose response throughout the measured dose distributions. The absorbed dose measured in the detection volume material  $D_{\text{det}}$  may be used to determine the absorbed dose that would be received in the water phantom at the dosimeter position without the presence of the dosimeter. The dose in water  $D_{\text{wat}}$  may be related to the dose  $D_{\text{det}}$  using the following equation (Johns and Cunningham, 1983):

$$D_{\text{wat}} = D_{\text{det}} \left( \frac{\overline{L_{\Delta}}}{\rho} \right)_{\text{det}}^{\text{wat}} \Phi_{\text{det}}^{\text{wat}} \quad (1.3)$$

The mean restricted mass stopping power  $\overline{L_{\Delta}}/\rho$  is a measure of the energy transferred per unit mass to a material as a fluence of ionizing particle  $\Phi$  travels through it. A relative dose or a dosimetry function (e.g., PDD, TPR, RDF, OAR) is determined by taking the ratio of two doses measured in different situations (e.g. two different depths). In this case, the absolute value of the correction factors stated in equation 1.3 is not of interest but rather the change in the correction factors from one condition to the other:

$$D_{wat} = \frac{D_{wat1}}{D_{wat2}} = \frac{D_{det1}}{D_{det2}} \frac{\left(\overline{L_{\Delta}/\rho}\right)_{det1}^{wat1} \Phi_{det1}^{wat1}}{\left(\overline{L_{\Delta}/\rho}\right)_{det2}^{wat2} \Phi_{det2}^{wat2}} \quad (1.4)$$

The factors  $\left(\overline{L_{\Delta}/\rho}\right)_{det1}^{wat1}$  and  $\Phi_{det1}^{wat1}$  are correcting for differences between the water and the detector material. They may be minimized by using as much as possible a water equivalent detector material. The first correction factor accounts for differences in the mean restricted mass stopping power. For example, a silicon detector has a smaller mean restricted mass stopping power than water so less dose is actually absorbed in the silicon dosimeter than there would be in the water at the same position without the presence of the detector. For relative dose measurements, the change in the electron energy distribution in water from one situation to the other has an impact on this correction factor because the mean restricted mass stopping power is defined as the weighted average of the restricted mass stopping power over the electron energy distribution.

The second correction factor is the electron fluence perturbation factor. It accounts for the changes in electron fluence produced by the presence of the dosimeter. For example, an air dosimeter has a much smaller density than water so the electron fluence is attenuated (or is built up in a non equilibrium situation) less in air than it would be in water. As a consequence, there is more (or less) dose actually absorbed in the middle of the air detector than there would be in water at the same position without the presence of the detector. For relative dose measurements, this perturbation depends on the dose gradient that might differ from one situation to the other.

The presence of the detector may also perturb the electron energy distribution and have an additional impact on the first correction factor. For example, a silicon dosimeter interacts more with low energy photons than water because the photoelectric effect is

more significant at low energy for high atomic number material ( $Z_{\text{silicon}} = 14$  and  $Z_{\text{water}} = 7.5$ ). As a consequence, the electron fluence *and* the proportion of low energy electrons are actually higher in the silicon detector than they would be in water.

The use of correction factors may be relaxed under certain conditions. For example, when the detector size is considerably smaller than the electron range, cavity theory (Spencer and Attix, 1955) predicts that the electron fluence is not perturbed significantly and that the second correction factor is thus equal to 1. The use of correction factors may also be relaxed under condition of charge particle equilibrium (CPE) or transient charge particle equilibrium (TCPE), characterized by constant electron energy spectrum. In such cases, relative dose measurements may be performed without even having to establish the correction factors since they are assumed identical at both positions and cancel each other out. For example, this situation may be applied to the measurement of RDFs, PDDs and OARs in large field sizes (excluding the buildup region and the penumbra) provided that the variation in photon energy distribution across the phantom - ultimately leading to variations in electron energy distribution - are not significant.

The penumbra region is one region of the field in conventional radiotherapy where CPE or TCPE is clearly not established. This is not very important since rigorous dose measurements in the penumbra region are often not considered essential. However, the penumbra region is critical in SABR lung treatments. It even constitutes the field in itself for an effective field size similar or smaller than the electron range in water ( $\approx 1.5$  cm for 6 MV) (Podgorsak and Podgorsak, 1999). Figures 1.7 and 1.8 illustrate the penumbra differences between small fields and large fields. For a large field size, the

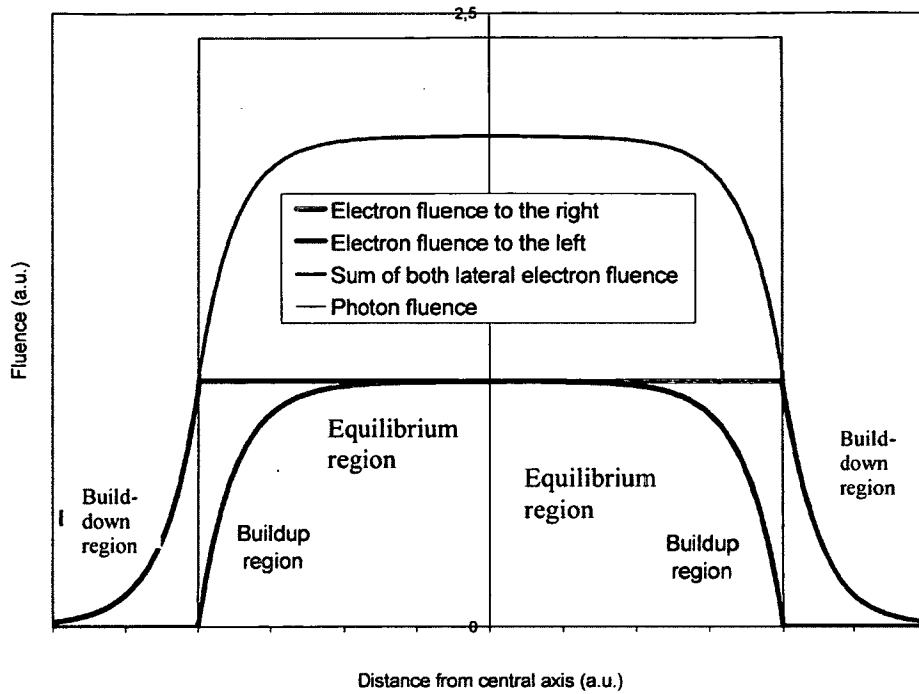


**Figure 1.7** Schematic representation of electron and photon fluences at 5 cm depth in a large field size for an incident megavoltage photon beam. Lateral equilibrium is established in the central portion of the field. The fluences are shown separately for electrons having motion components towards the left and the right side of the profile.

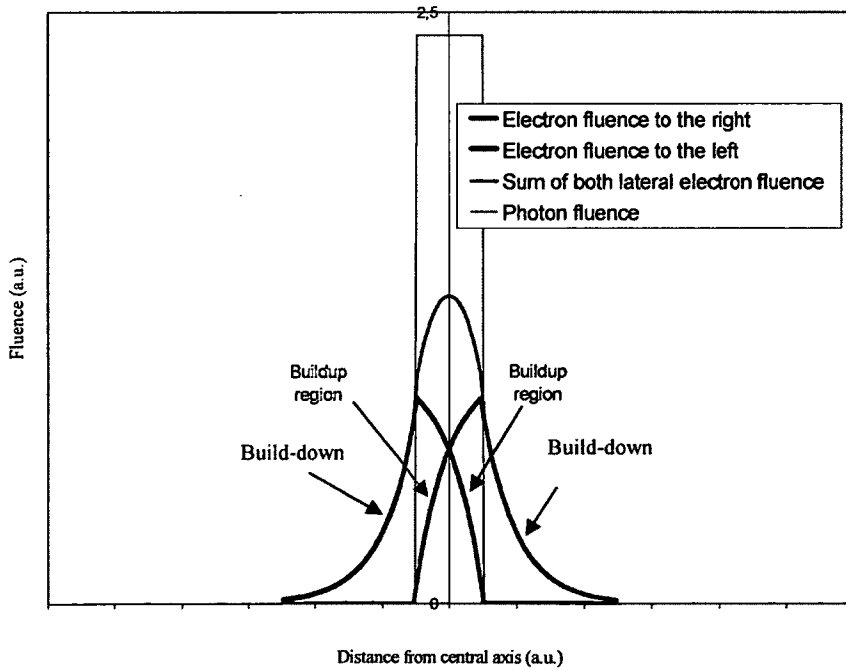


**Figure 1.8** Schematic representation of the photon and electron fluences at 5 cm depth in a small field size for an incident megavoltage photon beam. Lateral equilibrium is not established in the central portion of the field. The fluences are shown separately for electrons having motion components towards the left and the right side of the profile.

central portion of the field may be visualized as the overlap of both lateral equilibrium regions while for small fields, the central portion of the field consists of the overlap of both lateral buildup regions. The lack of lateral equilibrium and the resulting variation in electron energy distribution in the penumbra implies that the correction factors cannot be neglected when measuring relative dose distributions in those conditions.

Sophisticated methods are available for correcting the non-water equivalence of dosimeters (Paskalev, 2002) Unfortunately, these methods are time consuming and not appropriate for a large number of measurements. Neglecting the correction implies choosing a detector that is as water equivalent as possible to minimize the error involved. It also means that care must be taken when interpreting results based on uncorrected measured dose distributions.

An additional consideration for dosimeters is volume averaging (figure 1.9). A dosimeter provides a measure of the average dose deposited in the detection volume. If non-water equivalence corrections are previously applied, a dosimeter provides a measure of the average dose deposited in the water volume covered by the detection volume. Volume averaging does not affect the results as long as the dose is constant or linearly varying within the detection volume. On the other hand, if the dose variation is non-linear, such as in the penumbra, different types of correction factors (Hartmann, 1995; Rice *et al.*, 1987) may be applied to correct for volume averaging or provide an effective point of measurement. These methods are also time consuming and not appropriate for a large number of measurements. Neglecting the correction factor implies the appropriate choice of detector (as small as possible). As a general rule, the diameter of the detector should be

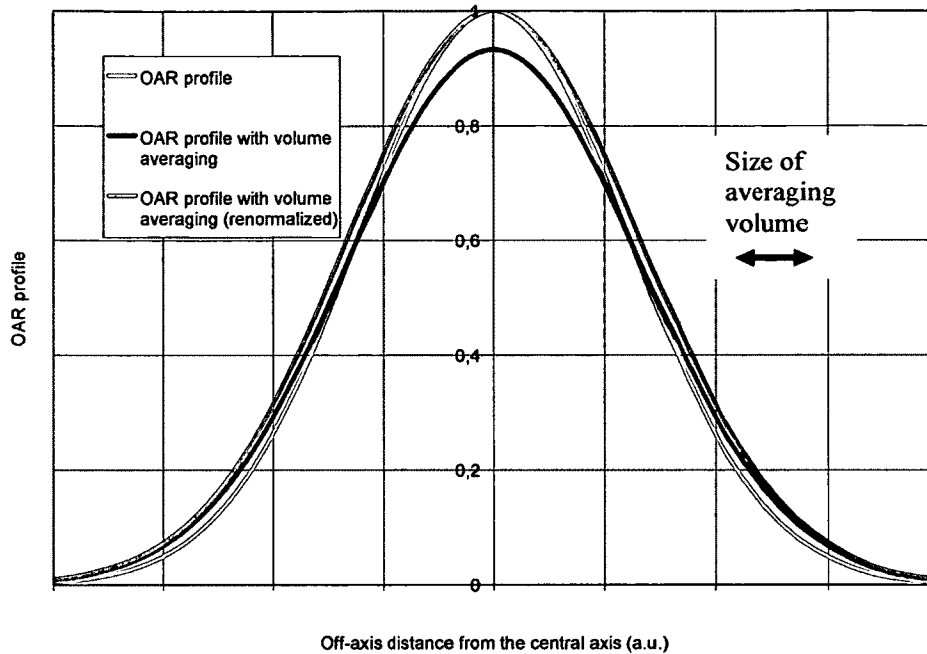


**Figure 1.9** Schematic representation of off-axis ratio (OAR) profile volume averaging. The OAR profile shown is for illustration purposes and is approximated as a Gaussian function. The profile with volume averaging is calculated by convolving the OAR profile with a square function.

at most 1/3 of the field diameter (Hartmann, 1995). The following sections provide information on several detectors used in this work.

### 1.4.2.2 p-type silicon diode

A p-type silicon diode dosimeter is manufactured by depositing a thin film of heavily doped n-type silicon (with a majority of electrons) on top of a lightly doped p-type silicon substrate (with majority of holes), thus creating a p-n junction (Rikner and Grusell, 1986). Majority carriers in the conduction energy band from both sides may diffuse to the other side and recombine, thus creating a depletion layer having a low

concentration of charge carriers and an intrinsic electric field. This electric field opposes further diffusion and is at the basis of the detection process. Ionizing radiation produces electron-hole pairs in the silicon diode by transferring enough energy ( $\sim 3.5$  eV) to valence band electrons to reach the conduction band. Charge carriers produced in the depletion layer are swept across by the electric field, thus creating an electric current. An even more important contribution to the current comes from charge carriers produced outside the depletion region and diffusing into it. The thickness of the detection volume, typically on the order of 0.06 mm, depends on the diffusion length of the charge carriers since a competing process allows electron-hole pairs to recombine before reaching the depletion layer. The current produced by the ionizing radiation is considered proportional to the absorbed dose and may be read with an electrometer. Even while unexposed to radiation, a small dark current may be measured and it is subtracted from the signal obtained during irradiation.

The advantage of diodes is their small detection size, high sensitivity and quasi-instantaneous response, which make them suitable for scanning. Diode sensitivity may change over a long time period due to accumulated radiation damage (Podgorsak, 2003). The response also shows variation with temperature (Saini and Zhu, 2002), angle of incidence and, in some cases, dose rate (Wilkins *et al.*, 1997). The silicon diode is not water equivalent. Figure 1.10 shows the mass energy absorption coefficient ratio and the restricted mass stopping power ratio with respect to water (Berger *et al.*, 2012a; Berger *et al.*, 2012b). The electron fluence perturbation may be significant because silicon has a higher cross-section for low energy photons. To adjust the energy response, the back of a photon diode is generally covered with a tungsten/epoxy layer that absorbs a certain

amount of low energy backscattered photons. This layer overcomes the increased sensitivity of the diode for photon energy below 400 keV but also introduces a more important directional dependence. Diodes manufactured without a filter (electron beam diode) are also occasionally used with photon beams (Beddar *et al.*, 1994) for cases where the directional dependence is more important than the variation in the proportion of low energy photons.

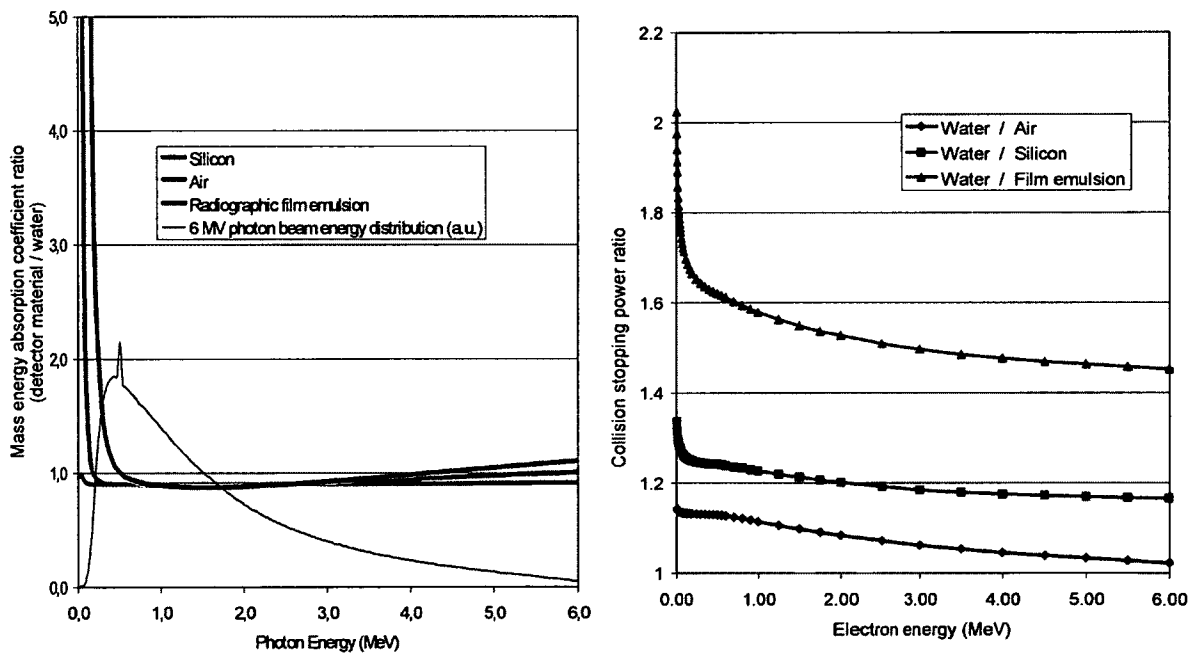


**Figure 1.10** On the left, mass energy absorption coefficient ratio for the various detector materials used in this work. The photon energy spectrum of a 10x10 cm<sup>2</sup> field size for a 6 MV photon beam is also plotted for comparison. On the right, restricted mass stopping power ratio for the various detector materials used in this work.

### 1.4.2.3 Radiographic film

A radiographic film consists of a thin transparent polyester base coated with a radiation sensitive emulsion (figure 1.11). The emulsion is composed of microscopic

crystals of silver halide (mostly silver bromide) dispersed in gelatin. A crystal of silver bromide is a regular cubical array of silver and bromide ions. In reality, the crystal is not perfect and there are local imperfections caused by impurities. Additionally, a small proportion of silver ions, referred to as interstitial silver ions, do not occupy the lattice

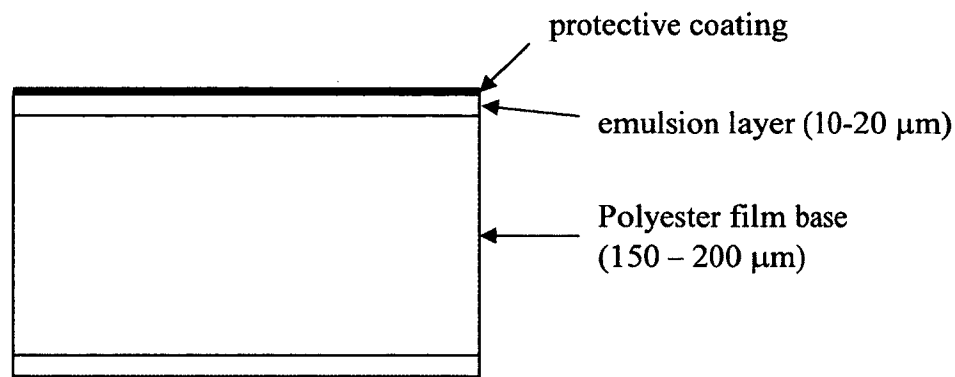


**Figure 1.11** Composition of a double-emulsion radiographic film showing the 10 - 20 μm thick radiation sensitive emulsion layer deposited on either side of a 150 - 200 μm polyester base.

positions but rather are located in the spaces between. Ionizing radiation oxidizes the bromine ions ( $\text{Br}^- \rightarrow \text{Br} + \text{e}^-$ ) and the released electrons are free to migrate about the crystal. As they do, they may encounter imperfections in the lattice and are trapped, giving the site a negative electric charge. This electric charge may attract the interstitial silver ions and reduce them to metallic silver (Curry III *et al.*, 1990). Once a silver halide crystal contains a threshold number of metallic silver atoms, which implies a minimum exposure to the photon beam, the crystal becomes developable and part of the latent image. There are, on the average, 5 to 10 crystals made developable per high-energy photon absorbed (Kodak, 2002).

Many materials undergo changes following exposure to photon beams and could conceivably be used to measure 2D dose distributions. The major advantage of radiographic film is that a few metallic silver reductions in a crystal may, by

development, be made to trigger the subsequent chemical deposition of some  $10^9$  or  $10^{10}$  additional silver atoms (Kodak, 2002). Development is essentially a chemical reaction, limited to developable crystals, where the silver ions are reduced and converted to metallic silver. The amplification process is sufficiently uniform and reproducible for relative dose measurement purposes. Following the development, the film is passed through a fixing solution that removes undevelopable silver halide crystals, leaving a clear and transparent film in their place.

Overall, the resulting film darkening and the absorbed dose are related to the concentration of metallic silver quantified in terms of optical density (OD). The later may be measured by shining optical light through the film and measuring  $I_o$ , the light intensity incident on the film, and  $I_t$ , the light intensity transmitted through the film. The decrease in optical light intensity through a thin slice of film is proportional to the concentration of opaque metallic silver. A simple differential equation describes the total decrease in light intensity through the total film thickness  $x$ .

$$\frac{dI}{dx} = -\alpha OD I \Rightarrow I_t = I_o e^{(-\alpha OD x)} \Rightarrow OD \propto \ln\left(\frac{I_o}{I_t}\right) \quad (1.5)$$

An unexposed developed film also has an optical density due to fogging and to the presence of the base. This optical density may be determined using  $I_t^*$ , the light intensity transmitted through an unexposed developed film:

$$OD_{\text{fog}} \propto \ln\left(\frac{I_o}{I_t^*}\right) \quad (1.6)$$

The absorbed dose is strictly proportional to the optical density related to radiation.

$$\text{Dose} \propto \text{OD}_{\text{rad}} = \text{OD} - \text{OD}_{\text{fog}} \propto \ln\left(\frac{I_0}{I_t}\right) - \ln\left(\frac{I_0}{I_t^*}\right) = \ln\left(\frac{I_t}{I_t^*}\right) \quad (1.7)$$

The coefficient of proportionality between the dose and the corrected optical density is determined by calibration. The calibration curve is a plot of known radiation doses vs. optical density. This curve is not perfectly linear and is usually fit with a polynomial instead of a linear relation. The gradual deviation from linearity of the film response is due to a saturation effect taking place when the dose is increased to a point where most of the silver bromide crystals are used.

Film dosimetry advantages include a high resolution and dose measurement in two dimensions. Disadvantages include response variation from one batch to the other, non-linearity (calibration curve) and susceptibility to temperature and chemical variations in the development process. The silver bromide emulsion is composed of relatively high atomic number atoms ( $Z=53$  and  $Z=35$ ) which makes it non tissue equivalent. Figure 1.10 shows the mass energy absorption coefficient ratio and the restricted mass stopping power ratio for the radiographic film emulsion.

#### **1.4.2.4 Cylindrical ionization chamber**

A cylindrical ionization chamber consists of a cavity with a central electrode surrounded by a conductive outer wall. The central electrode is separated from the wall by an

insulator to minimize leakage current when a polarizing voltage is applied (figure 1-12). In this work, an air filled cylindrical ionization chamber is used. When the chamber is irradiated, the electron fluence moves through the air cavity and ionizes the molecules, resulting in positive ions and free electrons. Most of the time, those free electrons are attracted to neutral molecules such as oxygen and form negative ions. An average energy of  $W = 33.97$  eV must be transferred from an electron to an air molecule to create an ion pair.

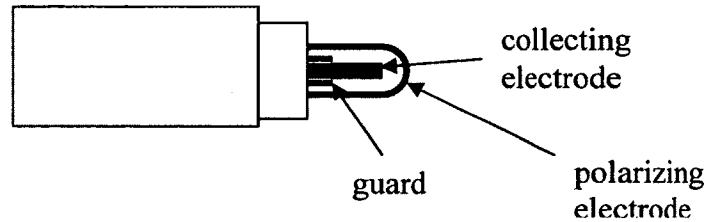


**Figure 1.12 Schematic diagram of a cylindrical chamber showing the central collecting electrode, guard ring and polarizing electrode.**

The ions are swept across by the electric field and the current is read by an electrometer. The absorbed dose in the cavity is proportional to the amount of charge collected  $Q$  in the air volume  $V$  of mass  $m_{air}$ :

$$D_{air} = \left[ \frac{Q}{m_{air}} \right] \left[ \frac{W}{e} \right]_{air} = \left[ \frac{Q}{\rho V_{air}} \right] \left[ \frac{W}{e} \right]_{air} \quad (1.8)$$

The advantages of ionization chamber dosimeters are a high stability, linearity, reproducibility, precision and a dose response independent of dose rate, angle of incidence and energy (Podgorsak, 2003). Air is a mixture having an effective atomic number close to water ( $Z_{air} = 7.6$  vs.  $Z_{water} = 7.5$ ). However, as explained earlier, the

density is considerably smaller than water (a factor of about 1000), which makes it non-water equivalent.

### 1.4.2.5 Phantoms

It is not possible to perform detailed in-vivo measurements in patients. Measurements that would be obtained in the patient are therefore carried out in tissue-equivalent materials called phantoms. Water is the most commonly used phantom material because it is easily accessible, cheap and approximately equivalent to soft tissues and muscles. Having a liquid phantom may be very useful for scanning dose profiles with dosimeters like diodes or ionization chambers. On the other hand, a liquid phantom is also cumbersome to set up and not very practical for dosimeters like radiographic film. To overcome this problem, different types of solid phantom material were designed by manufacturers. For a material to be considered water equivalent, it must have an effective atomic number  $Z_{\text{eff}}$ , a number of electrons per gram  $\rho_e$  and a mass density  $\rho_m$  close to that of water. Table 1.1 shows the characteristic of some commonly used phantom material.

**Table 1 Effective atomic number  $Z_{\text{eff}}$ , number of electrons per gram  $\rho_e$  and mass density  $\rho_m$  of the phantom materials (Kron, 1999).**

Phantom material	Effective atomic number $Z_{\text{eff}}$	mass density $\rho_m$ $\text{g/cm}^3$	number of electrons per gram $\rho_e$ (normalized to water)
Water	7.4	1	1
Solid Water	7.54	1.03	1.02
Acrylic	5.7	1.04	1.01
Delrin	6.96	1.41	1.36

### **1.4.3 Calculations of dose distributions**

#### **1.4.3.1 Convolution-superposition methods**

Dose calculations of external photon beams have been extensively studied in the literature and was the subject of a review (Ahnesjo and Aspradakis, 1999). Dose calculation algorithms plays a central part of the radiation therapy process because the physicist and the physician rely very heavily on their accuracy and known limitations to evaluate, modify and optimize treatment plans. Dose calculation algorithms may be divided in two classes: correction-based and model-based.

A correction-based dose calculation algorithm makes use of correction factors to modify the dosimetry functions to account for treatment conditions such as patient heterogeneities and irregular shapes. This method is adequate if the patient anatomy and the treatment fields are similar to the measurement conditions. This is generally not the case for SABR lung treatments because the lung anatomy is very heterogeneous and the effective treatment field sizes are often small and irregular (lack of lateral equilibrium). In those cases, model-based dose calculation algorithms, such as convolution-superposition (C/S) or Monte Carlo (MC) methods, are more appropriate and are currently considered the standard of care in most clinically used treatment planning system.

The simplest C/S method is the pencil beam algorithm. The pencil beam algorithm gets its name from the fact that the incident beam is divided into in many small pencil beams. Several types of pencil beam implementation are available and this section describes a simple one. The calculation is performed in fan line coordinate system to account for beam divergence and it is assumed that the photon beam is monoenergetic

and that the pencil beams are parallel and spatially invariant (figure 1.13). The dose distribution produced by a pencil beam in a semi-infinite water phantom is pre-calculated using Monte Carlo methods. It is stored in the treatment planning software in the form of a dose kernel  $A(x,y,d)$ , where the arguments  $x,y,d$  represent the distances from the pencil beam point of incidence and the point where the dose is absorbed. The dose distribution for the actual beam is calculated by convolving the pencil beam dose kernel with a pencil beam fluence matrix (equation 1.9).

$$D(x, y, d) = \iint \Phi(a, b) A(x - a, y - b) da db \quad (1.9)$$

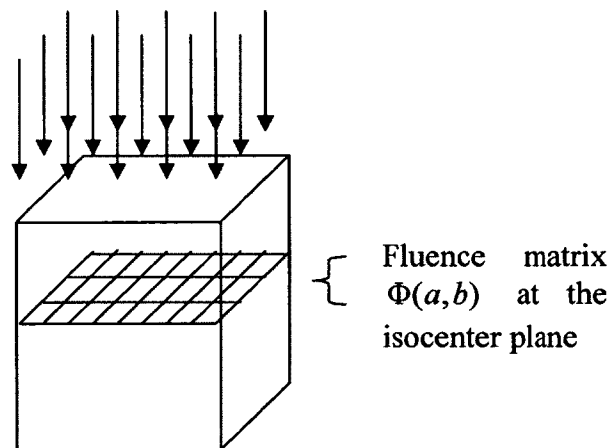


**Figure 1.13** A first approximation assumes that there is no beam divergence and that the pencil beams are parallel and spatially invariant.

The dose reduction due to beam divergence is corrected approximately by including an inverse square law correction factor to the equation 1.9. The fluence matrix in equation 1.9 is defined at the isocenter plane and represents the weight of each pencil beam. It contains values between 0 and 1, where 1 means that the collimator does not block the pencil beam fluence and 0 means that it is totally blocked. In reality, the pencil

beam fluence is never totally blocked by the collimator so the smallest matrix value used is the transmission value. Transmission values through the various collimators are required as input data by the algorithm.

A more accurate C/S method is referred to as point-kernel algorithm. Several types of implementation are available and this section describes a simple one. The calculation is also performed in a fan line coordinate system to account for beam divergence and it is assumed that the photon beam is monoenergetic. The dose distribution produced by a photon interacting at a point in the middle of a large sphere of water is pre-calculated using MC methods and stored in the treatment planning software in the form of a point-dose kernel  $A(r)$ . The dose distribution for the actual beam is calculated by convolving the spatially invariant point-dose kernel with the total energy release by primary photons at each points of the phantom. More specifically, the dose absorbed at a point  $r$ ,  $D(r)$ , from energy released at a point  $r'$  is given by the following equations (see figure 1.14) from (Papanikolaou *et al.*, 1993):

$$D(r) = \int T(r')A(r - r')d^3r' \quad (1.10)$$

$$T(r') = \frac{\mu}{\rho} \Phi_0 E e^{-\mu d'} \quad (1.11)$$

where  $A(r - r')$  is the convolution point kernel representing the relative energy deposited per unit volume about the site of primary photon interaction,  $T(r')$  represents the 3D distribution of the total energy released per unit mass,  $\mu/\rho$  is the photon mass attenuation coefficient,  $\Phi_0$  is the fluence at the surface of the phantom,  $d'$  is the depth along the vector  $r'$  from the surface to the phantom and  $E$  is the energy of the photon on the surface.

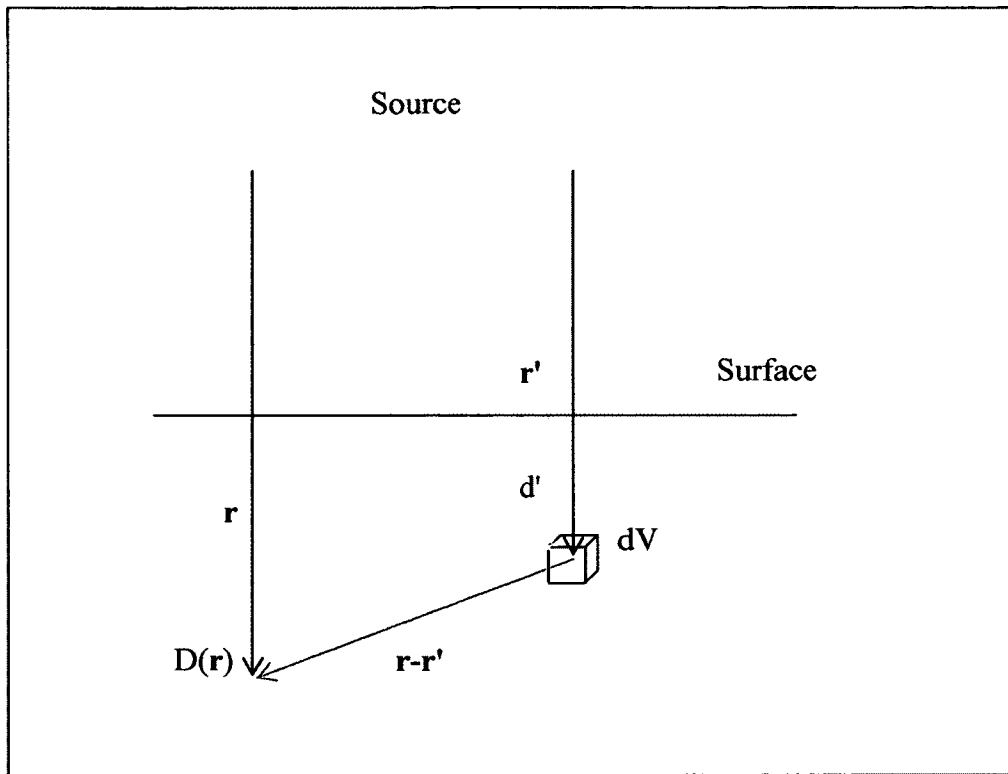


**Figure 1.14** Representation of the point kernel C/S dose calculation algorithm. Vector  $r$  shows the dose deposition point and the vector  $r'$  shows the site of primary photon interaction.

The dose reduction due to beam divergence is also corrected approximately by including an inverse square law correction factor to equations 1.10 and 1.11.

Both pencil beam and point-kernel C/S methods may be extended to account for polyenergetic photon beams, secondary sources (i.e., scatter dose from the head, electron contamination) and patient irregular contour (Ahnesjo and Aspradakis, 1999). Different methods also exist for point-dose kernel algorithms to include second order corrections (i.e., beam hardening, kernel tilting) and to speed up calculating time (collapse cone, variable dose grid, polyenergetic kernel, kernel inversion, long and small range kernel for scattered photons and electrons, graphic processor coding) (Miften *et al.*, 2000;

Papanikolaou *et al.*, 1993; Ahnesjo, 1989; Chen *et al.*, 2011). Finally, methods exist to account for tissue inhomogeneities and generally consist of adding the contribution (superposition) of spatially variant energy deposition kernel. The kernels are distorted by finding the average density along the straight-line path between the interaction site and the dose deposition site. Density scaling is a good approximation for scattered photons because photons travel in straight lines and the attenuation coefficient scales approximately linearly with density. For electrons, density scaling is a first order approximation since the path is more irregular, particularly in cases where the variation of density and material composition is large locally. In some clinical lung cases studied, dose calculated with convolution superposition algorithms were found to differ by more than 5% in the target when compared with more accurate methods such as MC algorithms (Vanderstraeten *et al.*, 2006).

#### **1.4.3.2 Monte Carlo methods**

A MC simulation consists of transporting a particle in a medium by simulating all interactions that the particle undergoes. The interactions and their outcomes take place according to known probability distributions sampled using quasi random numbers generated by the computer. The medium may have a complex geometry and composition, such as a linac and a patient, and it is generally divided into small voxels where stochastic physical quantities of interest are scored. For external photon beams, a rigorous simulation will transport a particle and its progeny from the entrance of the linac treatment head until they leave the volume of interest or until their energy falls below a specified cutoff value (ECUT for electrons and PCUT for photons). All secondary

particles created (or set in motion) by the interactions are also transported through the medium if their energy is above a specified threshold value (AE for electrons and AP for photons). The entire set of events carrying an initial particle and its progeny to the final state is called a history.

The uncertainty of a scored quantity  $x$  in a voxel of interest depends on the number of events taking place in the voxel. For a large number of histories  $N$ , the scored quantities converge to mean macroscopic quantities with stochastic uncertainties defined as follows (Walters et al, 2002):

$$\bar{x} = \frac{1}{N} \sum x_i \quad (1.12)$$

$$\sigma_{\bar{x}} = \sqrt{\frac{1}{N-1} (\overline{x^2} - \bar{x}^2)} \approx \frac{\sqrt{\overline{x^2} - \bar{x}^2}}{N^{1/2}} \propto \frac{1}{N^{1/2}} \quad \text{where } \overline{x^2} = \frac{1}{N} \sum_{i=1}^N x_i^2$$

The computing time required for each history is comparable so the uncertainty is also inversely proportional to the square root of the computing time. The simplest way to reduce this uncertainty is to increase the number of histories (computation time). Another easy way is to increase the voxel sizes at the expense of resolution so that transported particles have a higher probability to go through the voxels. Finally, a more sophisticated approach is to introduce modifications in MC codes to make them more efficient. These methods, referred to as variance reduction techniques, must be used with care since modifications of the particle transport physical reality must not significantly affect the scored quantities.

In general, there are six primary requirements to perform MC calculations of radiation dose distribution: i) interaction probability distributions (cross-sections) ii)

transport algorithms, iii) description of the medium geometry and composition, iv) reliable quasi random number generator algorithm, v) methods for scoring quantities of interest and vi) adequate computing power. The cross-section data, transport algorithm, scoring methods, quasi-random number generator and tools to model the medium are generally provided as part of a MC simulation system. A variety of systems are available for transport of different particles (electrons, photons, protons, positrons, neutrons, etc.) with different energy ranges. The next section provides more information about the XVMC and the EGSnrc systems used in this work.

#### ***1.4.3.2.1 BEAMnrc and DOSXYZnrc Monte Carlo simulation system***

BEAMnrc (Rogers *et al.*, 1995) and DOSXYZnrc (Ma *et al.*, 1996) Monte Carlo simulation systems are both built on the EGSnrc simulation code (Kawrakow, 2000; Kawrakow and Rogers, 2000), the last iteration of the EGS series. The former is designed to simulate photon and electron beams produced by linear accelerators, orthovoltage, and  $^{60}\text{Co}$  units. The latter is used to perform simulations and score doses in patient related geometries.

BEAMnrc provides a convenient and simple way to model the linac geometry by dividing the treatment head in independent geometrical units, each modeled with a component module (CM). A CM contains several subroutines specific to the geometry being modeled as well as subroutines to read the input file containing the materials and dimensions of each CM. The two most important subroutines are HOWFAR and HOWNEAR. Specifically, HOWFAR determines the distance along the particle's trajectory to the nearest boundary and HOWNEAR determines the minimum distance in

any direction to the nearest boundary (Bielajew, 1995). A boundary may be defined between two CMs but also between two regions located inside the same CM. To simplify distance calculations, the CM geometry is divided in a mesh of regions having very simple geometrical shapes each assigned with a medium index (figure 1.15). Many pre-coded CMs are available with BEAMnrc, going from simple ones (e.g., SLABS to model the target) to more complex ones (JAWS to model the linac jaws). Users may also code their own CM to model a particular unit (e.g., multi-leaf collimator). The subroutines are written in MORTRAN 3, a FORTRAN 77 preprocessor code allowing additional macro capabilities.

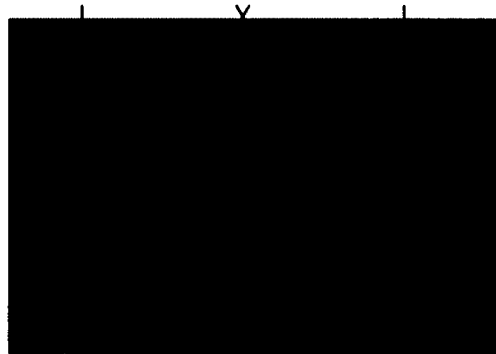


**Figure 1.15** An example of subregion assignment for a simplified flattening filter component module.

To perform a simulation, the first step is to build the treatment head by assembling different CMs in a certain order. The dimensions and materials of each CMs are written in the input file together with simulation parameters (e.g., number of histories, source characteristics, transport algorithm used, cutoff energies, variance reduction technique parameters). During compilation, the CM subroutines are added at the appropriate location to the main BEAMnrc code and a unique executable program is created for the

specific accelerator. When the program is run, it first reads the input file and then the material data file (also called PEGS file). The material data file contains detailed information about radiological properties of materials used (cross-sections, restricted stopping power, densities, atomic number, etc). Once the information required is loaded, BEAMnrc invokes EGSnrc routines to transport the incident particles through the treatment head and produces as its output a phase-space file. This phase space file contains the position, energy, charge, direction and history of interactions of all particles crossing a pre-specified scoring plane within the accelerator model. The phase space file is typically located at the bottom of the treatment head so that it may subsequently be used as a source for other MC simulation systems designed to perform simulations in patient related geometries. In certain occasions, the phase space file may also be reused as a source of particles for another BEAMnrc simulation. DOSXYZnrc is used in this work to read phase-space files or interactively sample BEAMnrc (Kawrakow and Walters, 2006) to obtain particles, to transport those particles in patient related geometries and to score absorbed dose. It is similar to BEAMnrc in the sense that it reads the same format of material data file and also uses EGSnrc routines to transport the particles. The patient (or a phantom) is modeled with a rectangular volume having designated voxel dimensions and materials. For example, to model a patient's head, all the voxels located outside of the head contour, but inside the rectangular volume, would be filled with air. The information about the rectangular volume size, the voxel definition and materials and the simulation parameters is contained in an input file read by the program.

#### ***1.4.3.2.2 XVMC Monte Carlo simulation system***

XVMC (X-ray Voxel Monte Carlo) (Fippel, 1999; Kawrakow and Fippel, 2000; Kawrakow *et al.*, 1996) is a fast MC simulation system used to perform simulations in patient related geometries and score absorbed dose. It is about 20 times faster than DOSXYZnrc because it makes multiple use of simulated histories. It also contains some simplifications in the boundary crossing algorithm and the electron multiple scattering theory. Those simplifications are only valid within the electron energy range (1-30 MeV) and phantom material ( $\rho < 3 \text{ g/cm}^3$ ) typically used in radiotherapy. Employing the same history to different sections of the phantom also has some limitations; these sections should be sufficiently far away from one another so that the history taking place in one section has no influence on the other section.

The patient (or a phantom) is modeled with a rectangular volume having designated voxel dimensions and density. The information about the rectangular volume size, the voxel definition and density and the simulation parameters is contained in an input file read by the program. There is no material data file for XVMC since only the density of the voxel is specified. The data required to perform the simulation (i.e., cross-sections, restricted stopping powers) are calculated using simplified relationships valid within limits specified above.

### ***1.5 Stereotactic ablative radiotherapy (SABR) lung treatment***

In 2011, an estimated 177,800 new cases of cancer and 75,000 cancer deaths are expected in Canada. Lung cancer remains the leading cause of cancer death (27%) in both men and women (NCIC, 2011). Lung cancers may be classified into two groups: non-small

cell lung cancer (NSCLC) and small cell lung cancers (SCLC). The 5-year survival rate is estimated to be 16% (NCI, 2011) and about 61% of cases require treatment with radiotherapy (Tyldesley *et al.*, 2001). The stage of disease serves as a guide for treatment modality and prognosis. According to the American Joint Committee on Cancer, stage 1 lung cancer includes tumours of less than 3 cm diameter surrounded by lung or visceral pleura, without bronchoscopic evidence of invasion in the main bronchus (T1). It also includes tumour that involve the main bronchus at less than 2 cm distal to the carina but without involvement of the carina, associated atelectasia or obstructive pneumonitis of the entire lung (T2). In both cases, there should be no regional lymph node metastasis or other distant metastasis. SABR lung treatments for stage 1 non-small cell cancers has recently been shown to result in superior local control rates compared with conventionally fractionated radiotherapy (5-year survival 42% vs. 20%) (Grutters *et al.*, 2010). SABR lung treatment is defined here as a combination of many beam angles to achieve sharp dose gradients, high precision localization of the target, and a high dose per treatment fraction.

Linac-based SABR lung treatments are planned in several steps. The first step is to obtain a three-dimensional representation of the patient geometry (densities, composition) and metabolic processes (e.g., glucose uptake). This is obtained from images acquired by computed tomography (CT) and positron emission tomography (PET) as shown by figure 1.16. The target volumes, normal tissues and related safety margins are then contoured on the patient geometry using standard contouring nomenclature (ICRU, 1993) for gross target volume (GTV), clinical target volume (CTV) and planning target volume (PTV). SABR lung treatments are generally given in 3 to 5

fractions with a high radiation dose per fraction (12-18 Gy) to achieve sterilization of the lesion. The relatively high doses used require a very sharp dose fall-off outside of the target volume to spare the surrounding normal tissues which may include vital radiosensitive structures. This is achieved by conforming the beams to the target volume with the use of collimating devices and by irradiating the target with several or continuous converging beam orientations as shown by figure 1.17.

The next step is to optimize the arrangement of photon beams to ensure that the PTV receives the prescription dose and that normal tissues are not receiving dose in excess of prescribed limits. The treatment planning optimization process is computer assisted and consists of first choosing the number of beams (or arcs), their orientations

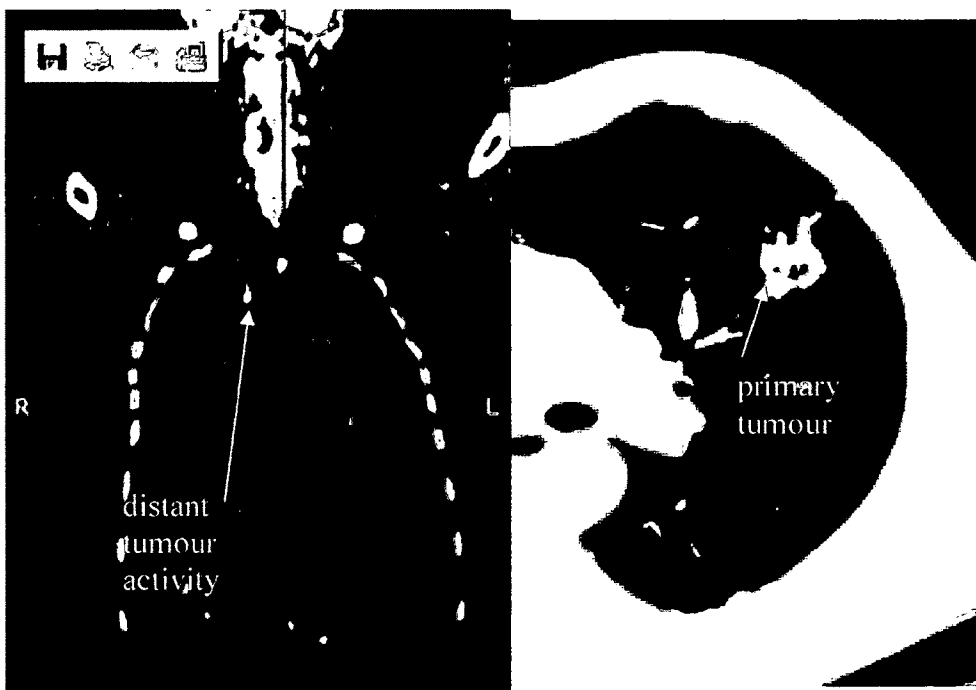


**Figure 1.16** Coronal view of patient voxelized geometry (left). The gray values are representation of the computed tomography densities and the color values are representation of the positron emitted tomography glucose uptake. The right image is a transverse view of the patient densities where the tumour is clearly visible in the lung.

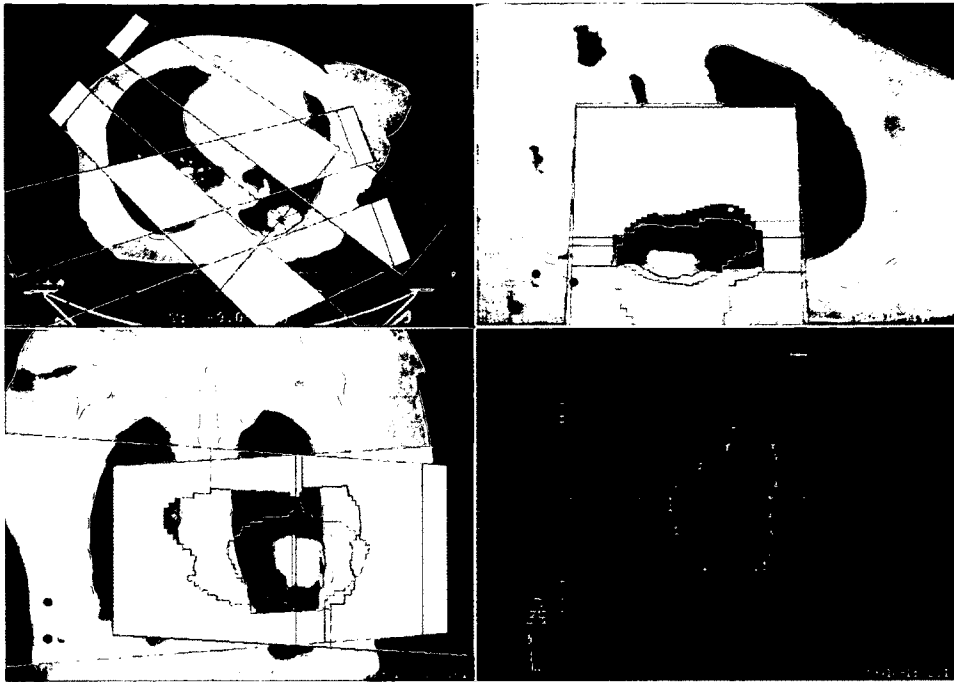


**Figure 1.17** Transverse (upper left), coronal (bottom left), sagittal (upper right) and beams-eye-view (bottom right) representation of the patient densities with two beams conforming on the planning target volume. Other beams are not shown for clarity.

and the field shapes. For each beam configuration, the software uses an algorithm and dosimetry functions to calculate the dose distribution inside the patient. The plan evaluation is carried out with standard tools provided by the software, which allows the user to inspect quantitatively and qualitatively the volumetric dose distribution with regards to each outlined structures, i.e., a dose volume histogram (DVH). The optimization of the plan is a trial-and-error process that varies depending on the complexity of the case and the experience of the user. The optimization may also be automated with inverse methods to minimize an objective function determined from planning objectives. This approach is used for more complicated clinical cases having numerous conflicting trade-offs and/or for cases requiring the use of intensity-modulated radiotherapy treatment (IMRT). IMRT consists in modulating continuously or

sequentially the 2D photon fluence intensity within each beam, which allows a more conformal dose distribution. Once the treatment plan is completed, the patient is positioned on the linac treatment couch and radiographic images are acquired to register the patient and improve the positioning accuracy.

Treating small target volumes is challenging because of issues related to target localization, target positioning and dose delivery. The two first issues are related to the diagnostic image quality, the volume delineation uncertainties and the registration process. The third issue is related to the stability of the treatment unit but also to the validity of the treatment planning dose calculations. The latter is the basis of this thesis that aims to evaluate the uncertainty of the dose distributions calculated by treatment planning software for SABR lung treatments.

## **1.6 Patient motion**

### **1.6.1 Setup motion**

Patient motion has an important impact on the accuracy and the quality of SABR lung treatment. For the purpose of this discussion, the motion is divided in two types: setup motion and respiratory motion. Setup motion refers to the patient positioning on the treatment couch before starting the treatment while respiratory motion refers to the intra-fraction motion (patient anatomy changing during the course of treatment).

Setup motion error is minimized with the use of immobilization devices (i.e., lung board, pillow) to make the patient positioning comfortable and reproducible. At the time of treatment planning image acquisition, tattoos are drawn on the patient skin to indicate

the image isocenter which may be identified at the intersection of coronal, transverse and sagittal lasers in the imaging room. The position of the tattoos may be visualized in the reconstructed 3D images by placing fiducial markers on the tattoos. At the time of treatment, the lasers in the treatment room are used to align the patient tattoos with the linac isocenter. The couch is then further moved to position the linac isocenter at the same patient location as reported in the treatment plan. For example, if the treatment plan image isocenter is located 2 cm inferior (towards the feet) to the linac isocenter, the couch has to be moved 2 cm inferior after the tattoo registration. Patient position is further validated by acquiring images before the start of treatment delivery, performing image registration and investigating any cause of anatomical changes (i.e., loss of weight, immobilization device setting changes).

### **1.6.2 Image registration**

Image registration is the process of deriving an optimal spatial transformation to map the features (e.g., pixel intensity) of a source image to those of a reference fixed image. This transformation is applied to the source image to align it geometrically with the reference image to facilitate direct comparison (i.e., comparing the patient anatomy in the planning images with the patient anatomy on the treatment couch before treatment delivery). Rigid registration (3 translations, 3 rotations) is often used in radiation therapy for diagnostic purposes, organ delineation and patient positioning but the method is limited by several factors (e.g., patient posture, anatomy modifications, breathing motion) that may change the anatomy or move different parts of the body in different places from one time to another. The topic is particularly relevant to SABR lung treatment where there may be a

requirement to register anatomy from one breathing phase to another (i.e., exhale to inhale) using four dimensional computed tomography images (see section 1.6.3.1). In those cases, rigid registration may be followed by a non-linear registration or deformable image registration (DIR) to determine residual local differences. DIR is an active area of investigation in 4D imaging and radiotherapy planning applications (Niu *et al.*, 2012; Al-Mayah *et al.*, 2010; Brock, 2010) and was shown to improve registration accuracy. Non-linear registration is challenging because of the non-existence of image correspondence in some clinical cases (i.e., weight loss, intestinal filling, noise) which requires the use of converging strategies to deal with the degenerate solution space.

A non-linear registration contains a higher number of degrees of freedom to allow local deformation of images. There are several ways to represent the results of a non-linear registration. For example, the deformation may be represented as a deformable vector field (DVF) defined at each image point or at sparse control points combined with interpolation methods (e.g., spline). Non-linear registration may be characterized by the image modality (i.e., CT to CT, CT to MRI, PET to CT), the inverse consistency (image 1 to 2 gives the same result as image 2 to 1), the similarity metric, the optimization method and the transformation model. Transformations should also be ideally diffeomorphic (one-to-one, continuous, differentiable), insensitive to noise level and relatively efficient in terms of computing time.

The similarity metric is used to quantify the match between two images in the optimization process. For example, the DIR used in this work is based on a mean-square-error (Thirion, 1998) similarity metric to minimize the image intensity differences

between two images. Other metrics based on points (Kessler *et al.*, 1991), lines (Balter *et al.*, 1992) or surfaces (van Herk and Kooy, 1994) were also reported.

The transformation model is used to put constraints (regularization) on the allowed transformation (i.e., vector field). For example, the DIR used in this work is based on an optical flow model (Thirion, 1998; Yang *et al.*, 2008; Horn and Schunck, 1981) to calculate the velocity field between two images assumed to have the same intensities (but not at the same location). Other transformation based on thin-plate/B-splines (Brock *et al.*, 2003; Rietzel and Chen, 2006), demon/diffusion model (Thirion, 1998), elastic/viscous fluid (Christensen *et al.*, 1994) or finite-element model (Brock *et al.*, 2005) were also reported in the literature.

The optical flow transformation proposed by Horn and Schunck registers two images (two time points) by solving for the velocity distribution of high contrast objects moving from one image to the other, based on the object intensities. The velocity field is equivalent to the deformation field. The model relies on the assumptions of constant image intensities  $I(\vec{r}, t)$  and small displacements or deformations ( $\sim$ voxel size). Based on this approximation, the velocity field  $\vec{v}$  is solved using the following Taylor expansion:

$$I(\vec{r}, t) \approx I(\vec{r} + \delta\vec{r}, t + \delta t) \approx I(\vec{r}, t) + \vec{\nabla}I \cdot \delta\vec{r} + \delta t \frac{\partial I}{\partial t} \quad (1.13)$$

The terms  $I(\vec{r}, t)$  on each side of the equation correspond to the two images and do not necessarily cancel because of image noise or deformation. The subtraction of both terms is replaced by an error term  $\varepsilon_1$  and both sides of the equation are divided by  $\delta\vec{r}$ . Using

$\frac{\partial I}{\partial t}(\vec{r}, t) = 0$  (assumption of constant image intensities), we obtain:

$$\left( \bar{\nabla} I \cdot \bar{v} + \frac{\partial I}{\partial t} \right) (\vec{r}, t) = \left( \bar{\nabla} I \cdot \bar{v} \right) (\vec{r}, t) = \frac{\partial I}{\partial x} v_1 + \frac{\partial I}{\partial y} v_2 + \frac{\partial I}{\partial z} v_3 = \varepsilon_1 \quad (1.14)$$

The assumption of small displacements requires the use of multi-resolution (or multigrid) strategies. Such strategies consist of performing the registration first on low resolution images and then gradually moving to higher resolution images. Equation 1.14 also requires a regularization term  $\varepsilon_2$  to control the smoothness of the velocity field and allow convergence to a unique determination of the velocity field. This term consists of a minimization of the square magnitude of the optical flow velocity gradients:

$$\varepsilon_2 = \sum_{i=1}^3 \left( \left( \frac{\partial v_i}{\partial x} \right)^2 + \left( \frac{\partial v_i}{\partial y} \right)^2 + \left( \frac{\partial v_i}{\partial z} \right)^2 \right) \quad (1.15)$$

The velocity field is determined by minimizing both  $\varepsilon_1$  and  $\varepsilon_2$  over the image volume  $V$ :

$$\varepsilon_{\min} = \iiint (\varepsilon_2^2 + \alpha \varepsilon_1^2) dV \quad (1.16)$$

The constant  $\alpha$  is used to set the relative importance of  $\varepsilon_1$  (image matching) and  $\varepsilon_2$  (regularization or smoothness). Equation 1.14 to 1.16 may be solved to give the following optical flow iterative equation:

$$\bar{v}(\vec{r})_{k+1} = \bar{v}(\vec{r})_k - \left( I_d + \bar{v}(\vec{r})_k \cdot \nabla I \right) \nabla I / \left( \alpha^2 + |\nabla I|^2 \right) \quad (1.17)$$

where  $\bar{v}(\vec{r})_{k+1}$  is the vector field at the end of iteration  $k+1$ ,  $\bar{v}(\vec{r})_k$  is  $\bar{v}(\vec{r})_k$  averaged in the neighborhood of each pixel,  $I_d$  is the difference between image 2 and image 1,  $I$  is the image 1 and  $\nabla I$  is the gradient of image 1. The advantage of the optical flow method is fast convergence and high efficiency (~minutes).

### **1.6.3 Respiratory motion**

The magnitude of target motion due to breathing has been measured to be on average 1.0 cm (Seppenwoolde *et al.*, 2002) and up to 5 cm (Keall *et al.*, 2006) for some patients. The average breathing period is 4 seconds (Shirato *et al.*, 2004) and the motion is greater in the lower lobes of the lung. The motion is mostly in the superior/inferior directions and may exhibit hysteresis. The AAPM Task Group 76 (Keall *et al.*, 2006) investigated the impact of respiratory motion and identified three areas of concern: organ delineation error caused by motion artifacts in images, treatment planning strategies to ensure adequate target coverage and dose delivery errors.

#### **1.6.3.1 Effect of motion on image acquisition**

The severity of motion image artifacts for 3D-CT was studied by several groups (Balter *et al.*, 1996; Gagne and Robinson, 2004; Shimizu *et al.*, 2000; Evans *et al.*, 2006) and was shown to lead to potential failure to cover properly the target over its full range of motion (Henkelman and Mah, 1982; Engelsman *et al.*, 2001; Chetty *et al.*, 2004). Several studies linked this failure to the inappropriate use of margins in the treatment plans (Mechalacos *et al.*, 2004; Flampouri *et al.*, 2006; Nioutsikou *et al.*, 2006; Rosu *et al.*, 2005; Rosu *et al.*, 2007). To improve the accuracy of a tumour motion assessment, four dimensional CT imaging (4D-CT) was gradually introduced into clinical services over the last 10 years. The method consists of over-sampling the set of projections during the CT acquisition and simultaneously recording the patient respiratory signal. The projections are sorted by breathing phase or amplitude before reconstructing the images. Earlier 4D-CT methods were proposed for single slice CT scanners and were limited to

small image extent due to tube heating issues (Ford *et al.*, 2003). The introduction of multi-slice CT scanners made it possible to overcome this issue using both axial and helical scanning mode (Keall *et al.*, 2004; Pan, 2005). Different approaches may be used with 4D-CT to monitor indirectly breathing phases including external markers on the abdomen (Berlinger *et al.*, 2006; Pan, 2005), strain gauges to measure abdomen expansion (Kleshneva *et al.*, 2006) and spirometry to measure air intake (Low *et al.*, 2003). Regardless of the method, the accuracy of the treatment depends on the feasibility for the patient to reproduce similar breathing patterns during treatment delivery (Guckenberger *et al.*, 2007), which is frequently not the case in practice.

Patient-specific internal target volume (ITV) margins may be derived manually or automatically from the 4D-CT images by combining target contours drawn on individual breathing phase CT scan (Ragan *et al.*, 2005; Gagne *et al.*, 2005) and/or by contouring the ITV directly on composite 4D-CT images generated using maximum, minimum or average pixel intensity from all breathing phases (Bradley *et al.*, 2006). The plan dose calculation is usually performed on the average pixel intensity images. It may also be performed on a specific breathing phase scan or even on a free breathing CT scan if the 4D-CT images are not covering enough anatomy in the superior-inferior direction.

### **1.6.3.2 Management of motion in treatment planning and delivery**

Different approaches may be used to account for respiratory motion using the target contours: forced shallow breathing (McGarry *et al.*, 2005), breath hold techniques (Rosenzweig *et al.*, 2000; Stock *et al.*, 2006; Murphy *et al.*, 2002; Nakamura *et al.*, 2007), gating (Ahunbay and Li, 2007) and respiration-synchronized techniques. The

latter is a more sophisticated approach and eliminates partially the need for internal margins by predicting target motion during treatment delivery and changing the beam configuration to adapt to the motion (Murphy, 2004; Schweikard *et al.*, 2000; Keall *et al.*, 2001a). Regardless of the approach used, an appropriate choice of safety margin around the target volume (and in some case normal tissue structures) is an essential component to account for target motion and residual uncertainties. Treatment planning optimization is usually performed in the clinic using fixed target volume (e.g., ITV) with an additional safety margin for other errors (e.g., setup motion). Several research initiatives have reported treatment plan quality improvements by incorporating respiratory motion uncertainties directly in the plan optimization algorithm as opposed to using static margins (Heath *et al.*, 2009; Nohadani *et al.*, 2010). These techniques generally rely on the assumption that each segment of the treatment delivery will be equally distributed on each breathing phase over multiple fractions. This assumption is not valid for hypofractionated treatments such as SABR lung treatments.

### **1.6.3.3 Effect of motion on treatment delivery**

A study (Bortfeld *et al.*, 2004) summarized three effects of motion on the delivered dose: blurring along the path of motion, spatial deformation of the dose and interplay effects. Dose blurring results in a broadening of the beam penumbra and lowers the conformality of the dose distribution. Dose deformation is localized and occurs because of the deformation of the patient anatomy. Finally, the interplay effect occurs in dynamic beam deliveries and is caused by the combination of organ and machine motion as shown by figure 1.18.

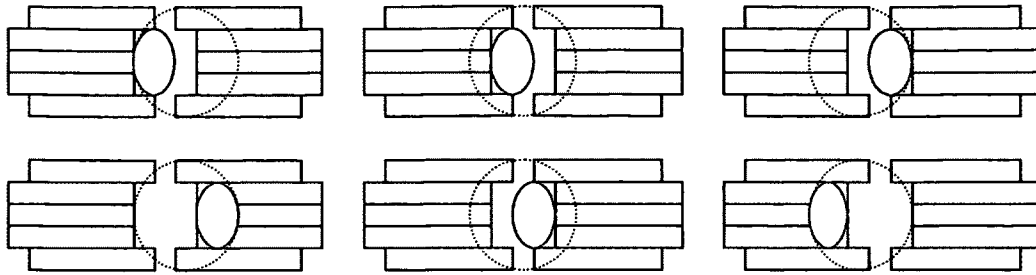


**Figure 1.18** Illustration of the interplay effect between a target volume and a multi-leaf collimator. The leaves are sweeping to the right to uniformly cover the internal target volume (blue). The target volume (red) is moving from left to right in the first delivery (top) and from right to left in another delivery (bottom). The dose received by the target volume depends on the relation between the motion of the target and the motion of the leaves. The target is receiving more dose in the first delivery than in the second delivery.

The interplay effect was studied analytically (Bortfeld *et al.*, 2002; Yu *et al.*, 1998) and the authors concluded that the interplay effect was small (1% to 2%) for conventional IMRT treatments delivered over several fractions (~30), a conclusion that was also confirmed experimentally (Ehler *et al.*, 2007; Schaefer *et al.*, 2004; Ong *et al.*, 2011). Another experimental study reported physical dose variation of up to 20% in the target volume for a single fraction but the estimated impact on the tumour control probability was less than 5% (Duan *et al.*, 2006). Seco *et al.* (Seco *et al.*, 2007) also reported an analytical study where the risk of a dose error of more than 1% was estimated to be 7% for two clinical cases. The authors also mentioned the possibility of dose deviations on the order of 20% for treatment delivered over multiple fractions when using mostly small low MU segments for IMRT delivery. Similar contradictory information is available from studies of the interplay effect on HT treatments. For example, (Kissick *et al.*, 2008) did not find clinically significant dose deviation due to the interplay effect while (Kim *et al.*, 2009) reports the possibility of getting dose deviation between 7% and 29% for some cases studied.

As reported by Bortfeld *et al.* (Bortfeld *et al.*, 2004), a frequent assumption in several analytical studies is that the motion is approximately sinusoidal and not correlated with beam delivery. This assumption may be questionable for hypofractionated treatments. In addition, a real patient breathing cycle is a non-stationary state and is not necessarily sinusoidal. This cycle is often difficult to model since it may exhibit various patterns, changes of amplitude and period, change of target mean position, baseline drift and envelope effects (Seppenwoolde *et al.*, 2002; Ozhasoglu and Murphy, 2002). In general, it is possible to use dynamic treatment planning strategies to minimize the risk of significant interplay effect ( $> 2\%$ ). However, it may not be possible to exclude completely the possibility of finding cases where the interplay effect is important, which explains the contradictory finding of multiple studies.

More recently, several groups reported the incorporation of realistic respiratory signals in dose calculations or measurements to make the results more representatives of actual SABR lung treatments. For example, a group (Court *et al.*, 2010) reported the use of anthropomorphic breathing phantom measurements performed with a resin tumour (copy of the patient tumour) and patient recorded respiratory motion. They studied different treatment techniques and the average standard deviation in the target for 5 treatments was found to be between 1% (3D conformal) and 4% (VMAT) of the expected dose. Other studies (Oliver *et al.*, 2008b; Oliver *et al.*, 2008a; Litzenberg *et al.*, 2007; Panettieri *et al.*, 2007) reported methods to incorporate patient motion in Monte Carlo simulation by approximating the tumour motion as a rigid body displacement or by equivalently shifting as a function of time the position of the transported particles with respect to the patient (in the direction opposite to the patient motion). (Waghorn *et al.*,

2010; Waghorn et al., 2011) introduced a similar method using a treatment planning system by shifting IMRT fluence map instead of particles. Recently, (Rao et al., 2012) reports the use of deformable image registration (DIR) to calculate the interplay effect for VMAT SABR lung treatments using 4D-CT images. In their study, the patient motion for each discretized treatment segments or sub-arcs was assigned to one of the 10 available 4D-CT images. The patient and the machine motion were thus modeled as discrete steps and the interplay effect was found to be less than 1% of the prescription dose. Another group (Jensen *et al.*, 2012) performed a similar study (without patient anatomy deformation) using MC methods, measurements and log files. Their study was performed on a moving phantom and also included comparison with other methods (i.e., particle shift) to study the impact of discretizing the patient motion in 10 steps using the available 4D-CT images.

In addition to the publication (Rao *et al.*, 2012) discussed above, many other groups (Ehler and Tome, 2008; Flampouri *et al.*, 2006; Guo *et al.*, 2011; Huang *et al.*, 2010; Vinogradskiy *et al.*, 2009) have used DIR in dose calculation to map dose back from each breathing phases to a reference phase. The use of DIR allows more realistical calculation of the effect of motion on the full patient anatomy (and not only the target). In most publications, the approach used does not permit interplay effects to be accounted for as it assumes that it will smear out over the course of several fractions. Other authors also reported methods to include the deformable vector fields (DVF) as part of the MC simulation to deform the voxels or map the energy deposition interactively (Heath and Seuntjens, 2006; Siebers and Zhong, 2008; Heath *et al.*, 2011; Peterhans *et al.*, 2011; Paganetti *et al.*, 2004). However, similar smearing approximations were also implied in

the few examples provided in the publications to demonstrate the feasibility of their methods. To our knowledge, the dose calculation studies performed by (Paganetti *et al.*, 2004; Rao *et al.*, 2012) are the only ones incorporating deformation of the patient, full heterogeneity correction and discretized interplay effect between the machine and the patient motion. The first study (Paganetti *et al.*, 2004) was specific to lung proton treatment and the second study was specific to SABR lung treatment using VMAT. In both cases, the patient anatomy was modified for each treatment segment (or sub-segment) in the dose calculation process by choosing one of 10 possible voxelized geometries based on the available 4D-CT images.

## **1.7 Thesis outline**

Treating small lung tumours with high precision is challenging because of issues related to target localization, target positioning and dose delivery. The two first issues are related to the diagnostic image quality and the registration process. The third issue is related to the accuracy of the dose delivery but also to the validity of the treatment planning dose calculations. The latter is the basis of this thesis that aims to evaluate the uncertainty of SABR lung treatment dose distributions calculated by commercial treatment planning systems. The recent use of improved treatment techniques that reduce the treatment delivery time and may reduce the risk of late toxicities is the subject of many ongoing investigations. As discussed previously, a challenge with many of those techniques is the difficulty of incorporating intra-fraction organ deformation in the dose calculation algorithms to generate more accurate and realistic dose distributions. The dosimetric impact of intra-fraction organ motion for SABR lung treatments has been studied by

several groups in the past using measurements, planning studies or a combination of both. The aim of this study is to calculate for the first time realistic dose distributions that include the continuous motion of both organs and treatment delivery unit using 4D MC methods for both VMAT and HT treatments. The particularity of this 4D MC method compared with previous studies is that it does not rely on discrete (step-like) motion of the organs or the machine, includes 3D dose distributions with full heterogeneity corrections and avoids the cumbersome use of repetitive measurements. SABR lung treatments delivered using a robotic treatment unit (tumour tracking) is not covered in this work and will be addressed in future work.

The thesis is structured as follows. Chapter 2 describes the modeling of the treatment units. To do so, we present a method to perform full position-probability-sampled MC dose calculations in the BEAMnrc and DOSXZYnrc user codes of EGSnrc. The method includes for the first time full accelerator head simulation of conventional and HT treatment units and a realistic representation of machine continuous motion via the sampling of a time variable for dynamic treatment delivery technique such as helical tomotherapy or volumetric modulated arc therapy. Chapter 3 describes for the first time a method to model using 4D MC the continuous motion and deformation of the patient geometry . To do so, we implement in the user code two methods (density interpolation, density mapping) to update the patient geometry (transport grid densities) as a function of time and two methods (voxel average, voxel center) to map back the energy deposited in the time dependant transport grid to a reference grid. We then derive correction factors to account for non-ideal deformable vector field inverse consistency and mass conservation. Finally, we provide information on the tests and measurements performed to validate the

implementation of this method. One of the tests is to use for the first time 4D MC simulations to calculate the dose as a function of time in a moving phantom irradiated with a dynamic treatment delivery technique. This test was used for validation purposes but also represent a first step to quantify parameters to be used to calculate dose for each patient treatment for adaptive purposes. Finally, MC methods developed in Chapter 2 and 3 are applied in Chapter 4 to study more specifically the impact of intra-fraction motion for SABR lung treatments.

## 2 Treatment unit modeling

### 2.1 Introduction

The accuracy of dose calculation algorithms used in most treatment planning systems (TPS) is limited by approximations used in the characterization of the radiation beam as well as approximations used to model the coupled electron-photon transport in complex heterogeneous media. The topic was superficially covered in a previous section of this thesis (section 1.4.3). MC dose calculation algorithms are widely recognized as the gold standard (Vanderstraeten *et al.*, 2006) for calculating dose distributions as the transport of particles through the accelerator head and the patient heterogeneous geometry may be modeled explicitly. Another advantage of MC calculation algorithms is their relative immunity in terms of efficiency to the effect of time discretization to account for treatment fraction, patient motion and moving parts of the accelerator during IMRT. Residual inaccuracies may nevertheless exist in MC dose calculation which are inherent in the method (statistical noise) or directly linked to approximations used in cross-section modeling, charge particle condensed history algorithms and geometrical description of the medium.

MC-based dose calculation methods were discussed in general terms in section 1.4.3.2 but no specific example of application was given. In the past, MC methods have been implemented for various fixed-beam IMRT techniques including step-and-shoot IMRT techniques (Ma *et al.*, 2000; Laub *et al.*, 2000) and sliding window IMRT techniques (Liu *et al.*, 2001; Keall *et al.*, 2001b; Heath and Seuntjens, 2003). MC-based methods have also been implemented for standard arc treatments using stereotactic

radiosurgery cones (Solberg *et al.*, 1998)<sup>7</sup> or fixed MLC opening (Solberg *et al.*, 1998; Chow *et al.*, 2003). Interest in the use of MC dose verification methods are spurred by the recent release of VMAT techniques and the growing number of HT users. MC methods are particularly well suited to the complexity of these treatment modalities, and may improve treatment planning studies by enabling further investigation of the impact of machine tolerance and patient motion on dose distributions. Li *et al.* (Li *et al.*, 2001) first demonstrated the feasibility of using MC methods for verification of VMAT dose distributions (RenderPlan, Elekta) with a technique that approximated the modulated arcs as a series of static apertures with a gantry angle spacing of 5 to 10 degrees. More recently, Bush *et al.* (Bush *et al.*, 2008) implemented a MC method for dose verification of a VMAT technique having additional degrees of freedom (RapidArc<sup>TM</sup>, Varian Medical Systems). They used a gantry angle spacing identical to the one used in the treatment planning system (~2 degrees) and included dose rate variation and MLC dynamic motion in their simulation for each static arc projection. MC dose verifications methods were also implemented at about the same time for HT deliveries. Zhao *et al.* (Zhao *et al.*, 2008) approximated the helical deliveries as a series of static apertures with the same angle spacing as used in the treatment planning system (~7 degrees). They included the simulation of several static apertures at each gantry angle to fully represent the opening and closing of the leaves inside each HT projection. In a similar work, another group (Sterpin *et al.*, 2008) chose to assign a more realistic gantry angle to each static aperture composing the arc projections, equivalent to using a finer gantry angle spacing to approximate the continuous motion.

In MC methods, there are two approaches that may be used to simulate the simultaneous variation of multiple parameters (i.e., MLC, jaws, gantry, couch, dose rate, patient motion, etc...). A more rudimentary approach consists of approximating the continuous variation as fixed discrete projections and simulating each of those projections individually before adding all the results as a final step. This approach, referred to as static-component simulation (SCS) (Verhaegen and Liu, 2001; Liu *et al.*, 2001) may become cumbersome if there is a need to steer and track the simulation of a large number of projections. The number of projections depends on multiple factors including the desired dose calculation accuracy, the treatment technique (i.e. ~30 to 200 projections for VMAT and step-shoot IMRT and ~18,000 to 500,000 projections for HT) and the time sampling correlation between the various parameters (i.e. breathing motion and MLC motion are uncorrelated). The word projection used alone here refers to the number of leaf configuration changes or arc segments rather than the usual ~7 degrees "tomotherapy projection". The number of projections therefore includes several leaf configuration changes per "HT projection". Another approach, referred to as position-probability-sampling (PPS) (Liu *et al.*, 2001; Paganetti, 2004; Verhaegen and Liu, 2001) consists of using a time randomized variable during a simulation to sample and interpolate for each history the required parameters using analytical functions or interpolating tables. In practice, both methods are used at various levels in most simulations and their implementation typically depends on the needs and the available features of the MC code used in the implementation.

There are also several MC approaches regarding the accelerator head simulation. Several general purpose MC codes are suitable to produce phase space files of particles

based on full simulation of the geometrical model of the accelerator head: BEAMnrc ((Rogers *et al.*, 1995), MCNP (Briesmeister, 2000), Penelope (Salvat *et al.*, 2003), Geant (Agostinelli, 2003). To reduce computation time, the simulation results of the static part of the accelerator head are often stored in a phase space file to simulate separately the beam modulators (MLC, jaws, etc...) using the same MC package or using an analytical procedure involving drastic approximation in the photon transport (Sterpin *et al.*, 2008; Keall *et al.*, 2001b). Besides full MC accelerator head simulation, a compressed representation of a phase space file may also be generated using simplified models based on a virtual source representing the main components of the treatment beams by a set of analytical functions or interpolating tables. This approach involves more approximations but it is faster and particularly useful when the details about the accelerator head geometry are not available (Sikora *et al.*, 2007; Fippel *et al.*, 2003; Ma and Rogers, 1995).

This chapter describes the development of a method for performing a complete PPS MC dose calculation for verification of photon treatment using the BEAMnrc / DOSXYZnrc code. This method is similar to the one used by (Paganetti, 2004) with the GEANT4 code for proton beam and builds on previous work done by (Verhaegen and Liu, 2001; Liu *et al.*, 2001; Heath and Seuntjens, 2003) for specific accelerator CMs. It includes full accelerator head simulation and a realistic representation of the continuous variation, with no resort to discretization approximations or analytical procedure. It also simplifies the simulation process, improves the dose calculation accuracy and involves a minimal change in computation time. To implement the method, accelerator head models were defined and validated against measurements for a HT treatment unit and two

conventional treatment units. The method's functionality was then tested by comparing simulated and treatment planning dose distributions for four types of treatment techniques: 3D-CRT, step-shoot IMRT, HT, VMAT.

## **2.2 Materials and method**

### **2.2.1 Modifications to BEAMnrc/DOSXYZnrc**

The implementation of a PPS method required several changes to the BEAMnrc and DOSXYZnrc user-codes. These codes were briefly introduced in section 1.4.3.2.1. The current design of the code does not include the ability to associate a time variable to each particle to allow dynamic change of the simulation parameters and geometry as the particle is transported through the various component modules and the patient geometry.

First, we decided to store the time variable in the already existing "zlast" variable, currently used in the BEAMnrc code to record the z-position of the last interaction for visualization purposes. This approach minimized the amount of changes required in the code, allows implicitly the transfer of the time variable to secondary or split particles and also makes it possible to transfer the time variable to other codes such as DOSXYZnrc (i.e. phase space file and shared library modes). To do so, a BEAMnrc file (*subroutine beam\_shower, beamnrc.mortran*) was modified to pick a random "time" number between 0 and 1 at the beginning of each history and to save it as the zlast variable. This number represents the cumulative MU (normalized to the total MU) rather than the exact time measured by a clock at which the particle was emitted during treatment. Second, to allow the simulation geometry to be changed interactively for each history, we used a similar

process as the one used for the DYNMLC (Heath and Seuntjens, 2003) component module (CM). It involves changing each dynamic CM file (*subroutine input\_CMname, CMname\_cm.mortran*) to allow additional information to be read in the simulation input file. For example, instead of providing a static variable for a jaw position, we now need to indicate in the input file the variation of the jaw position as a function of time. We will refer to this as the CPDF since it may loosely be interpreted as a cumulative probability distribution function (CPDF) for sampling purposes. In the simulation input file, a flag number is associated with each CPDF to indicate its type. For example, a table of control points (e.g., [4 cm, 25 %] [5 cm, 50 %] [6 cm, 100 %]) with flag = 1 may be use *without* interpolation to specify the position of a jaw for a 3D-CRT treatment: the jaw is at 4 cm for the first 25 % of the treatment time, at 5 cm for the next 25 % and at 6 cm for the rest of the treatment time. For the same jaw, a similar table ([4 cm, 25 %] [5 cm, 100 %] [6 cm, 100 %] with flag = 2 may be used *with* interpolation to specify the position of a jaw for a VMAT treatment: the jaw moves linearly between 4 cm and 5 cm for the first 25 % of the treatment time and moves between 5 and 6 cm for the rest of the treatment time. There are other types of CPDF (e.g., MLC sinogram) and each is associated with a specific flag number and an appropriate sampling routine. Those sampling routines are all stored as macros inside each CM macro file (*CMname\_macros.mortran*) and they are called for each history in the BEAMnrc file (*subroutine beam\_shower, beamnrc.mortran*) after the time variable is randomly selected. The CM macro files were also modified to declare the dynamic variables as "global" to allow them to be used in the sampling routine.

Last, we modified the DOSXYZnrc code to perform interactively for each particle the coordinate system transformation between accelerator (BEAMnrc) and patient reference frame (DOSXYZnrc) using already existing 3D translation / rotation routines available in the DOSXYZnrc code. The DOSXYZnrc code is already configured to read for each particle the time variable (zlast variable) as part of the phase space file. For the shared library mode, a modification to the shared library sampling routines was required to read the time variable instead of a "dummy z coordinate". The DOSXYZnrc source file (*subroutine srcinput and subroutine srcinit, srcxyznrc.mortran*) for source 8 (phase space) and 10 (shared library) was modified to read the CPDF of dynamic variables (e.g. patient motion, isocenter position, gantry angle, couch angle and collimator angle) in the simulation input file using a similar method as described above for the BEAMnrc component modules. There is again one CPDF per dynamic variable and the sampling is performed independently to allow each CPDF to be defined using a different time grid. Source 8 and 10 are already designed to perform accelerator simulation from multiple directions using a CPDF so the changes required are mostly related to the introduction of flags to allow the use of different types of CPDF and sampling routines. The sampling routines were added in another section of the DOSXYZnrc source file (*subroutine srchst, srcxyznrc.mortran*) before the lines performing the coordinate system transformation.

The PPS method depends on the number of histories providing an adequate sampling of the source space. This is taken care of by ensuring that the statistical uncertainty does not exceed a suitable threshold (e.g., 1%), which may be specified in the simulation. The method is also dependant on several assumptions regarding machine

behavior that are specific to each accelerator type (e.g., linear interpolation of jaw position between TPS discrete positions).

## 2.2.2 User interface

A program was written for Matlab® to automate the beam modeling iterations, automatically process patient information (DICOM files, MLC sinogram files, XML files, ascii files, etc...), write the MC input files, steer the dose calculation on the cluster (~600 nodes) and analyze the results. No modification to the parallel processing was done. Jobs are split the same way as with the unmodified code. In other words, for the BEAMnrc phase space file mode, there is only one phase space file regardless of the number of nodes used and for DOSXYZnrc, there is one dose file per node (DOSXYZnrc combines them at the end of the simulation). The program makes extensive use of the DICOM-RT toolbox (Spezi *et al.*, 2002), the CERR / dcm4che package (Deasy *et al.*, 2003) and the SSH / jcraft-jsch toolbox (Nehbrass *et al.*, 2006). An illustration of this workflow is shown in figure 2.1. The figure 2.2 shows an example of Elekta SynergyS 6V beam modeling result for a 4 cm<sup>2</sup> field size. The result also shows an example of gamma error analysis with a tolerance of 1% and 1 mm. A gamma analysis result inferior to 1 means approximately that a Monte Carlo dose at a given position on a dose profile is within 1% of the corresponding measured dose at the same position or that the dose may be found on the measured dose profile within 1 mm of that position.

The derivation of CPDF for a conventional treatment unit is straightforward since it is a natural extension of the DICOM plan structure based on control points and cumulative MU. As discussed in section 1.3.1, each field, beam segment or arc segment contains two

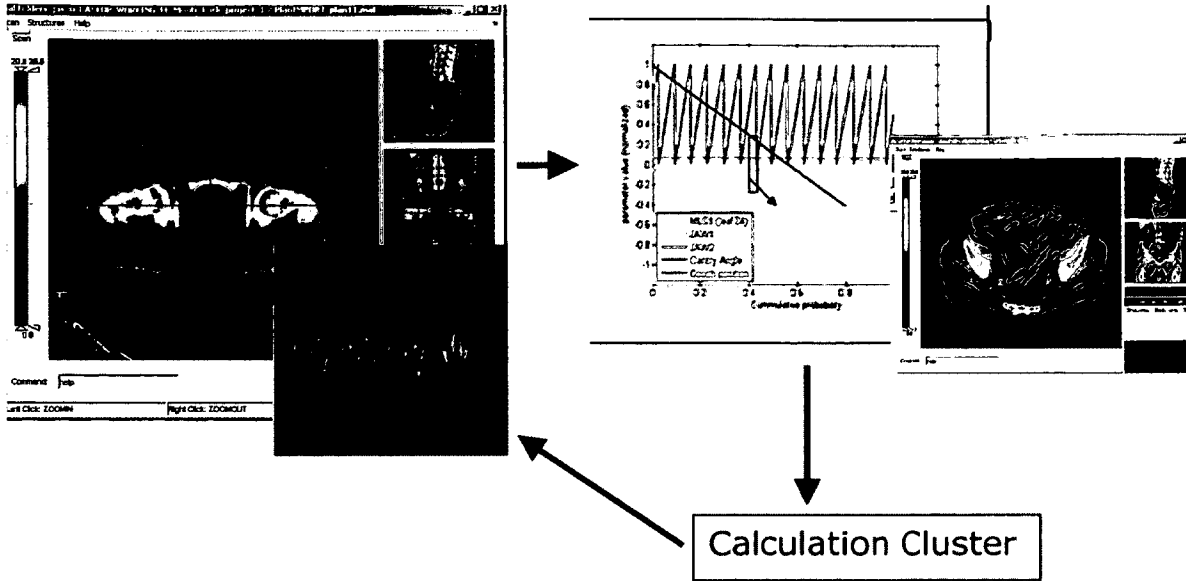


**Figure 2.1** Illustration of the workflow to perform MC dose calculation for a specific patient. First, the patient data (images, plan, contours, dose, MLC sinogram) is extracted, processed and visualized. Second, cumulative probability distribution functions and voxelized geometries are converted as input file. Third, the information is transferred to the calculation cluster and the simulations are steered remotely. Finally, the calculation results are transferred back to the interface for analysis and visualization purposes.

control points defining the initial and the final machine configuration. For 3D-CRT and step-shoot IMRT, the second control point is redundant and was not used to derive the CPDF since the machine configuration is fixed during irradiation. Figure 2.3 shows examples of cumulative probability distribution function extracted for 4 different types of treatment techniques.

The derivation of CPDFs for the HT treatment unit is more complicated. As discussed in section 1.3.2, the HT binary MLC is programmed to enable each of the leaves to be open during a portion of time centered on 51 equally spaced gantry positions called "HT projections". A table or a figure representing the open time of each leaf (number between 0 and 1) as a function of HT projection is typically called an MLC sinogram. At the beginning of the project, the HT TPS (version 3.1) did not include the

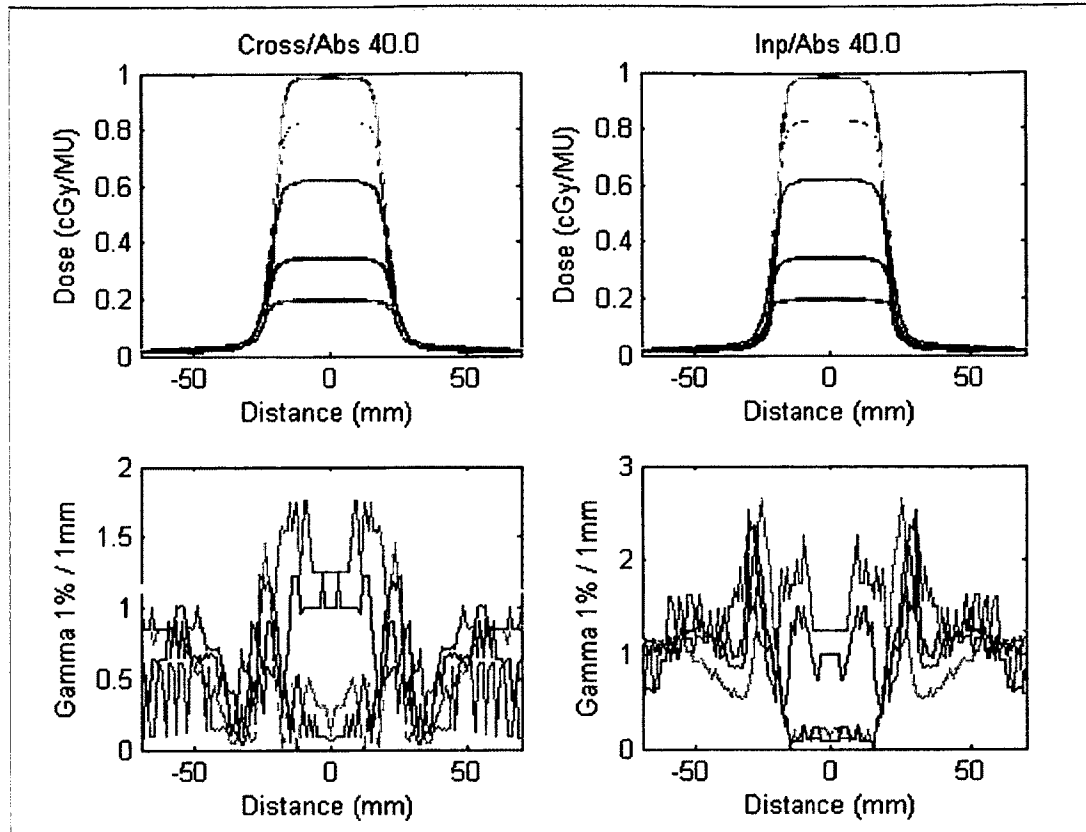


**Figure 2.2** Example of result for the beam modeling component of the interface. Crossplane (left) and inplane (right) measurements of off-axis absolute dose profile (black) are compared against Monte Carlo results (colors) at different depths for a 4 cm field size. An example of gamma error analysis is available at the bottom. The automated beam modeling process attempts to minimize the error function for various field sizes and at different section of the profiles (e.g., penumbra, tail, flat).

MLC sinogram as part of the DICOM plan export file so the CPDF were derived using proprietary XML based patient archive information. Information collected in the XML file included the gantry rotation time, the MU rate, the number of fractions, the number of HT projections, the pitch, the jaw field size, the position of the image isocenter (green lasers) and the starting gantry angle. It also included the MLC sinogram binary file name and the physical distance between the image isocenter position (green lasers) and the treatment isocenter position at the start of the treatment (70 cm – COUCHreadyZ). All those parameters were used to derive the CPDFs using equations similar to those

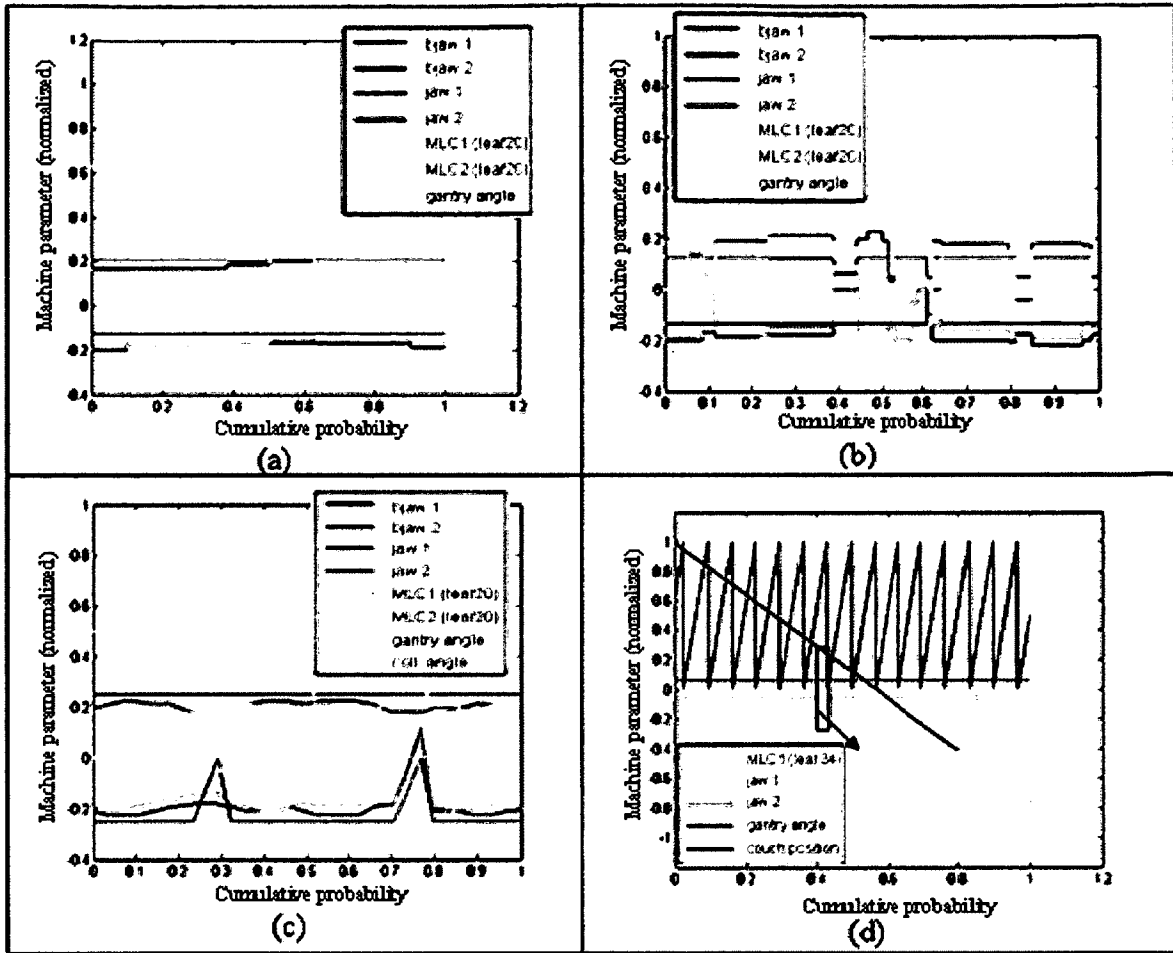


Figure 2.3 Example of cumulative probability distribution functions extracted for 4 different types of treatment techniques: 3D CRT (up-left), step-shoot IMRT (up-right), VMAT (bottom-left), HT (bottom-right).

described by Zhao *et al.* (Zhao *et al.*, 2008). The more recent release of the HT TPS (version 4.0) includes major changes in the XML patient archive and the format of the MLC sinogram. It also includes the MLC sinogram as part of the DICOM plan export file. The MLC position CPDF was derived using two methods. The first method used the MLC sinogram to extract a table of control points including all MLC configuration changes. For example, if a simple treatment with one HT projection used two leaves with respective opening time of 60% and 40%, then 5 control points are needed in the CPDF

(all leaves closed 20%, first leaf open 30%, both leaves opened 70%, first leaf open 80%, all leaves closed 100%). If more leaves are used, the number of control point required per HT projections may be much larger ( $>100$ ). For long treatment times irradiating large volumes, such as total marrow irradiation (TMI), this method may generate a huge amount of control points ( $> 300,000$ ). A more efficient method used for those cases is to directly load the MLC sinogram as a CPDF to reduce by a factor of  $\sim 100$  the amount of data required and to modify the sampling routine to extract the leaf configuration as part of the sampling process. The time variable (number between 0 and 1) may be used to select the appropriate HT projection in the MLC sinogram and to also find the exact time percentage (TP) spent since the beginning of the projection. For example, for a simple treatment with two HT projections, a random time variable of 60 % for a specific history indicates that you are currently at  $TP = 10\%$  of the second tomotherapy projection. Each leaf is then set open if its opening time is larger than the absolute value of  $(2 * TP - 100\%)$ , in other words 80 %. The sampling is faster with the second approach and it is less memory intensive.

Patient motion is typically defined using the standard time (as measured by a clock) instead of cumulative MU as used by our method. A function mapping the standard time to cumulative MU is therefore required to derive appropriate CPDFs for patient motion. Such functions may be generated using accelerator log files in combination with a suitable motion detector and are specific to each treatment since it depends on parameters such as beam off-time, dose rate for each arc segment, etc... Three types of rigid patient motion CPDF were introduced in the code by allowing the translation of transported particles (electrons, positrons, photons) as a function of time.

Translating the particles (the machine) in a direction opposite to the expected patient motion is more convenient in terms of coding and it is equivalent to shifting the actual patient geometry. Modeling properly the respiratory motion and accounting for the anatomy deformation requires further modifications to the EGSnrc user-codes, which is the subject of chapter 3. The first type of patient motion CPDF is a Gaussian function, defined by an amplitude and a width, that may be randomly sampled by each transported particle as they exit the accelerator geometry to simulate random patient motion over a large number of fractions (e.g., for a prostate treatment). The second type of CPDF is a sinusoidal function and it is defined by an exponent, an amplitude, a phase, a period and a duration to model approximately breathing motion. Multiple sinusoidal functions with different parameters may be defined successively and independently in each orthogonal direction to model breathing pattern change over the course of treatment. For cases that can't be modeled appropriately using those functions, a third type of CPDF consists of a table of control points similar to the one used for jaws as explained in section 2.2.1. This type is particularly useful for simulations using data acquired with a motion detector.

### **2.2.3 Monte Carlo model of a conventional treatment unit**

Conventional treatment units were briefly described in section 1.3.1. The MC accelerator head models for two 6 MV conventional treatment units (Elekta Synergy™ and Elekta SynergyS™, Elekta AB., Stockholm, Sweden) were constructed based on technical data provided by the company, previously published work (Van de Walle *et al.*, 2003; De Vlaminck *et al.*, 1999) and caliper measurements done on seven treatment units at TOHCC.

The Elekta Synergy time independent components and their associate BEAMnrc CMs are the target (SLABS), the primary collimator (FLATFILT), the flattening filter (FLATFILT), the ionization chamber (CHAMBER), the backscatter plate (SLABS), the mirror (MIRROR) and the exit window (SLABS). The time dependant components consist of the electron beam, the MLC (MLCE), the back-up jaws (MLCQ) and the lower jaws (JAWS). Those components were among those modified to make it possible to change the parameters interactively for each history. Figure 2.4 shows an illustration of the BEAMnrc model of the Elekta Synergy accelerator.

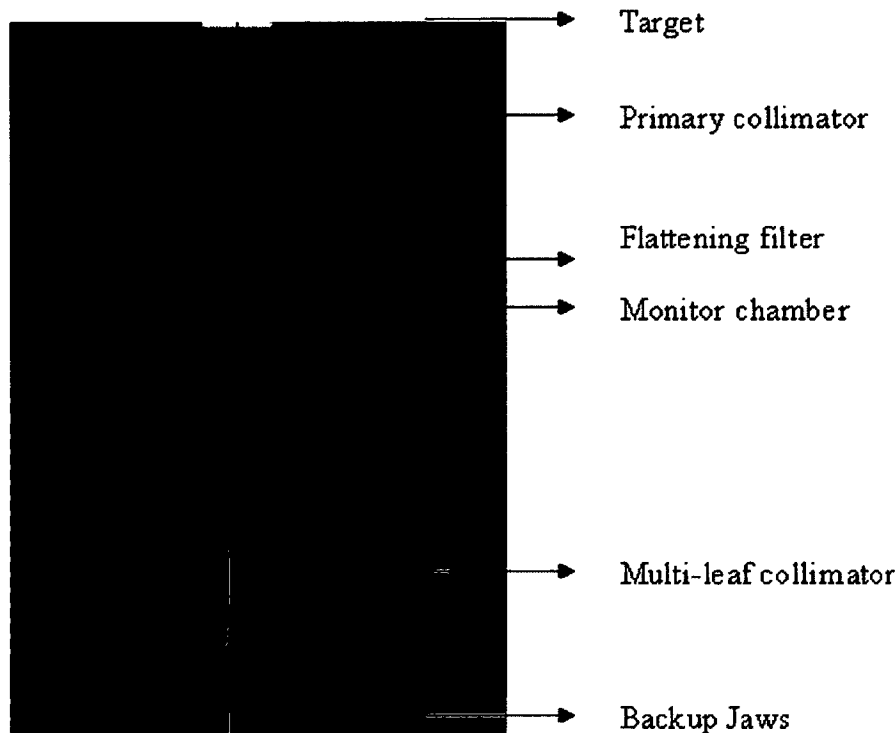


**Figure 2.4** Crossplane view of the Elekta Synergy accelerator BEAMnrc model (jaws not shown).

The Elekta SynergyS time independent components and their associate BEAMnrc CMs are the target (SLABS), the primary collimator (FLATFILT), the flattening filter

(FLATFILT), the ionization chamber (CHAMBER), the backscatter plate (SLABS), the mirror (MIRROR), the fixed primary jaws (PYRAMIDS), the fixed backup jaws (PYRAMIDS) and the exit window (SLABS). The time dependant components consist of the electron beam and the MLC (MLCEsyms). To model the Elekta SynergyS MLC geometry, we introduced changes in the MLCE BEAMnrc CM to account properly for the rotation and the translation of the leaves which differ from the Elekta Synergy treatment unit. The Elekta SynergyS MLC is referred to commercially as the Beam Modulator and does not include a tongue and groove mechanism to limit the amount of radiation transmitted between leaves. The MLC is instead rotated around a crossplane axis to slightly defocus the leaf side with respect to the beam focal spot. The BEAMnrc MLCE CM allows such rotation. However, the rotation also implies a translation of the MLC leaves in the inplane direction with respect to the beam central axis. To align the field opening with the central axis, the MLC bank is usually translated to compensate for the rotation. Modifications were introduced in the CM to perform this translation. A more recent version of the Elekta Synergy treatment unit is designed using an MLC (commercially referred to as MLCi2) which is also based on the same principle as the Beam Modulator (no tongue and groove).

For both models, the electron source routine in BEAMnrc was modified to use a Gaussian elliptical shape to account for differences between crossplane and inplane penumbra not attributable to the MLC or jaw properties ( $\sim 1$  mm). All simulations were performed with photon cutoff energy  $PCUT = 0.01$  MeV and electron cutoff energy  $ECUT = 0.7$  MeV (includes rest mass energy) in BEAMnrc.  $ECUT = 0.660$  MeV was used in DOSXYZnrc. The MC calculation was calibrated at 5 cm depth,  $SAD = 100$  cm

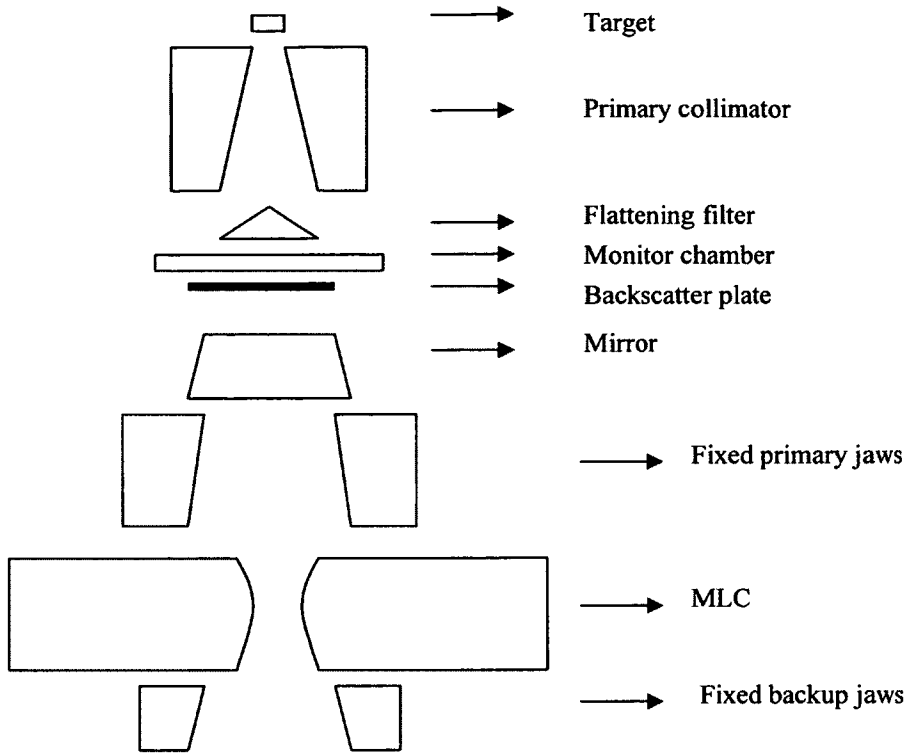


**Figure 2.5 Crossplane illustration of the Elekta SynergyS accelerator BEAMnrc model.**

and  $10 \times 10 \text{ cm}^2$ . In other words, dose (Gy) is obtained from the treatment plan MC calculation results (Gy / incident electron) by multiplying it with the treatment plan MU and the ratio of accelerator output (Gy / MU) and MC simulation results (Gy / incident electron) under calibration conditions. Several variance reduction techniques were used including BEAMnrc directional bremsstrahlung splitting (splitting number = 1000) (Kawrakow *et al.*, 2004) and DOSXYZnrc splitting (splitting number = 40). The patient CT datasets were converted to DOSXYZnrc phantom files using clinical calibration files (HU to density, HU to material). When needed, MC dose was converted from dose-to-medium to dose-to-water using stopping power ratios (Siebers *et al.*, 2000) to provide meaningful comparison with the TPS.

#### 2.2.4 Monte Carlo model of a HT treatment unit

The MC accelerator head model for HT treatment unit (Hi-Art<sup>®</sup>, Tomotherapy Inc., Madison, WI) was constructed based on previously published work (Zhao *et al.*, 2008; Sterpin *et al.*, 2008) and extensive caliper measurements done on two treatment units at TOHCC as proprietary data were not available for all parameters. The time independent components and their associate BEAMnrc CMs are the target (SLABS, FLATFILT), the hardening plate and the primary collimator (PYRAMIDS), the ionization chamber (CHAMBER) and the end block below the MLC (PYRAMIDS). The time dependant components consist of the electron beam, the jaws (PYRAMIDS) and the MLC (MLCEtomo). Those components were also modified as explained earlier to make it possible to change the parameters interactively for each history. The jaws are currently fixed during clinical delivery but we included the possibility of dynamic motion in the model since this option is expected to be released in the future and also to make it possible to simulate simultaneously multiple fractions with different jaw settings, or to simulate junction deliveries (retreat, total marrow irradiation). The MC calculation was calibrated at 1.5 cm depth, SAD = 85 cm and a field size of 5x40 cm<sup>2</sup>.

To model the HT MLC geometry, we introduced changes in the MLCE BEAMnrc CM to account properly for the arc shape of the MLC bank which differs from a conventional treatment unit. In the modified MLCE CM, the nominal leaf width (i.e., 6.25 mm) is defined on an arc instead of the isocenter plane as shown in figure 2.6. An inplane view of the MLC geometry model is shown in figure 2.7. To further improve the

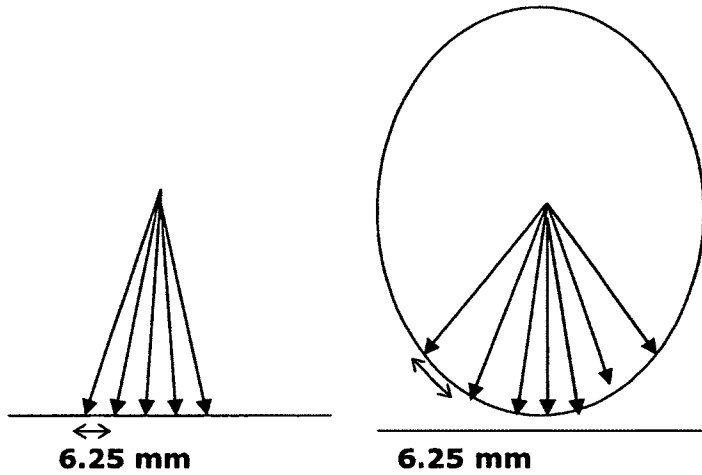


**Figure 2.6** The MLCE component model was modified to define the leaf width on an arc (right) instead of the isocenter plane (left).

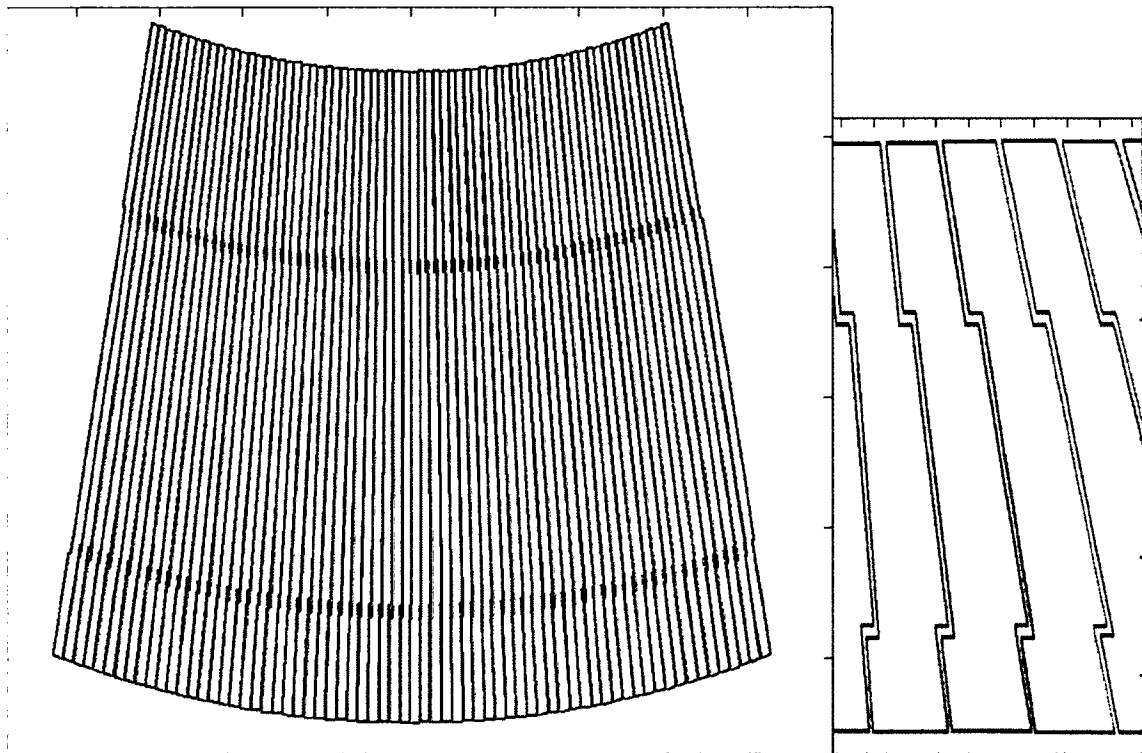


**Figure 2.7** Inplane view of the tomotherapy binary multi-leaf collimator geometry (left). A closer view (not to scale) of the interleaf air gap and of the tongue and groove is also shown (right).

model of the HT MLC geometry, we introduced changes in the CM to account properly for the defocusing of the MLC geometry which means that leaf sides are focused at a point slightly higher than the beam focal spot. This is deliberately done by the manufacturer to lower the amount of transmission radiation through closed leaves without having to increase the size of the tongue and groove or lower the interleaf air gap (Balog *et al.*, 1999). Sterpin *et al.* (Sterpin *et al.*, 2008) used technical drawing from the company to do MC simulation using Penelope code and pointed out the need to also introduce a 2 mm shift in the target position to properly fit the field edge.

Defocusing the leaf sides has the drawback of increasing the amount of primary source shielding for small leaf opening (Balog *et al.*, 2003), particularly for off-centered leaves as shown in figure 2.8. This effect is very sensitive to the alignment of the beam focal spot with the MLC geometry. Figure 2.9 shows for example the photon fluence reduction due to primary source shielding when a single leaf is opened (the effect is negligible if more than 3 leaves are opened). These data were extracted using the on-board detector panel for one of our HT treatment unit on different dates. The difference in reduction between the two dates may be up to 4%, which explains why these data are routinely acquired and updated in the TPS. The data shown in figure 2.9 is also occasionally asymmetric, which is explained partially by the alignment of the beam focal spot and the MLC geometry. It is also partially explained by the fact that the tongues and the grooves are always pointing in the same direction, which makes the MLC geometry asymmetric. To properly tweak the MLC geometry for the MC model, an analytical code was written to calculate fluence reduction for the leaves. The code is a simple ray tracing technique with a Gaussian focal spot. An example of the result is shown in figure 2.10.

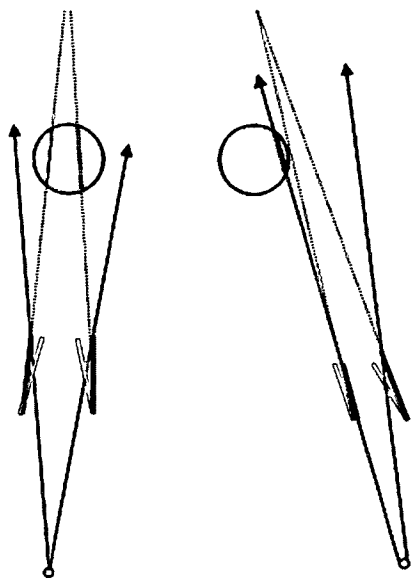


**Figure 2.8** Illustration of the impact of primary source shielding. The beam focal spot is shown in red and represents the electron beam impinging on the target. Focused leaf sides are also shown in red and defocused leaf sides are shown in black. The defocused leaf sides are defined as "defocused" because they are focused on a point located above the beam focal spot. The amount of primary source visible (green arrows) in the isocenter plane through off-centered leaf opening is smaller when the leaf sides are defocused.

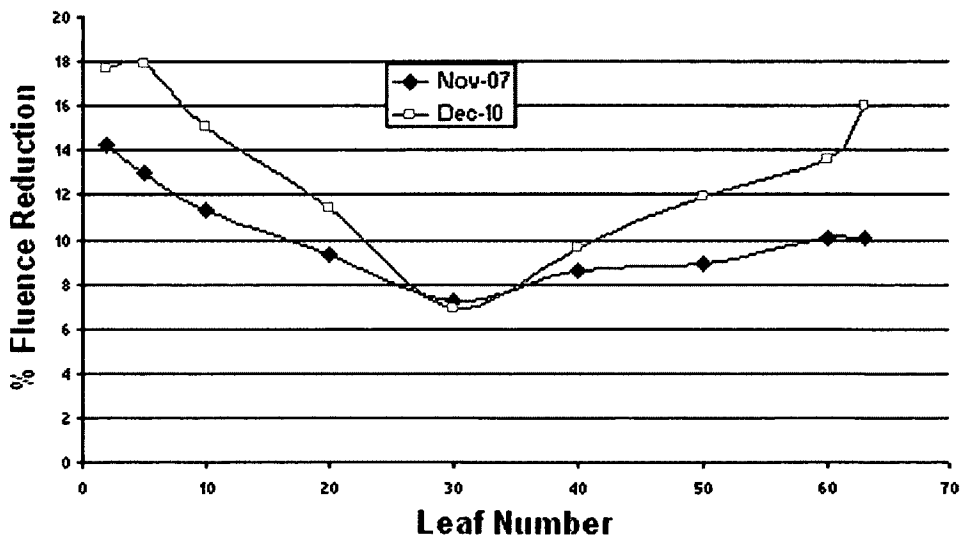


**Figure 2.9** Example of photon fluence reduction due to primary source shielding when a single leaf is opened. Leaf number 32 and 33 are the central leaves.

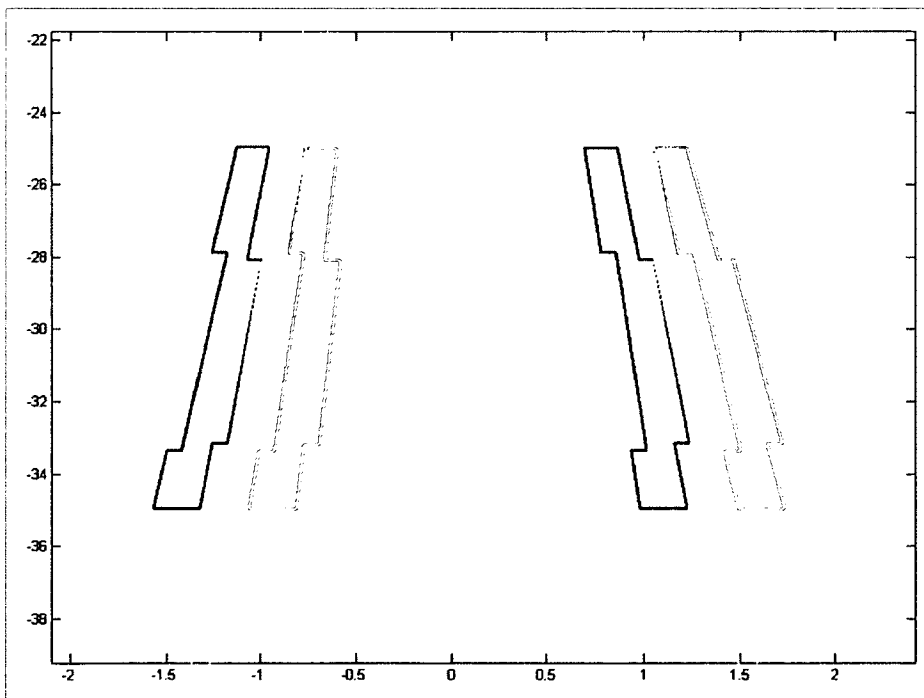
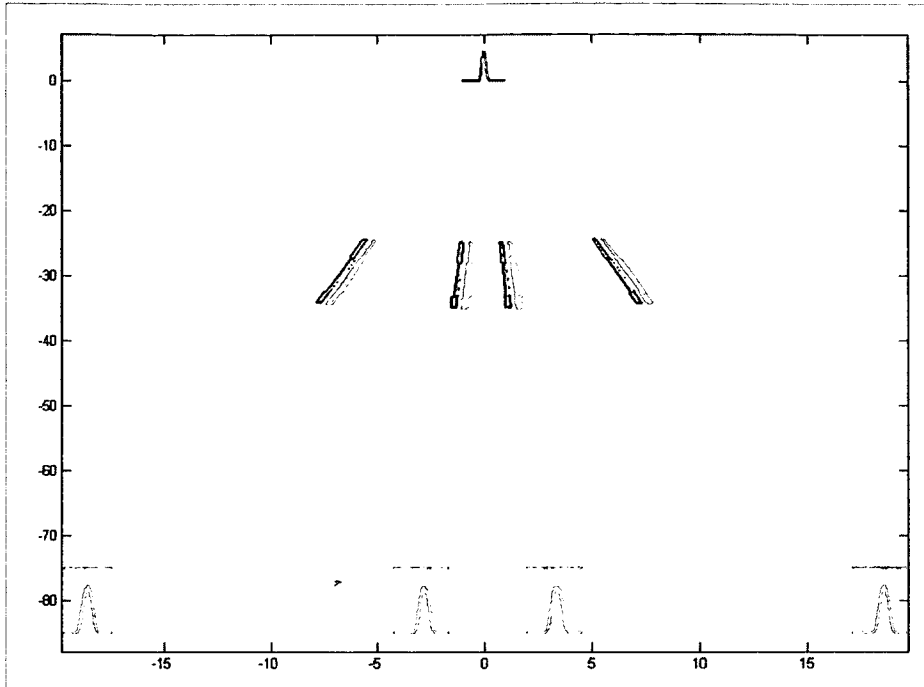


**Figure 2.10** Example of fluence reduction results (top) based on an analytical code that calculates the amount of photon fluence produced by a finite source that is reaching points in the isocenter plane. In this case, the leaf sides were focused on the beam focal spot so the fluence reduction is similar for centered and off-centered leaves. A closer view of the center leaves is also shown (bottom). The two inner photon traces in yellow (closer to the isocenter position 0) are shown to hit different part of the asymmetric MLC geometry, which explains partially the asymmetry of the fluence reduction from one side of the leaf bank to the other. The dimensions are in cm.

Residual fluence reductions that are not accounted for by the MC MLC model (~1%) may be included by changing the corresponding MLC sinogram values. Leaf latency is also included in the model by changing sinogram values as performed in the TPS (Balog *et al.*, 2003).

### **2.2.5 Measurements for validating the Monte Carlo models**

Measurements were performed for static beam delivery on both treatment unit types to tune and validate the MC models. Detector correction factors discussed in section 1.4.2.1 were not used to modify the measurements. Those correction factors were minimized by choosing detectors with small perturbation on the measured dose distributions and combining results from multiple detector type when needed. Measurements on the conventional treatment unit were done using a 60x60x60 cm<sup>3</sup> water tank (RFA-300, Iba Dosimetry, Uppsala, Sweden), an RK 0.12 cm<sup>3</sup> ionization chamber and a PFD 2.5 mm diameter photon diode. Measurements were performed with an SSD of 100 cm and RDFs were measured at 5 cm depth using the ion chamber, except for field sizes smaller than 4 cm where the diode was used. PDD profiles were measured with the ion chamber except for the buildup region and for field sizes smaller than 5 cm where the diode was used. OAR profiles were measured at various depths using the diode except for the profile tails of fields larger than 20 cm which were measured using the ion chamber. Similar measurements on the HT treatment unit were done using a 30x30x60 cm<sup>2</sup> water tank (TomoScanner<sup>TM</sup>, Standard Imaging Inc., Middleton, WI), an A1SL 0.056 cm<sup>3</sup> ionization chamber and a 0.6 mm diameter stereotactic field photon diode. Measurement setup was

SSD 85 cm and RDFs were measured at 1.5 cm depth. Kodak EDR-2 films were used in a SolidWater® based phantom for dynamic beam delivery measurements or when improved spatial resolution was required for static beam delivery measurements. The different types of static beam measurements were merged to generate absolute crossplane and inplane dose profiles to perform the comparison.

### **2.2.6 Treatment planning systems**

Treatment plans were generated for 4 types of treatment techniques using three different TPSs currently in clinical use at TOHCC. Standard prostate and brain cases were respectively chosen for the conventional and the HT treatment units. The selected plans are relatively simple so differences between simulated and planned dose distributions should be small except in known areas that were documented as part of the TPS beam modeling process.

For the conventional treatment unit, a 6-field 3D-CRT prostate plan was generated using a fast multigrid point kernel C/S dose calculation algorithm TPS (XiO 5.4, Elekta CMS Inc., Maryland Heights, MO). A similar case was also planned using aperture-based inverse optimization for step-shoot IMRT (Monaco 1.0.2, Elekta CMS Software Inc., Maryland Heights, MO) and VMAT (Monaco VMAT beta, Elekta CMS Software Inc., Maryland Heights, MO). A second VMAT case was also planned for a SABR lung treatment. The Monaco TPS is based on a full PPS MC dose calculation algorithm (i.e., accounts for continuous motion) and makes use of a virtual source model and the XVMC calculation package. Three HT plans were generated using inverse optimization and a 2.5 cm jaw field (Hi-Art 3.1, Tomotherapy Inc., Madison, WI). The first plan is a simple

brain case with a modulation factor of 3.1. The modulation factor is defined as the maximum leaf open time divided by the mean open time of all active leaves. The second plan is a more "extreme" case to illustrate the effect of gantry angle discretization: a fast treatment (modulation factor of 1.1) of a 3 cm diameter cylindrical target in a solid water phantom located at about 15 cm from the isocenter. The third plan is a TMI plan to test the functionality of the method for longer treatment time. The TPS is based on a point kernel C/S dose calculation algorithm that approximates the continuous gantry motion by 51 static projections per rotation. Conversion of MC dose from dose-to-medium to dose-to-water was performed for the 3D-CRT plan and the HT plan since they were calculated using density scaled dose kernels generated in water.

## **2.3 Results**

### **2.3.1 Modifications to BEAMnrc/DOSXYZnrc**

Modifications to the codes were first tested by comparing simple MC calculations against summed discretized dose distributions (SCS approach) generated using the unmodified BEAMnrc/DOSXYZnrc. In principle, it is possible to perform as many SCS discrete simulations as there are histories and the differences between PPS and SCS methods is then a matter of sampling (random vs. iterative) and both converge approximately to the same solution. In practice however, particularly in our implemented SCS method for comparison purposes, MC calculations are not performed that way and the simulation process typically involves choosing an appropriate discretization interval that makes the error clinically negligible for most clinical cases (i.e.  $\sim 7$  degrees gantry angle for helical

tomotherapy TPS). Observed differences between PPS and SCS methods were below dose calculation uncertainties as expected and recorded time indicated that the sampling routines increased the simulation time by less than 2 % for a case involving 20,000 control points. The recorded time did not include the time required for steering and summing individual beam simulations. The average time for the PPS MC simulations for all the clinical cases was about 3 hours using 32 nodes for a statistical uncertainty lower than 1%. Modifications to the code were also tested by visually inspecting the phase space file and the dose distribution to confirm that sampling routines are used correctly. For example, Figure 2.11 shows the effect of simulating the full continuous gantry motion for one HT TPS projection (~7 degrees) with 3 non-adjacent leaves fully opened. This case is not clinically relevant but it illustrates the correct functionality of the model and it may also be calculated analytically without resorting to the TPS or MC methods. The phantom dimension is 40 cm along the beam direction and 60 cm along the direction perpendicular to the leaf motion. The isocenter is located in the middle of the phantom at 20 cm depth. The open leaves are all located on the right side of the MLC bank. Figure 2.11a shows a transverse MC dose distribution calculated with a static gantry angle of 0 degrees (similar to TPS). Figure 2.11b shows a transverse MC dose distributions calculated with a continuous gantry angle variation (-3.53 to 3.53 degrees). The effect of gantry motion is larger away from the isocenter as demonstrated by Figure 2.11c, which shows a comparison between dose profiles extracted at 17 cm from the isocenter in the direction perpendicular to the leaf motion.

### 2.3.2 Validation of the MC model of a conventional treatment unit

The electron beam source code was tuned to fit dose measurements using a Gaussian elliptical shape with a full width at half maximum (FWHM) of 0.8 mm (inplane) x 2 mm (crossplane), an electron beam mean energy of 6.5 MeV, a Gaussian mean angular spread

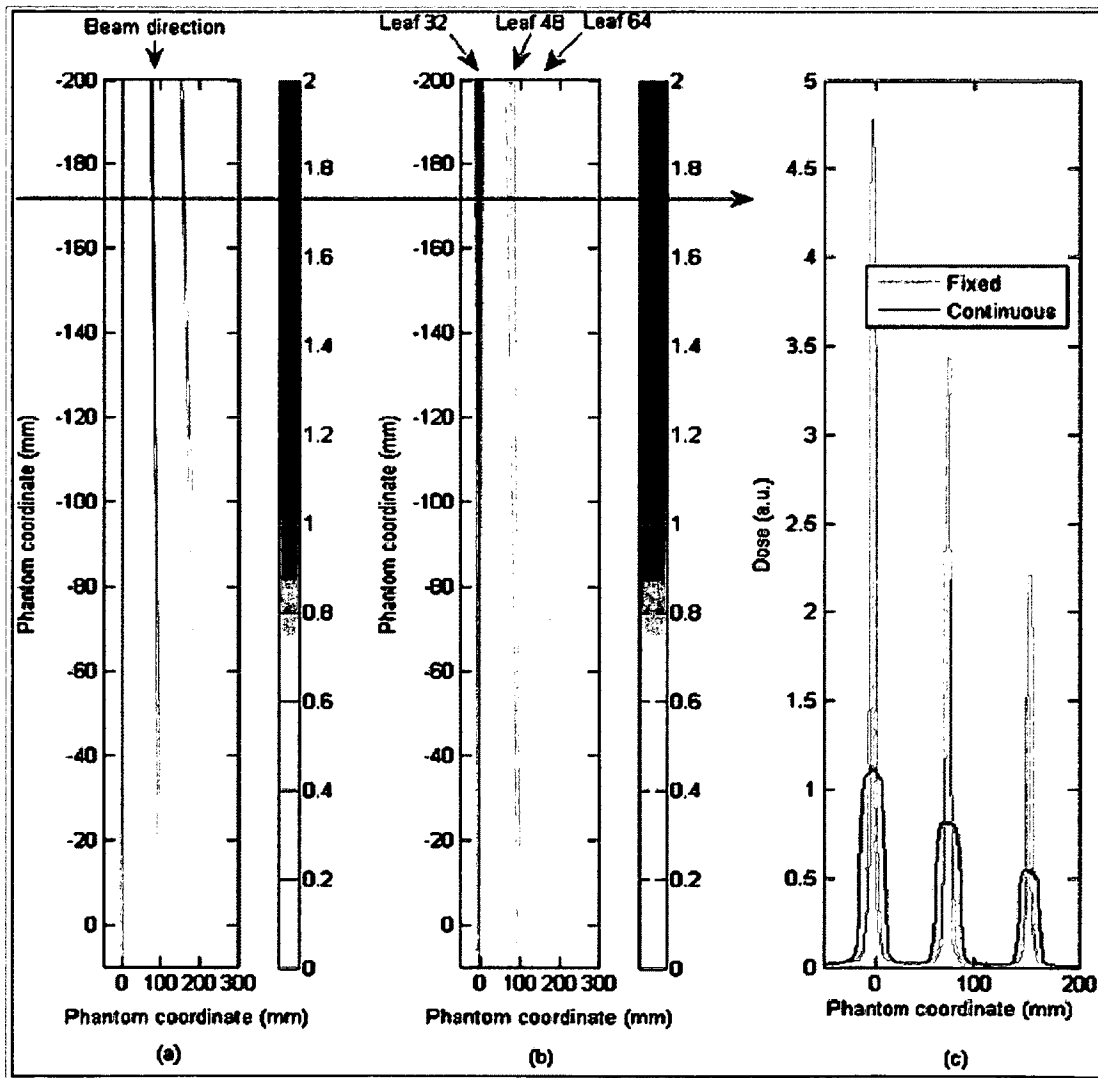
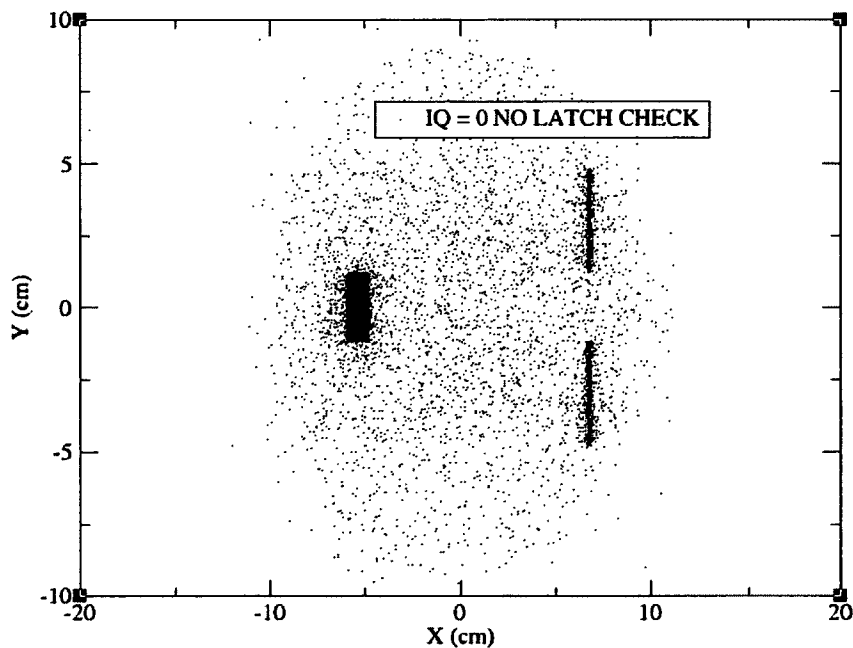


Figure 2.11 MC-calculated transverse dose distribution for a single tomotherapy projection (~7 degrees) with 3 non-adjacent leaves fully opened for (a) static gantry angle (0 degrees) and (b) continuous gantry angle variation (-3.53 to 3.53 degrees). A comparison between dose profiles extracted at 17 cm from the isocenter (shown by arrow) in the direction perpendicular to both the leaf movement and the beam direction is shown in (c). The phantom coordinate axis perpendicular to the arrow (up to down in the figure) is parallel to the beam direction. (Source: Paper I reproduced with permission)

of 1.0 degrees and a Gaussian energy spectrum with a FWHM of 0.6 MeV truncated to  $\pm$  0.5 MeV.

The back-up jaws and MLC have round leaf ends and required calibration to account for the non-linear relationship between the physical position and the location of the radiation field edge. A 3<sup>rd</sup> degree polynomial based on comparison between measured and simulated off-axis profiles of photon fluence was used to convert the required radiation field size defined on the isocentre plane to a physical position of the leaf in the accelerator head. The photon fluence profile is extracted from phase space file such as the one shown in figure 2.12. In this example, the phase space file shows a leaf opening of 2



**Figure 2.12** Example of scatter plot for a phase space file extracted at 60 cm from the target. The phase space file is used to calibrate the leaf position by extracting photon fluence profile along the leaf movement direction. The figure shows a leaf opening of 2 cm located off-center (left). Only a few leaves are actually opened and the remaining leaves are closed (right) with a gap to avoid collisions. The X axis is parallel to the leaf movement direction and the Y axis is perpendicular to the leaf movement direction. Both X and Y axes are perpendicular to the beam direction.

cm located off-center. Only a few leaves are actually opened and the remaining leaves are closed (with a gap to avoid collisions) on the opposite side of the field. Similar phase space files with the opening centered at different positions along the crossplane line were used to extract the field edge by locating the position of 50% and 55% photon fluence reduction (compared with the middle of the leaf opening) for leaves and back up jaws respectively. Figure 2.13 shows an example of a result for the Elekta SynergyS MLC. In this case, the difference between the field edge and the projected leaf tip position is shown as a function of off-axis position. The parabolic shape of the curve is caused by the off-axis variation of the leaf tip transmission and a gradual change in the location of the photon / leaf intersection along the leaf curvature as explained by (Boyer and Li, 1997).

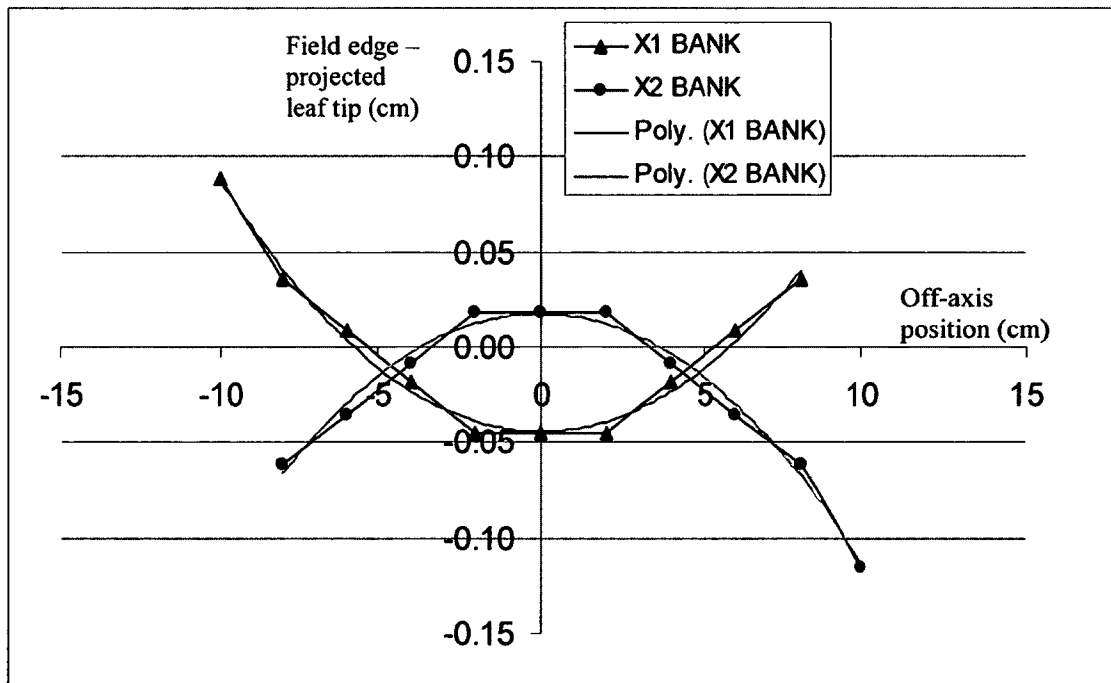


**Figure 2.13 Example of leaf calibration result for the Elekta SynergyS MLC. The difference between the field edge and the projected leaf tip position is shown as a function of off-axis position for the two MLC banks along with a polynomial fit. The parabolic shape of the curve is caused by the off-axis variation of the leaf tip transmission and a gradual change in the location of the photon / leaf intersection along the leaf curvature**

Relative dose agreement is within 1 % for PDD and 0.5 % for RDF including field sizes as small as 1 cm<sup>2</sup>. Absolute dose agreement for static fields between MC and measurements is within 2 % / 1mm as shown on Figure 2.14a for the Elekta Synergy. An agreement of 2% / 1 mm is considered acceptable because it is comparable with the overall absolute dose measurement uncertainty. The observed agreement is better or similar to that obtained with Monaco and XiO TPS as shown in Figure 2.14b and 2.14c,

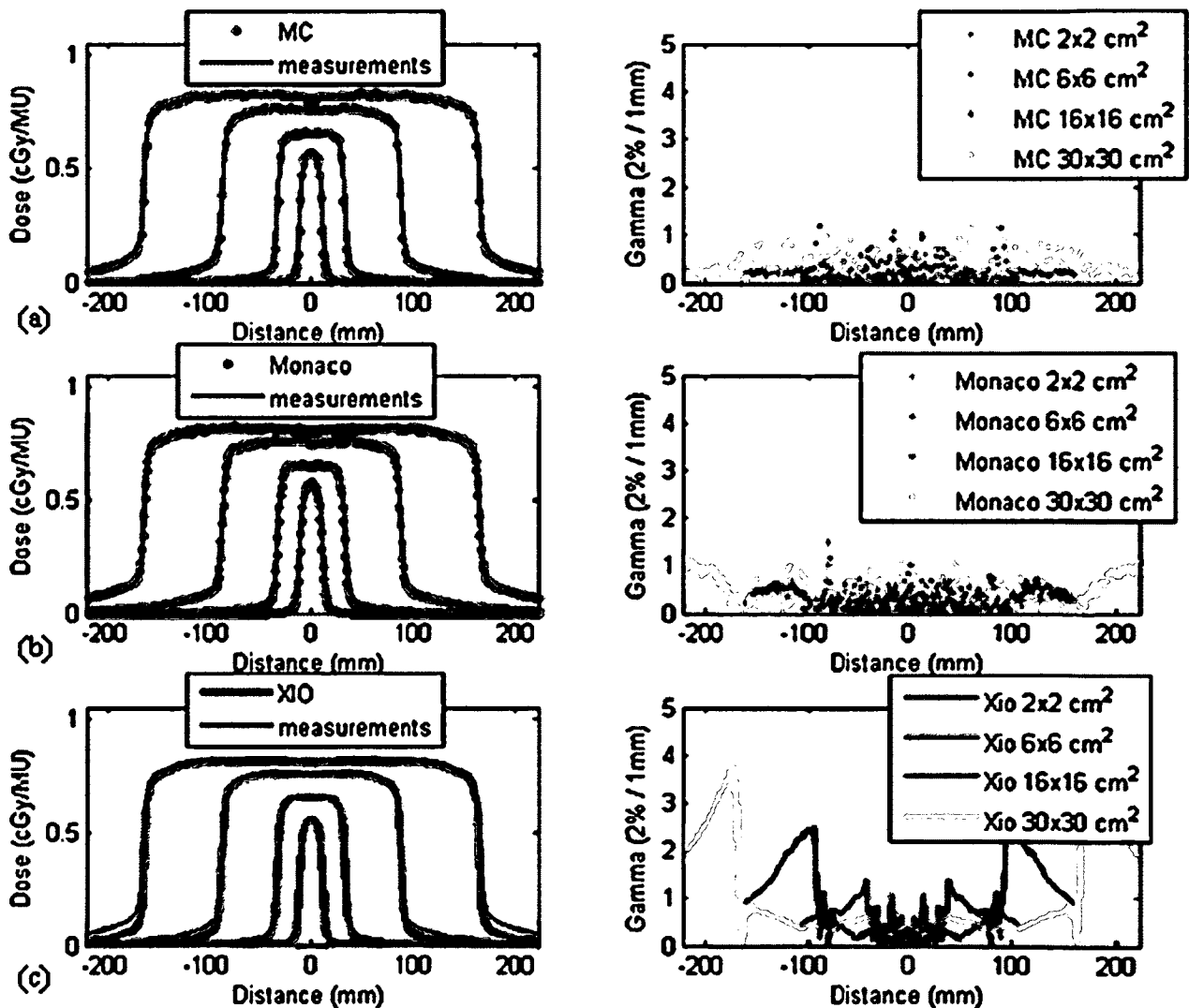
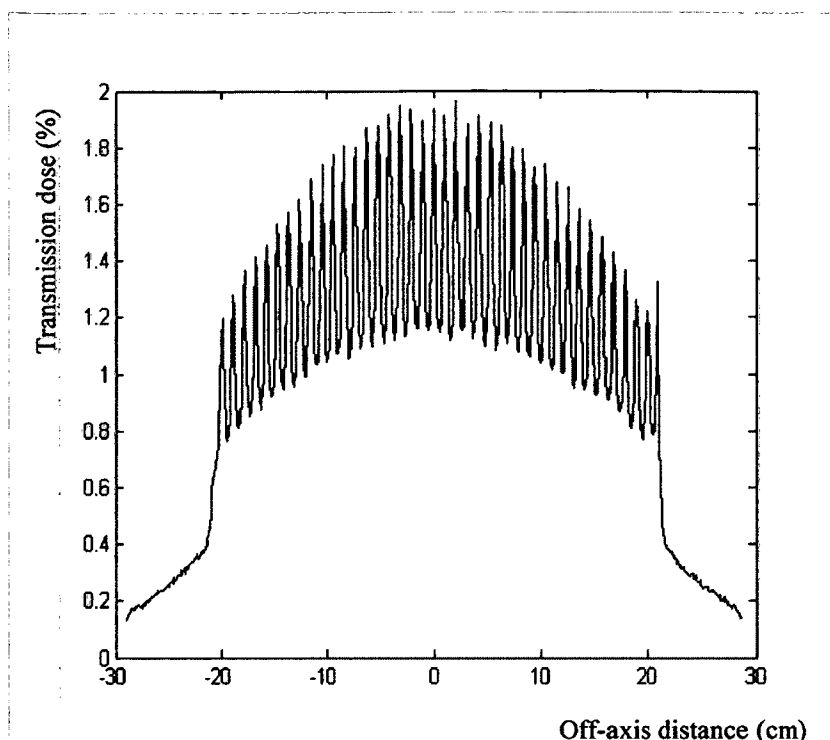


Figure 2.14 (a) MC- simulated and measured absolute dose profiles (crossplane) at 10 cm depth for four different field sizes (left). Gamma analysis for the same profiles is shown on the right. The same measurements are also compared with the Monaco TPS (b) and the XiO TPS (c). (source: Paper I reproduced with permission)

respectively. Observed differences between the XiO TPS and measurements in the tail region are more significant for larger field sizes (~5 % of central axis dose) and are typical of issues related to extra focal radiation modeling. Observed differences between the Monaco TPS and measurements in the tail region of large field sizes (~2 % of central axis dose) are also related to extra focal radiation and primarily caused by use of a secondary source weight that is too large. The Monaco TPS dose calculation algorithm includes the head scatter contribution as part of its virtual source model. The size and weight of the secondary source are used to tune both output factors and the tail region, which explains the observed compromise.

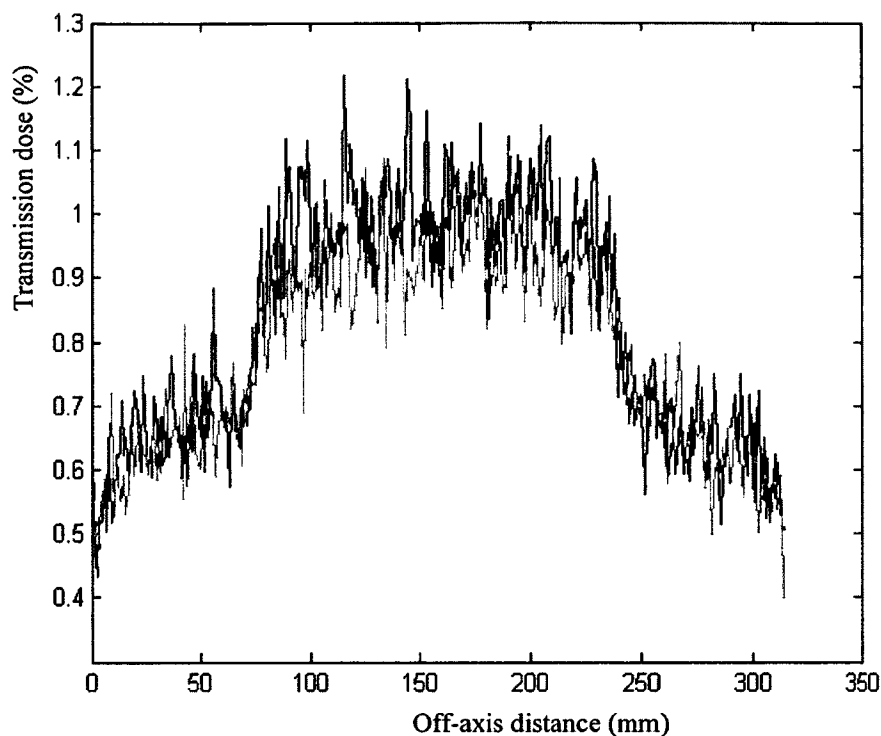
The MLC parameters (tongue and groove, interleaf air gap, width) were fine tuned by simulating the transmission dose through and between the leaves. Figure 2.15 shows an example of transmitted dose (relative to a 10x10 open field) at 5 cm depth for the Elekta Synergy. The observed transmitted dose is in agreement with measurement (film normalized by ion chamber) and values reported in the literature (Van de Walle *et al.*, 2003) (mean 1.5%, minimum 0.8%, maximum 2.0 %). A similar result is shown in figure 2.16 for the Elekta SynergyS and the agreement with measurements (mean 0.9%, minimum 0.8%, maximum 1.1 %) is also acceptable.

The MLC parameters were also fine tuned by simulating the tongue and groove effect. This effect was defined by Webb *et al.* (Webb *et al.*, 1997): when a field is comprised of matched components in which either the tongue or the groove projects into the open part of the field, the resulting junctioned field may have an underdose in the region of interlock. The underdose is caused by the fact that exponential attenuation is



**Figure 2.15** Monte Carlo simulation of transmission dose percentage at 5 cm depth for the Elekta Synergy accelerator (normalized to the 10x10 cm<sup>2</sup> open field dose). The leaves are completely closed and the off-axis distance is perpendicular to the leaf movement direction and relative to the central axis.

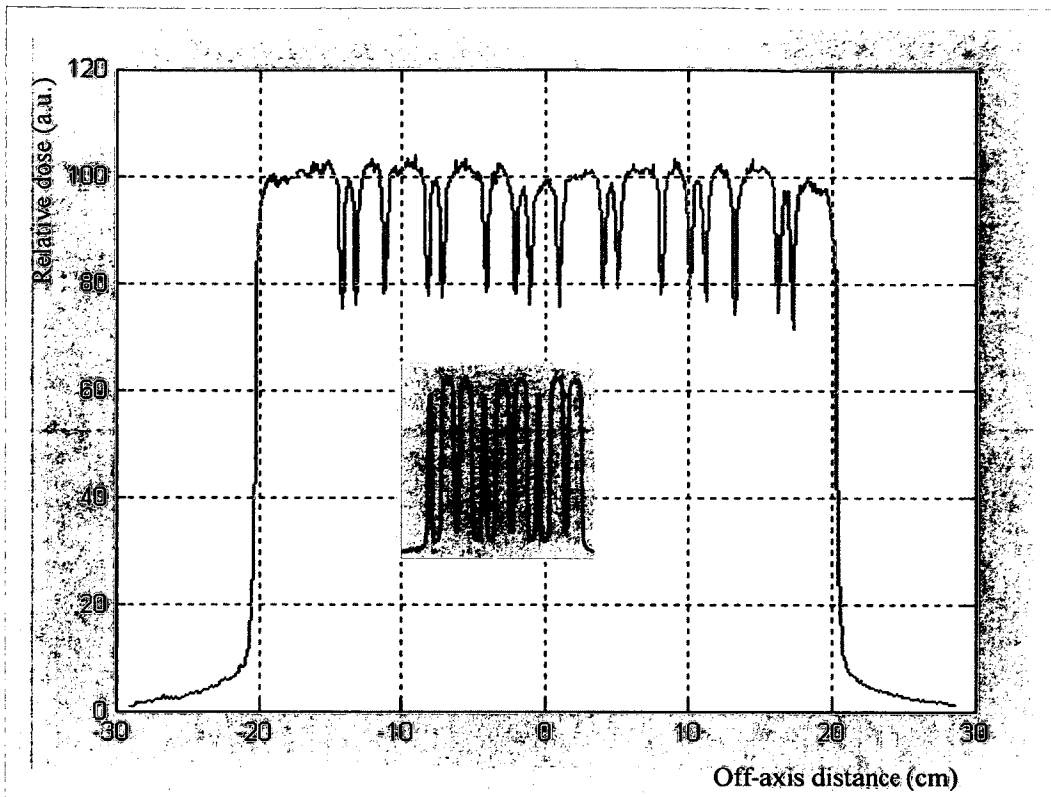
not additive: the photon exponential attenuation caused by a thickness  $d$  is smaller than the combination of two exponential attenuations of thickness  $d/2$ . Figure 2.17 shows an example of tongue and groove effect simulated using MC for the Elekta Synergy treatment unit. The dose calculated for a given set of open leaves and the dose calculated with the opposite field (leaves that were closed are opened and vice versa) are combined and plotted. The junction between opposing fields is clearly visible as an underdose of about 20% to 30%, which is in agreement with film measurement and values reported in the literature (Van de Walle *et al.*, 2003) (22% to 44%). A similar result is shown figure 2.18 for the Elekta SynergyS. The underdosage is in average 20.0% and 14.2% for MLC rotations of 5 degrees and 3 degrees respectively. The agreement with the film



**Figure 2.16** Monte Carlo simulation of transmission dose at 5 cm depth for the Elekta SynergyS accelerator (normalized to the 10.4x10.4 cm<sup>2</sup> open field dose). The blue line is for an MLC rotation of 3 degree and the red line is for an MLC rotation of 5 degrees. As explained in section 2.2.3, the MLC is rotated around a crossplane axis to slightly defocus the leaf side with respect to the beam focal spot. The leaves are completely closed and the off-axis distance is perpendicular to the leaf movement direction and relative to the starting position of the phantom located at 160 mm from the central axis. The leaves are starting and ending at distances of 70 cm and 230 cm respectively.

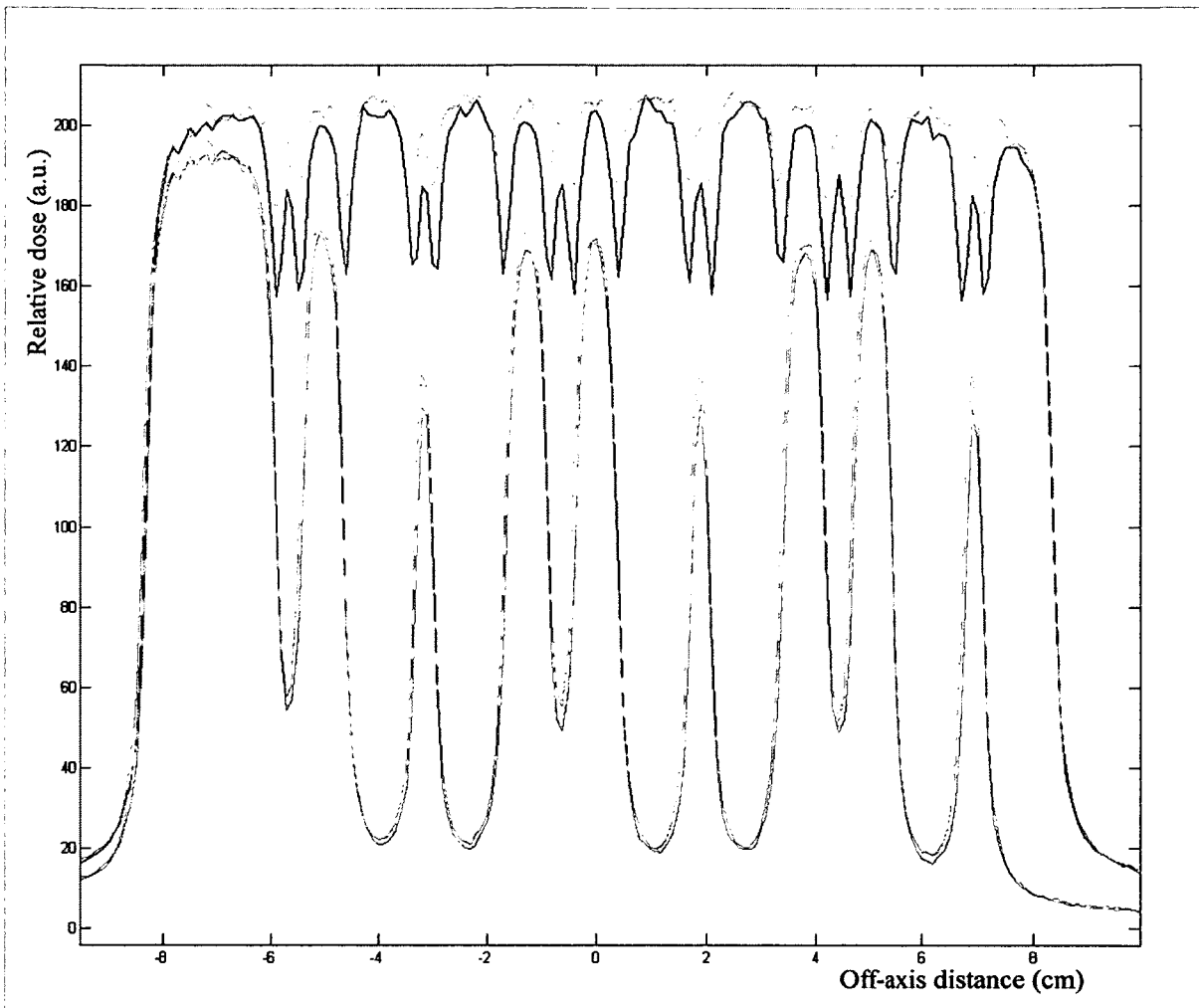
measurements ( $19.4\% \pm 4.1\%$ ) is superior for the MLC rotation of 5 degrees but both results are acceptable from a clinical point of view since the impact of the tongue and groove effect on the overall patient dose is usually minimized using various treatment planning strategies.

The name "tongue and groove effect" for the Elekta SynergyS accelerator is not appropriate since there is no tongue or groove in the leaf geometry. However, the underdosage effect is caused by the same principle as the tongue and groove effect except that the partial infiltration of leaf material in the field opening is due to the defocused leaf



**Figure 2.17** Monte Carlo simulation of tongue and groove dose for the Elekta Synergy treatment unit. The tongue & groove dose is obtained by summing the dose calculated for a given set of open leaves and the dose calculated with the opposite field (leaves that were closed are opened and vice versa). The insert shows the dose calculated for one set of open leaves.

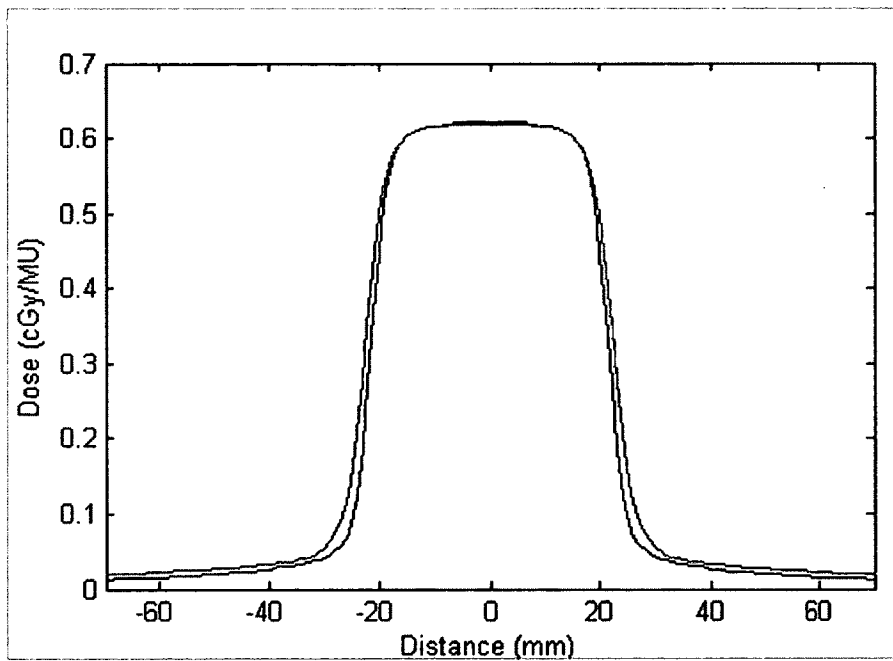
side instead of the tongue. An additional impact of tongue and groove or leaf defocusing is a reduction of the effective field size. For the Elekta Synergy accelerator, the effect is about 2 mm and is usually dealt with by first opening the superior and the inferior leaves defining the field and then collimating the opening with the jaws instead. For the Elekta SynergyS, the field size reduction is smaller (~0.8-1.4 mm) and is typically ignored in most treatment planning systems. For example, figure 2.19 shows an inplane off-axis dose profile at 10 cm depth, SSD 100 cm for a field size of 4 cm defined on the isocenter plane. The measured field size is 1.4 mm smaller than the TPS field size based on a nominal value of 4 cm (10 leaves are opened, each with a nominal width of 4 mm).



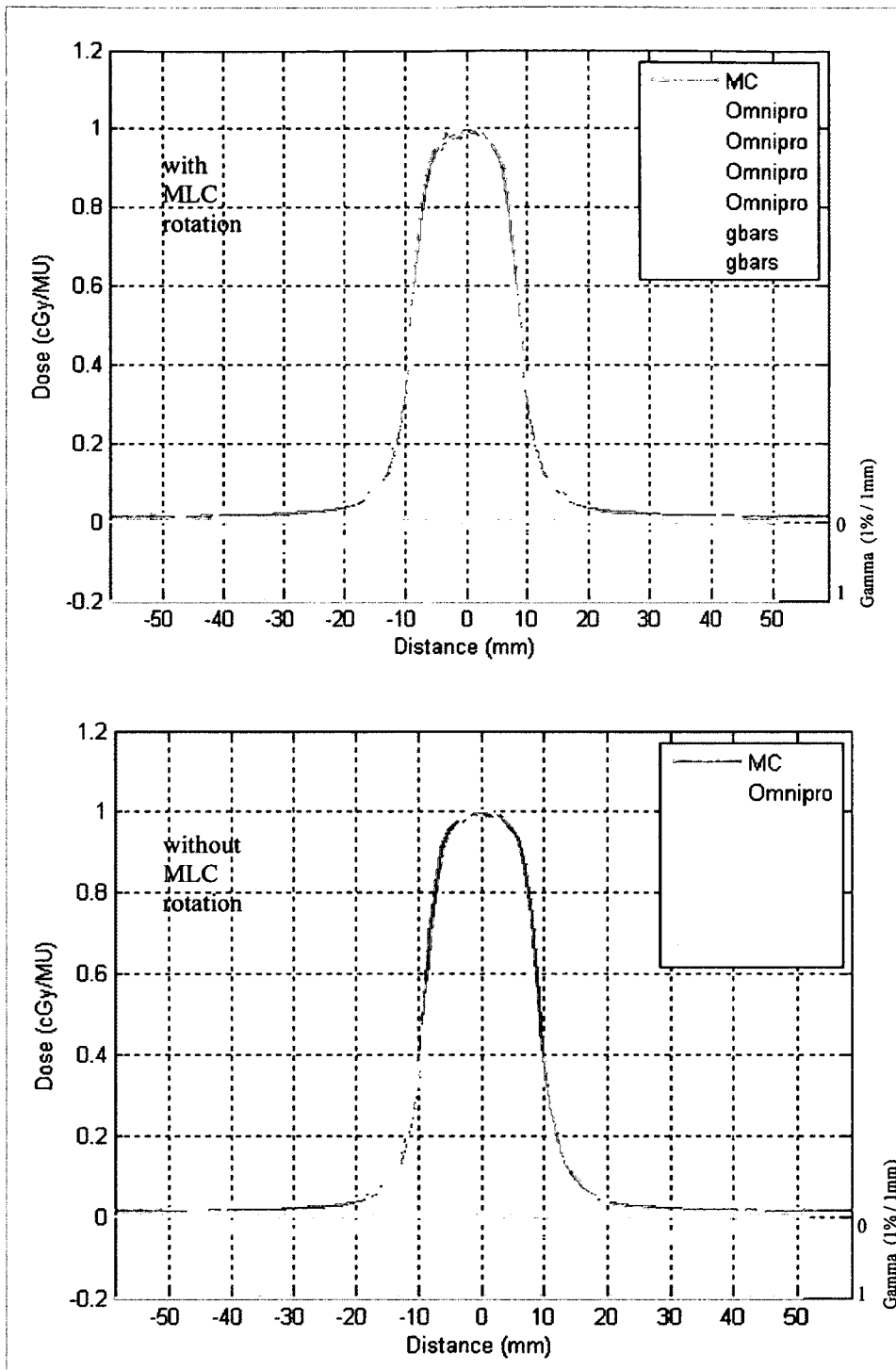
**Figure 2.18** Monte Carlo simulation of tongue and groove dose for the Elekta SynergyS treatment unit. The tongue & groove dose is obtained by summing the dose calculated for a given set of open leaves and the dose calculated with the opposite field (leaves that were closed are opened and vice versa). The blue line is for an MLC rotation of 5 degree and the red line is for an MLC rotation of 3 degrees. Only one of the added profiles is shown in light blue and pink (one for each MLC rotation).

Figure 2.20 shows the results of a Monte Carlo simulation of an inplane off-axis dose profile at 5 cm depth, SSD 100 cm for a field size of 1.6 cm defined on the isocenter plane (4 leaves are opened). The MC simulation performed with an MLC rotation of 5 degrees and a translation of 2.2 mm matches the measurements well. The agreement is

clearly worse and similar to the TPS for the MC simulation performed without the MLC rotation. Several MLC parameters used to model the MLC geometry (physical size of the tongue, groove and leaf width, leaf radius, etc.) are not provided explicitly in this work because the data were derived using as a starting point confidential information from the manufacturer.



**Figure 2.19** Inplane off-axis dose profile at 10 cm depth, SSD 100 cm for a field size of 4 cm defined on the isocenter plane. The red line is for the convolution-superposition algorithm and the black line represents the measurements. The measured field size (FWHM) is smaller than the treatment planning field size because of the defocused leaf side.



**Figure 2.20** Inplane off-axis dose profile at 5 cm depth, SSD 100 cm for a field size of 1.6 cm defined on the isocenter plane (4 leaves are opened). MC simulation performed with an MLC rotation of 5 degrees and a translation of 2.2 mm (top) matches well the measurements (Omnipro). The agreement is clearly worse for the MC simulation performed without the MLC rotation (bottom). The bottom of each figure shows an error analysis (gamma 1% / 1mm).

### 2.3.3 Validation of the MC model of a HT treatment unit

The electron beam was tuned to fit dose measurements using a Gaussian cylindrical shape with a FWHM of 1.4 mm, a mean energy of 5.2 MeV, a Gaussian mean angular spread of 1.075 degrees and a Gaussian spectrum with a FWHM of 0.6 MeV truncated to  $\pm 0.5$  MeV. Not having access to technical data from the manufacturer made the modeling task more challenging since some components are not easily accessible for caliper measurements. For example, the choice of the mean energy was found to be quite dependant (5.2 - 6.0 MeV) on the composition and the thickness of the hardening plate located directly above the ion chamber. Relative dose agreement when compared with measurements is within 1 % for PDD curves and 0.6 % for RDF including field sizes as small as 1.25 cm x 2.5 cm (2 leaves opened). The jaw field edge positions are also within 1% of the field size. Absolute dose agreement for static fields between MC calculations and measurements is within 2 % / 1 mm as shown on Figure 2.21a. The comparison between measurements and the HT TPS is shown in Figure 2.21b. Determining the expected field size position may be confusing for a cone shaped transverse profile and MLC collimation including a tongue and groove pattern. The situation is also complicated by the fact that the MLC is not perfectly focused on the target and that the HT system is a pre-packaged "black box" requiring no modeling. The changes introduced in the MLCE BEAMnrc component model to account properly for the arc shape of the MLC bank and the defocusing of the leaves helped reduce residual error in the off-axis dose profile edges. Figure 2.22b shows the improved agreement at the transverse field edge for the largest field size following the modifications and figure 2.22a shows a

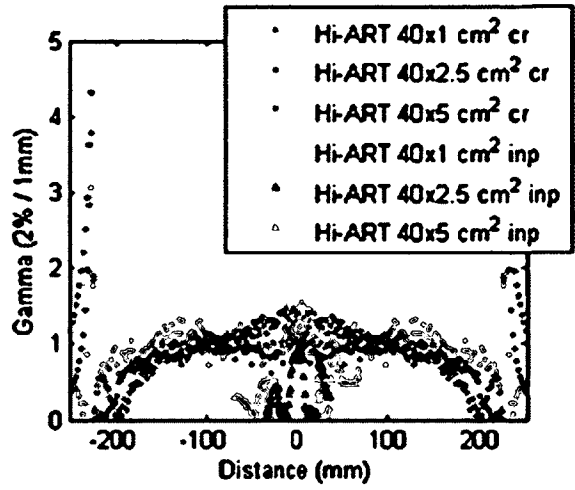
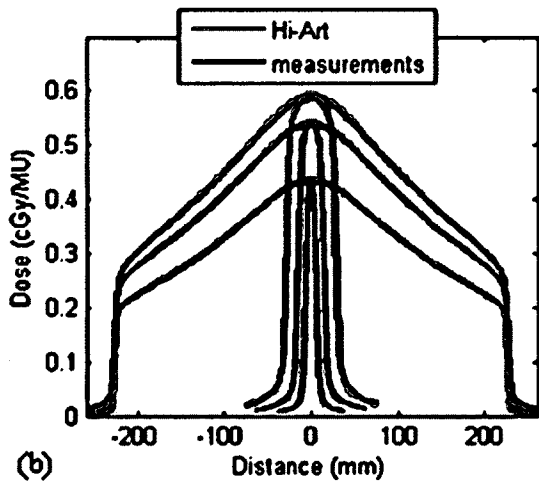
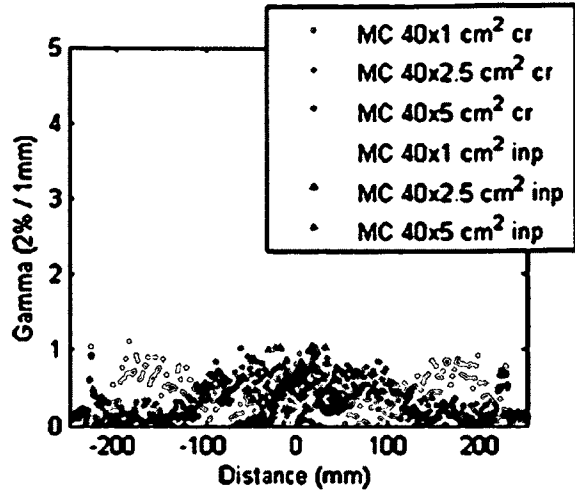
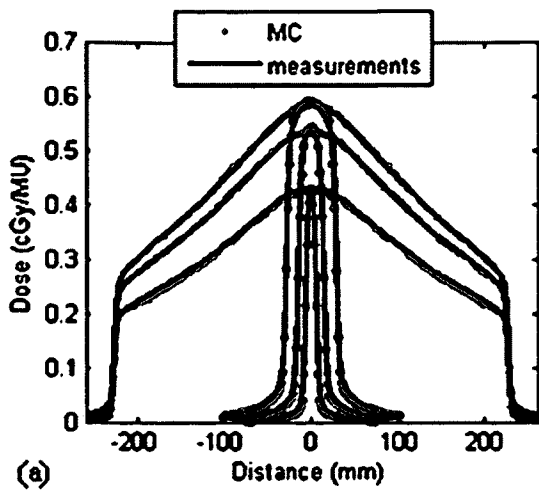
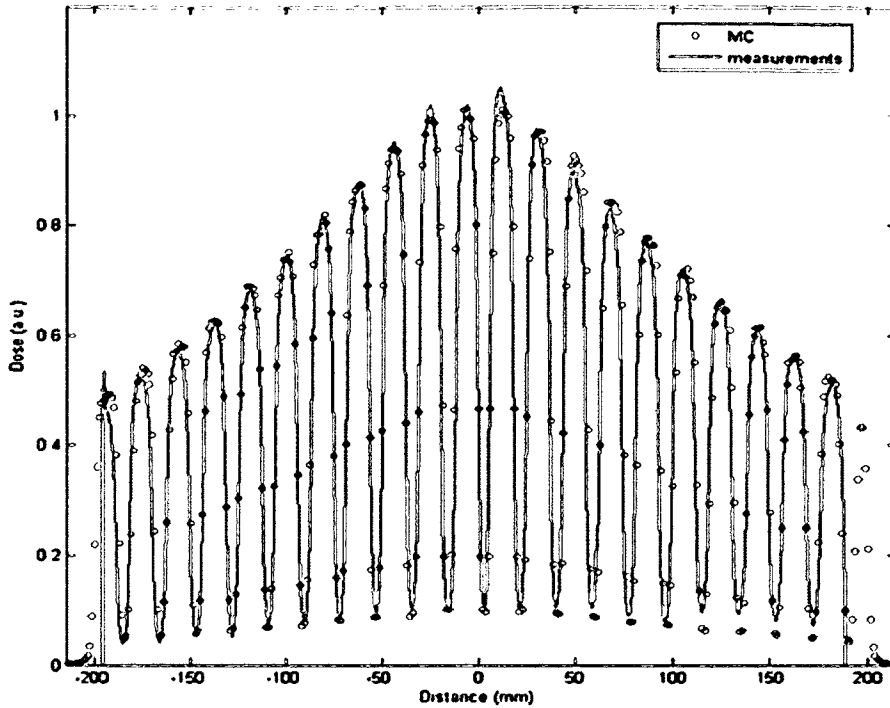
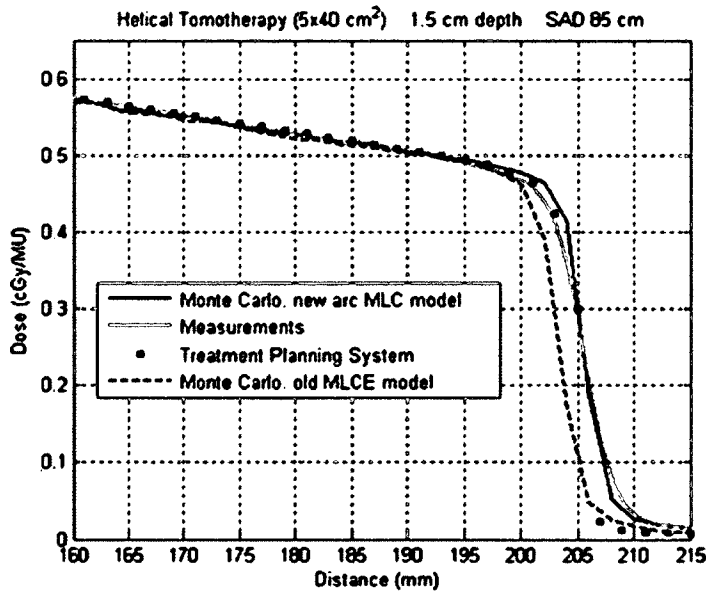


Figure 2.21 (a) HT MC-simulated and measured absolute dose profiles in crossplane (cr) and inplane (inp) directions at 10 cm depth for three different jaw field sizes (left). Gamma analysis for the same profiles is shown on the right. Also shown are comparisons between the Hi-Art HT TPS and measurements (b). (source: Paper I reproduced with permission)



(a)



(b)

Figure 2.22 (a) MC-simulated and measured dose profiles (crossplane) for the helical tomotherapy accelerator for a 1 cm jaw field size and an alternating pattern of 2 closed leaves and 2 opened leaves. Film data at both ends of the measurement are distorted due to film edge effect. (b) Helical tomotherapy accelerator transverse profiles comparison for the largest field size following modifications to the MLCE BEAMnrc component module. (source: Paper I reproduced with permission)

comparison with measurements for an alternating pattern of "2 closed leaves / 2 opened leaves". The MLC parameters (tongue and groove, interleaf air gap, width) were fine tuned by simulating the transmission dose through and between the leaves. Figure 2.23 shows the transmitted dose (relative to an open field) at 5 cm depth. The agreement between the MC simulated transmitted dose (~0.3%), the film / ion chamber measurement and values in the literature (Zhao *et al.*, 2008) is within 0.1%.

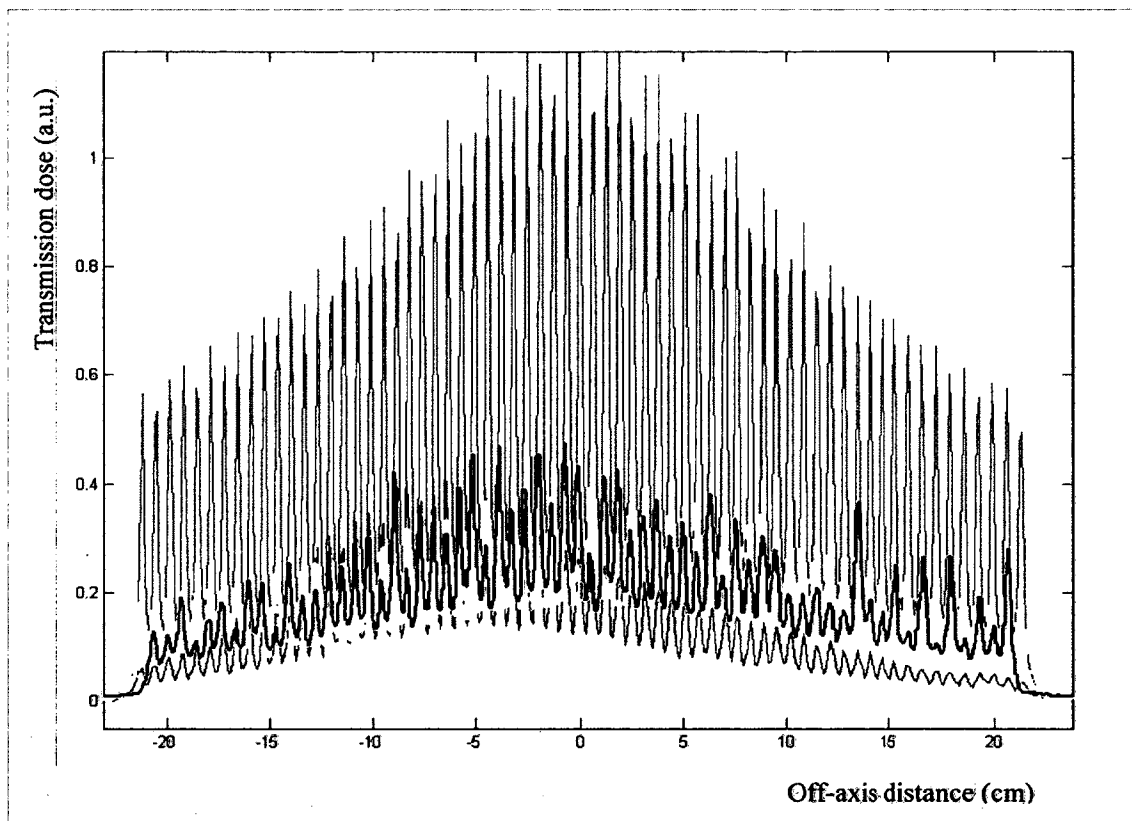


**Figure 2.23** Transmission dose at 5 cm depth for the tomotherapy accelerator (normalized to an open field dose for a 5x40 cm<sup>2</sup> field size). Film measurements (normalized with ion chamber) are shown in black and Monte Carlo simulations are shown in yellow. The blue line and the red line are included to illustrate the impact on the Monte Carlo transmitted dose of sub-mm changes in the MLC geometry parameters.

The MLC parameters were also fine tuned by simulating the tongue and groove effect discussed before. Figure 2.24 shows the tongue and groove effect at 5 cm depth for the combination of two fields having respectively odd and even leaves opened. An opening

of 6 leaves was created for both fields at an off-axis distance of 2.5 cm to allow the measurement of the dose with an ionization chamber without volume averaging error. The ionization chamber measurement was used to normalize the film measurement. The junction between opposing fields is clearly visible as an underdose of about 12%, which is in agreement with film / ion chamber measurements. The symmetry of the tongue and groove curve is routinely used in machine maintenance to properly align the MLC with the beam focal spot when the machine is modified or disassemble for repair. The primary

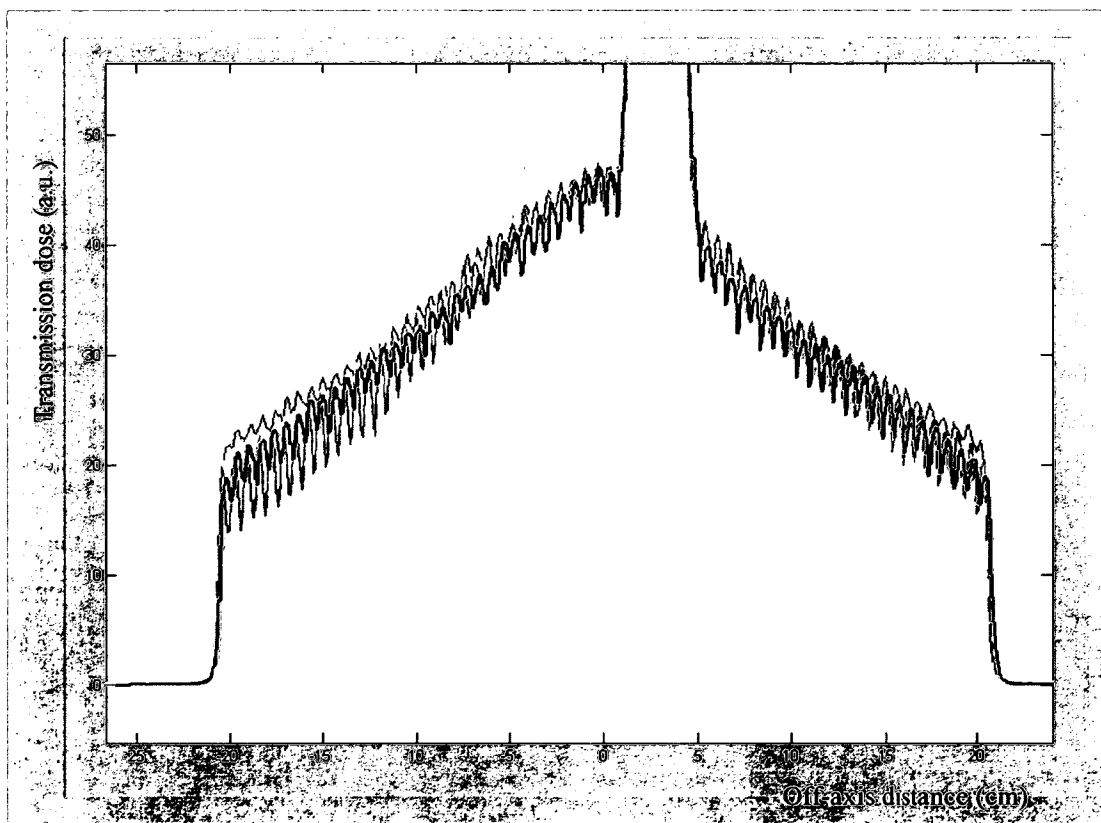


**Figure 2.24** The tongue & groove dose is obtained by summing the dose measured or calculated for two opposing fields having respectively odd and even leaves opened. Film measurements (normalized with ionization chamber reading in the small open section of the field) are shown in black and Monte Carlo simulations are shown in yellow. The blue line and the red line are included to illustrate the impact on the Monte Carlo simulation of sub-mm changes in the MLC geometry parameters.

source shielding was discussed in section 2.2.4. Figure 2.9 is an example of photon fluence reduction measurement routinely performed with the on-board detector to update treatment planning parameters. This information is used after the treatment planning process to modify the MLC sinogram. In our case, the Monte Carlo simulation already accounts for this effect to first order so we validated the model using MC simulation of a modulated field shown in figure 2.25. The couch and the gantry are static and the field contains openings of different sizes (1 leaf, 2 leaves, 3 leaves) at various off-centered positions. The agreement between the MC simulation and the film / ion chamber measurements was found to be within 2.5%. The impact of this error in the overall patient dose distribution is much smaller because small leaf openings have a small weight in patient treatment plans. The impact is also smaller because patients are not treated with a static gantry and a static couch and the resulting dose profile would generally be blurred (convolved) by such motion as described earlier in figure 2.11.

### **2.3.4 Testing the MC model of a conventional treatment unit**

TPS plan information was used to generate CPDFs for time dependant parameters to include them in the BEAMnrc input files. Examples of MC-calculated transverse dose distributions and comparison with the TPS dose distributions are shown in Figures 2.26a, 2.26b and 2.27a. The agreement is within 3 % / 3 mm for all relevant voxels (not located in surrounding air, immobilization device, couch, etc...). Figure 2.3 in section 2.2.1 shows the extracted CPDFs for the same treatment plans. Figure 2.28 also shows an example where the effect of rigid motion is incorporated in the dose distributions of a VMAT SABR lung treatment for one fraction. A sinusoidal function with a period of 6

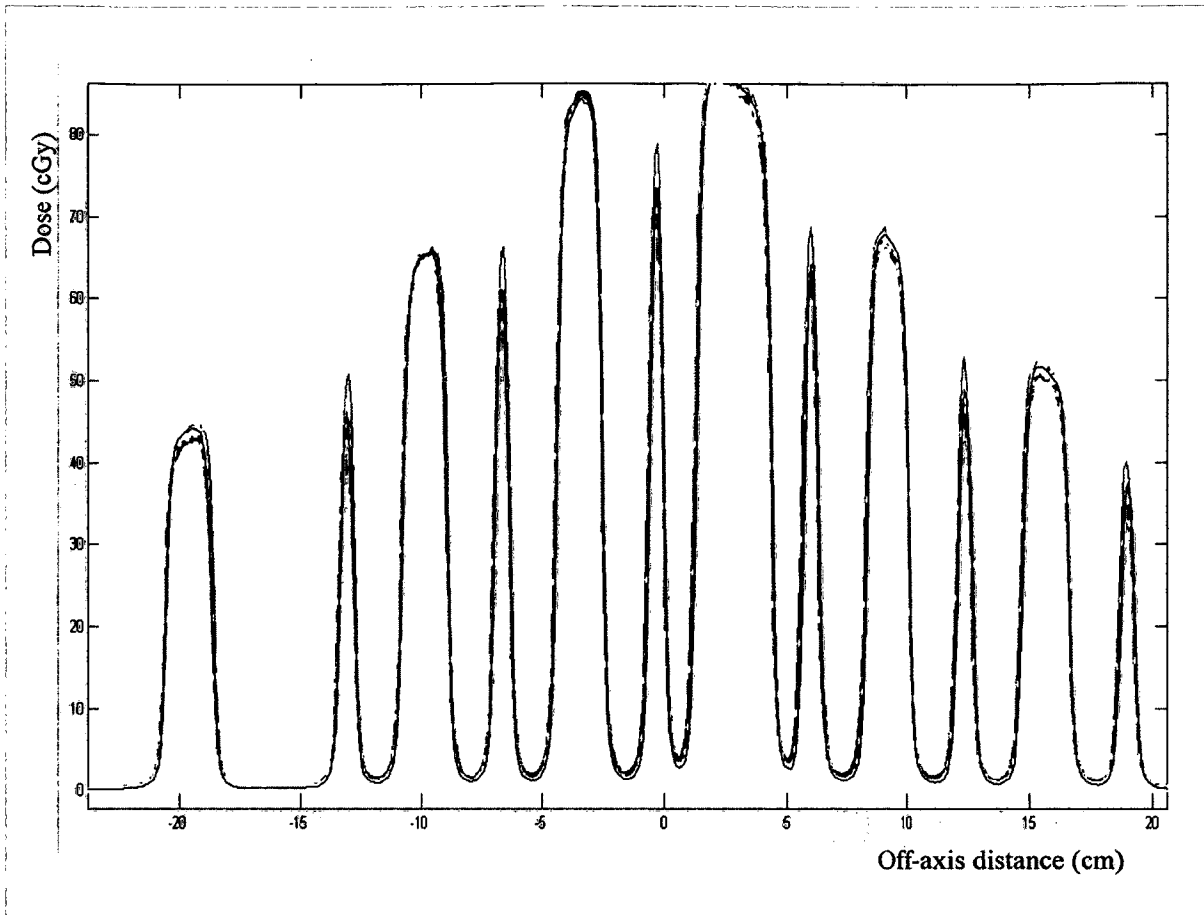


**Figure 2.25 MC simulation of a modulated field. The couch and the gantry are static and the field contains openings of different sizes (1 leaf, 2 leaves, 3 leaves) at various off-centered positions. Film measurements (normalized with ionization chamber reading in the largest open section of the field) are shown in black, SFD diode measurements are shown in red and Monte Carlo simulations are shown in yellow. The blue line is included to illustrate the impact on the Monte Carlo simulation of sub-mm changes in the MLC geometry parameters.**

seconds and amplitude of 5 mm was used for all 3 standard motion directions. Finally, figure 2.29 shows an example of MC Monte Carlo simulation of a 3D-CRT SABR lung treatment (no motion included in the simulation) and compared with the TPS dose calculation for a patient with two tumours including one with extremely low density. This case was included in the investigation because quality assurance methods for verifying the treatment plan dose calculation accuracy were reporting dose errors on the order of

30% in the target volume. For a typical SABR lung treatment case, the error is within 5%, which is considered acceptable considering that the quality assurance method is

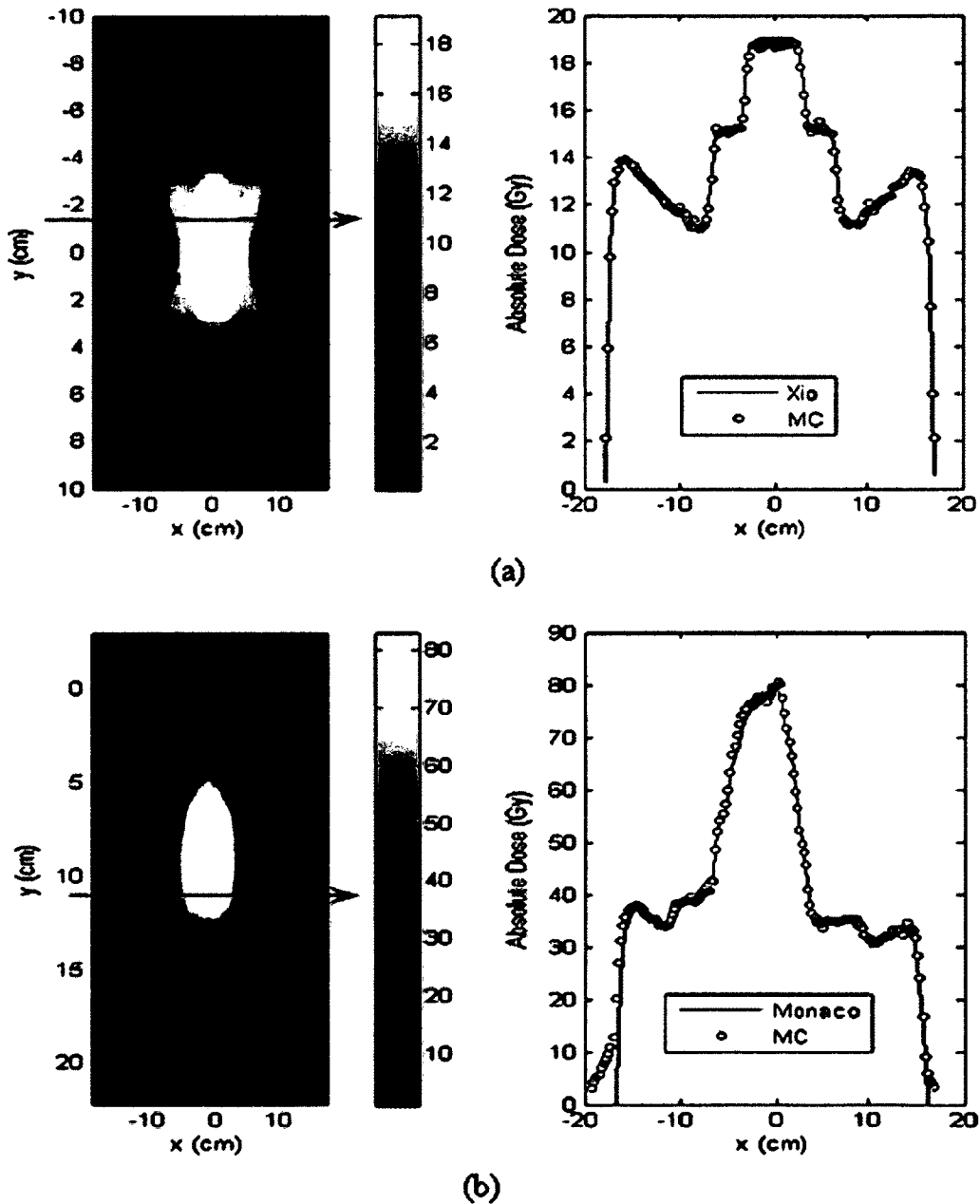


Figure 2.26 MC-calculated transverse dose distribution (left) and comparison with the TPS (right) for (a) 3D-conformal, (b) step-shoot IMRT. (source: Paper I reproduced with permission)

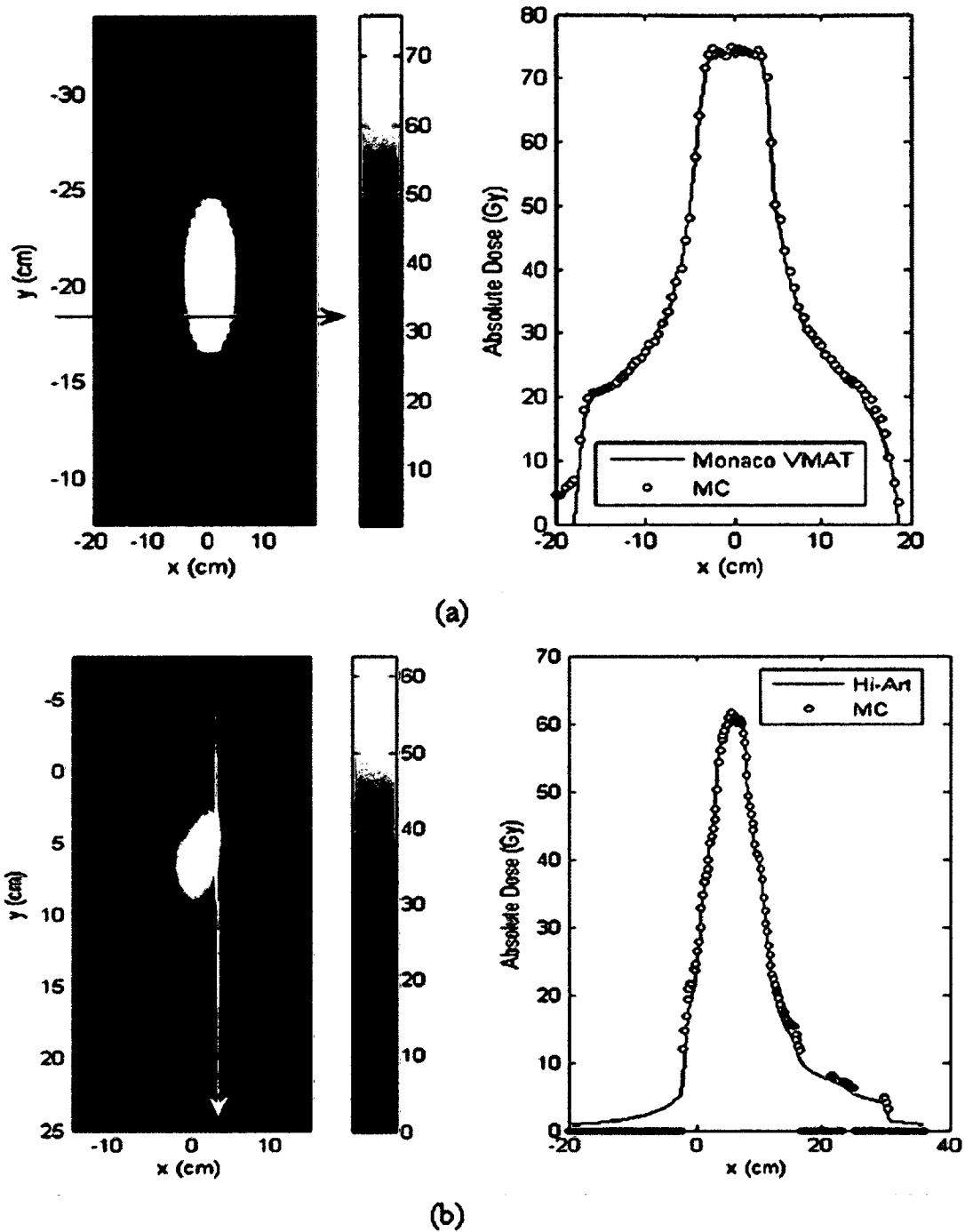
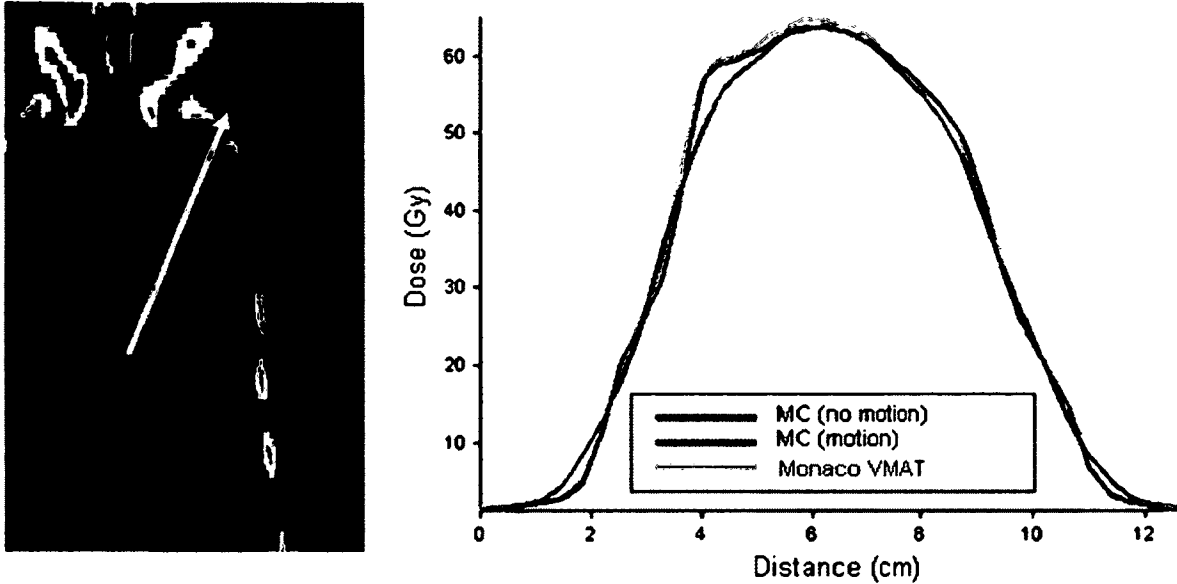


Figure 2.27 MC-calculated transverse dose distribution (left) and comparison with the TPS (right) for (a) VMAT prostate case (b) helical tomotherapy brain case. MC-calculated dose for points located in air were zeroed for the helical tomotherapy brain case. (source: Paper I reproduced with permission)



**Figure 2.28** MC-calculated transverse dose distribution (left) and comparison with the TPS (right) for a VMAT lung stereotactic treatment. The comparison also includes MC calculations performed with rigid patient motion (sinusoidal function with amplitude of 5 mm and a period of 6 seconds for all three standard motion directions). (source: Paper I reproduced with permission)

based on a primitive dose calculation algorithm (i.e., dosimetry function using density scaled depth and field size). The result of the MC simulation is in agreement (within 3% of the prescribed dose) with the TPS dose calculation for the target volume. The results also show that the TPS is overestimating the low dose received by the lung tissues (difference of 5 % in the volume of lung receiving 5 Gy), a common plan parameter used to assess the risk of lung complications following treatments.

### 2.3.5 Testing the MC model of a HT treatment unit

As explained earlier, TPS plan information was extracted from the DICOM files, the MLC sinogram file and the XML archive patient file. This information was used to generate CPDFs for time dependent parameters to include in the BEAMnrc input files.

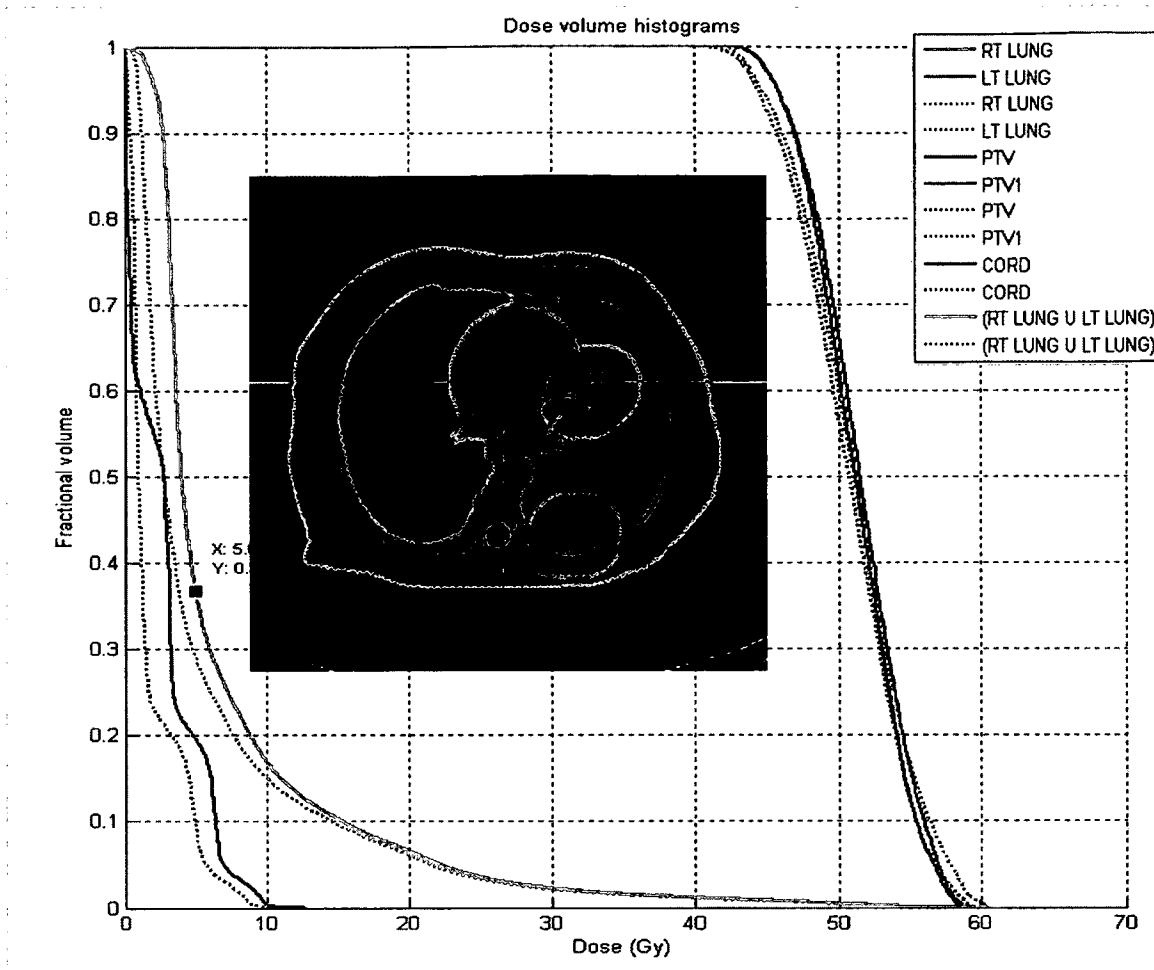
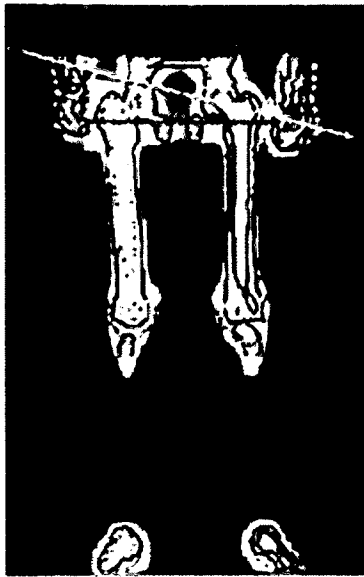
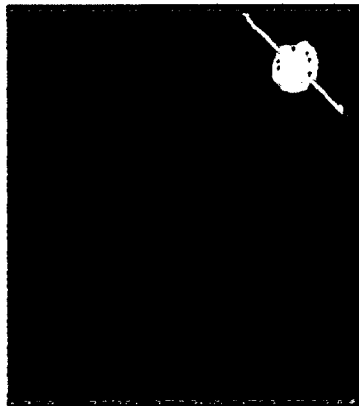
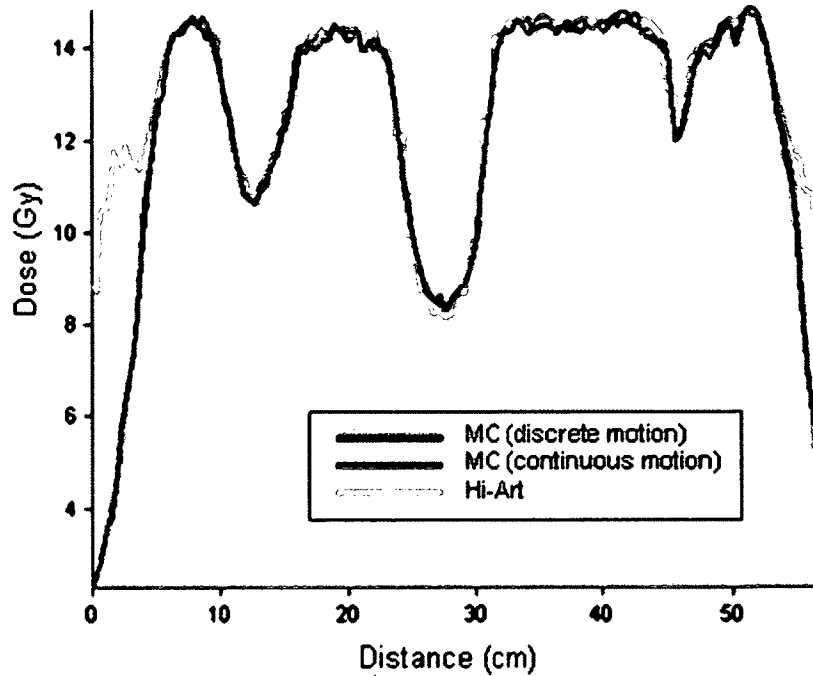


**Figure 2.29** MC-calculated transverse dose distribution (insert) for a 3D-CRT double tumour lung stereotactic treatment. Dose volume histogram shows the results of the MC simulation (dotted line) and the treatment planning system dose calculation (solid line).

The tabulated data were plotted for several parameters in figure 2.3 (section 2.2.1) for the brain case. An example of a MC-calculated transverse dose distribution for a simple brain case and compared with the TPS dose distribution is shown in Figure 2.27b. The agreement is within 3 % / 3 mm for all relevant voxels. A second example for an "extreme" case is shown in Figure 2.30b. Differences between MC and TPS are well above 10 % / 5 mm near the edge of the PTV. To confirm that this difference is caused by the use of discrete angles and not by a problem with our method, a second MC



(a)



(b)

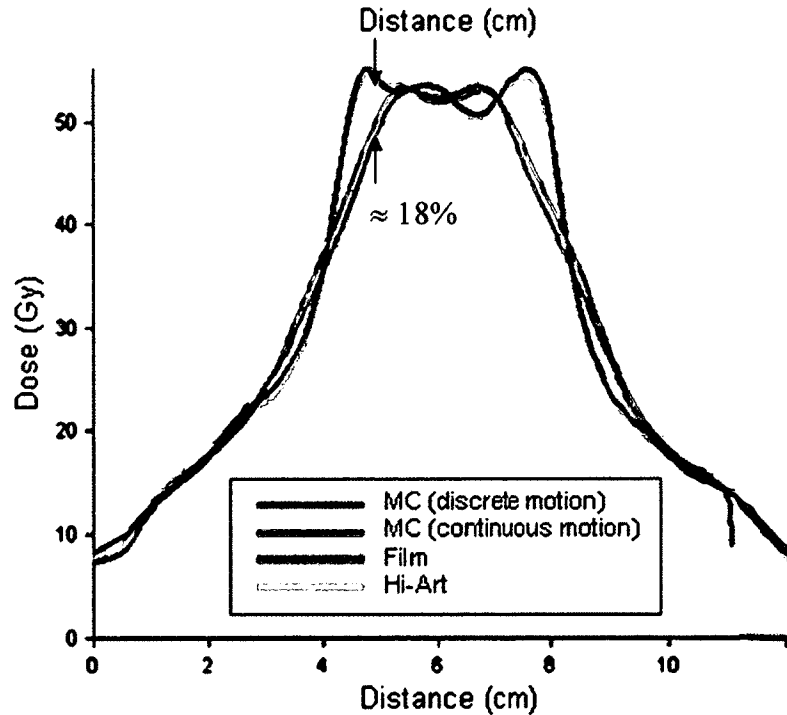
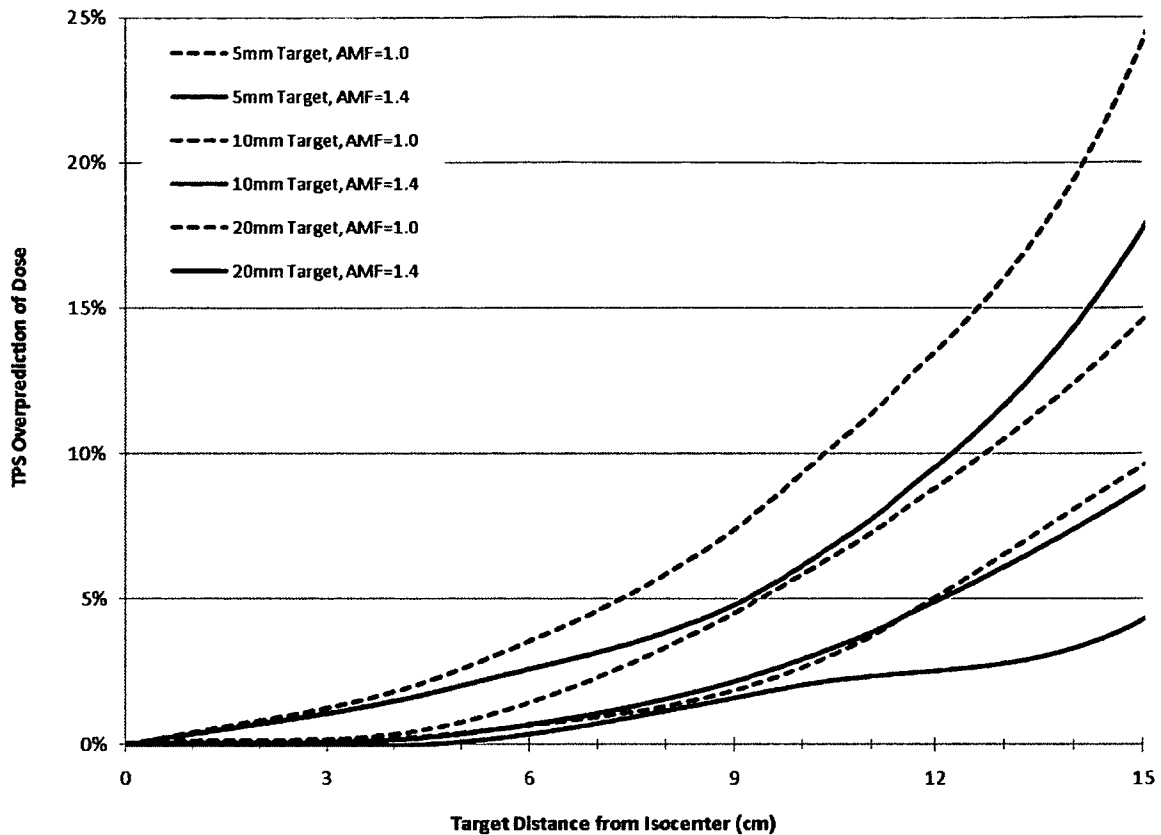


Figure 2.30 MC-calculated transverse dose distribution (left) and comparison with the TPS (right) for (a) HT TMI case (b) HT "extreme" case. The comparison also includes MC calculations performed with discrete angles to simulate the TPS algorithm and film measurements for (b). The "extreme" case is used to illustrate the effect of gantry angle discretization: a fast treatment (modulation factor of 1.1) of a 3 cm diameter cylindrical target in a solid water phantom located at about 15 cm from the isocenter. (source: Paper I reproduced with permission)

calculation was performed with discrete angles to simulate the TPS algorithm and is shown to match within 1 % the TPS in Figure 2.30b. Finally, a film measurement was also performed to validate the model and is shown to match the PPS MC simulation within 2 % / 1 mm in Figure 2.30b. The case studied in Figure 2.30b is an extreme case (low modulation factor, 15 cm off-centre) and is not representative of the vast majority of cases treated with HT. For example, Figure 2.30a shows two MC transverse dose distributions (continuous motion and discrete angles) for a TMI case and a comparison with the TPS dose distribution. The patient's hands are located at about 20 cm from the isocenter but there is practically no angle discretization effect since the volume treated and the modulation factor are much larger. More recently, the manufacturer reported a study (TomoTherapy, 2011) showing that gantry discretization combined with low modulation factor and small target volume may result in treatment planning dose overestimation as large as 25% in the center of the target as shown in figure 2.31.

## **2.4 Discussion**

There are several advantages to the position-probability-sampled method implemented in BEAMnrc/DOSXYZnrc as compared with a SCS method previously implemented at our center. First, the simulation is done with a higher degree of fidelity and is therefore more accurate as shown by figure 2.30b for an extreme HT case. In HT, the opening time for each leaf is modified in the TPS optimization process using pre-calculated beamlets. Since the opening time is not known in advance, the beamlets and ultimately the optimized dose don't incorporate the source motion within each sub arc.



**Figure 2.31** Tomotherapy treatment planning system dose overestimation (calculated / measured) caused by gantry discretization for small target volume treatments performed with low modulation factor (source: TomoTherapy Inc., field safety notice 5089 reproduced with permission).

This effect was modeled previously by Kissick et al. (Kissick *et al.*, 2007) with the use of a delivery transfer function to account for the source motion blurring. They concluded that the cost-benefit ratio to incorporate these effects into the dose optimization and calculation is high. As shown for the brain case and the TMI case (figure 2.27b and 2.30a) and as observed for many other cases retrospectively (not shown), the effect of source motion is indeed clinically negligible for most clinical cases. However, for specific HT treatment plans when this may not be the case (figure 2.30b), the impact on the dose distribution should be analyzed carefully in an appropriate plane as part of the plan quality assurance process. The MC method implemented as part of this

project is a valuable tool to extend the quality assurance process done with measurements to the full 3D patient geometry and to incorporate at the same time the additional impact of tissue heterogeneities and patient motion as shown in figure 2.28 and 2.29. The HT treatment unit was modeled previously using an SCS approach in BEAMnrc/DOSXYZnrc by (Zhao *et al.*, 2008) but their model did not include the continuous motion of the source within each HT projection. Such a model would therefore reproduce the discretization issues related to the TPS. A second model by Sterpin *et al.* (Sterpin *et al.*, 2008) was designed with the Penelope MC code using an SCS approach and allowed for sub discretization of the source motion within each HT projection. The main goal of their study was to explore extreme cases in terms of heterogeneity corrections (e.g., small lung tumours) but no discussion was provided regarding the appropriate selection of discretization interval for dynamic parameters. For selective HT cases (e.g., TMI), we found that the PPS method allows a simpler approach by using only the MLC sinogram as a CPDF for sampling the MLC position (2,675 control points instead of 300,000). As a natural extension of the proposed PPS method, it is also possible to model the actual opening and closing of the leaves or any latency issues by only adding one step in the sampling process. This feature could be useful as part of a machine quality assurance program to investigate pass / fail tolerance levels for various dynamic parameters in more detail. Modeling this motion with the SCS method would require adding a large number of simulations and/or evaluating carefully the impact of any level of discretization on the results.

Similar comments may also be made about conventional treatment units. The use of the PPS method for simulating the dynamic motion of the collimator (e.g. leaves, jaws)

was used in the past for simulating virtual wedges, sliding-window IMRT and VMAT treatments. For example, Bush *et al.* (Bush *et al.*, 2008) published a model based on the SCS approach for the patient portion of the simulation that included sub-discretization of VMAT arc segments in DOSXYZnrc. However, the BEAMnrc component of the simulation was based on a PPS approach to model the rapidly changing MLC configuration. We did not expect to find issues for VMAT cases explored as part of this study since the Monaco TPS used for leaf position optimization is already based on a full PPS MC dose calculation algorithm. It is also fair to say that the need for a PPS method for the patient component of the MC simulation (DOSXYZnrc) is not obvious for conventional treatment units since a single VMAT arc may well be simulated using an SCS approach with a reasonable number of independent simulations (1000 control points) to provide an acceptable error (discrete gantry angle spacing of 0.36 degrees). The drawbacks of the PPS method also include the loss of information (i.e., the dose for each beam is replaced by the total dose), an increase in memory requirements to store the time varying geometry parameters and a minor increase in computational time to sample the geometry. In our case, the memory requirement was not an issue and we found that the small increase in computational time was compensated by more stability (i.e., less network traffic, less input / output, easier to restart the simulation to lower the uncertainties), and by not having to steer and sum a very large number of individual simulations. The PPS method is also preferable since evaluation of the appropriate discretization levels is not required before doing a simulation or to investigate the time sampling correlation between the various dynamic variables, particularly in cases where there are large differences between motion patterns. In principle, running many

independent beam simulations for each beam shape (SCS) should be much more efficient than that described in this study because each of the simulations may be performed with a different directional bremsstrahlung splitting radius. In practice however, using a smaller radius centered on the isocenter is often not possible due to the elongated slit beam design of the HT treatment unit and the off-axis position of several apertures delivered using conventional treatment unit. We also found that using a too small radius combined with a large directional bremsstrahlung splitting number introduced several artifacts caused by "fat" particles. This was particularly obvious for large treatment volumes where a lower splitting number and a larger radius were required (e.g., TMI). Overall, the simulation efficiency was found to be suitable for a dose calculation verification tool and no attempts were made to improve it.

## **2.5 Conclusion**

We have described the development of a method for performing complete position-probability-sampled Monte Carlo dose calculation using the BEAMnrc / DOSXYZnrc code. The method includes full accelerator head simulation and a realistic representation of the continuous motion, with no resort to discretization approximations or analytical procedures. A single Monte Carlo simulation may thus be performed to calculate the patient dose for various types of treatment techniques delivered using a conventional or a HT treatment unit. The method simplifies the simulation process, improves the dose calculation accuracy and involves an acceptably small change in computation time. Absolute dose agreement for static fields between MC calculations and measurements is

within 2 % / 1 mm. Absolute dose agreement between MC and TPS for four types of treatment techniques was determined to be 3 % / 3 mm.

## **3 Patient modeling**

### **3.1 Introduction**

In chapter 2, we presented a method to perform position-probability-sampled Monte Carlo dose calculations in the BEAMnrc and DOSXYZnrc user codes of EGSnrc. The method includes full accelerator head simulation of HT and conventional treatment units and a realistic representation of machine continuous motion via the sampling of a time variable. In this study, the DOSXYZnrc user code was further modified to account for the continuous intra-fraction deformation of the patient geometry.

Section 3.2.1 describes how information about the patient is acquired and how it is used to modify the transport grid densities (patient geometry) as a function of time during the Monte Carlo simulation. Section 3.2.2 describes how the energy deposited in the time dependant transport grid (e.g., inhale) is mapped back to a reference grid (e.g., exhale). Section 3.2.3 describes the measurements performed to validate the implementation of this method. Chapter 4 gives an example of application of the method for SABR lung treatments with intra-fraction motion.

### **3.2 Materials and methods**

#### **3.2.1 Patient geometry**

##### **3.2.1.1 Deformable image registration**

The 4D voxelized geometries (densities) are obtained from a helical 4D-CT scanner and exported as ten breathing phase density matrices. Deformable image registration (DIR) is

then used to generate deformable vector fields (DVF) to relate densities in each breathing phase to a reference breathing phase ( $9 \text{ DVFs}_{\text{ref}}$ ) as well as to its neighbor breathing phases ( $9 \text{ DVFs}_{\text{neighbor}}$ ). The DIR algorithm used is an inverse consistent method based on symmetric optical flow (Yang *et al.*, 2008; Yang *et al.*, 2011a). Figure 3.1 shows some of the DIR parameters used and shows an example of DVF superimposed on a coronal view of the lung and the diaphragm. Inverse consistency means that the registration results are consistent when registering the images in both backward and forward directions (e.g. from the transport grid to the reference grid and vice versa). This feature is desirable for the DIR algorithm in addition to its accuracy to ensure more unbiased detection of voxel compression and dilatation (Leow *et al.*, 2005), which helps to minimize errors in the implementation of this 4D MC method. In figure 3.1, the parameter “Stages to use” is the number of multi-resolution (or multigrid) stages to use. As explained in section 1.6.2, the optical flow transformation model relies on the assumption of small displacement of intensity pattern ( $\sim$ voxel size) which requires the use of multi-resolution strategies (starting with large voxel size and then gradually moving to smaller voxel size). The parameter “num of passes” is the number of time the registration is performed at each image resolution and the parameter “num of iterations” is the number of iteration of equation 1.17 used for each pass. Multiple passes with small number of iterations for each pass may often generate better results than one pass with larger number of iterations. The parameter “stop condition 1” is the iteration stop condition and the value is in unit of pixel. The iteration will stop if the change in the motion field is less than this value. The parameter “stop condition2” is the pass stop condition. The pass will stop if the change in the motion field is less than this value. The parameter “Smoothing” is used to control the

amount of vector field smoothing (related to the parameter  $\alpha$  in equation 1.17). The parameter “more smoothing” allows additional smoothing of the vector field after each pass, multigrid stage or final calculation. Only the first values is used in this work and it sets the sigma of a Gaussian low pass filter. Finally, the parameter “multigrid filter” is the type of filter used for computing the down-sampled image intensity at the beginning of each multigrid stage.

As part of the patient planning process, an internal target volume (ITV) is drawn by a radiation oncologist on one patient geometry (free breathing CT) using 4D-CT information. A conventional margin of 5 mm is then added to the ITV in all directions to create the planning target volume (PTV). The gross tumour volume (GTV) is rarely contoured on each of the 4D-CT breathing phases. Those contours are instead automatically extracted using an algorithm based on the ITV contours and known motion of the tumour pixels ( $DVF_{\text{ref}}$ ). More specifically, the GTV contour starts with one pixel in the center of the ITV for a reference breathing phase. At each iteration, the GTV contour is enlarged by one surrounding pixel and the new included pixel is accepted if it does not escape the ITV contour when applying each of the nine breathing phase DVF. The process is stopped when there is no more available pixel to try in the ITV contour of the reference breathing phase. The extraction of the GTV contour was done this way to make sure that the GTV motion is contained within the ITV in the Monte Carlo simulation to avoid plan degradation due to small mismatch between DVF motion and the radiation oncologist’s perceived motion when drawing the ITV. Since the GTV is rarely contoured explicitly in all breathing phases, it was not impossible to quantify this mismatch for the study. However, as a sanity check on the DVF, figure 3.2 shows an

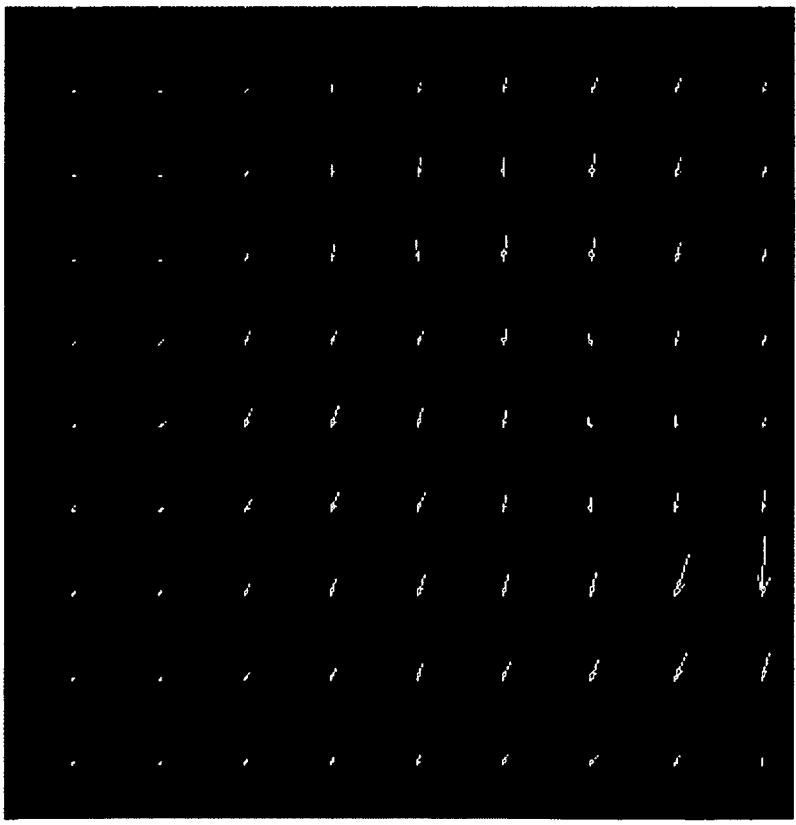
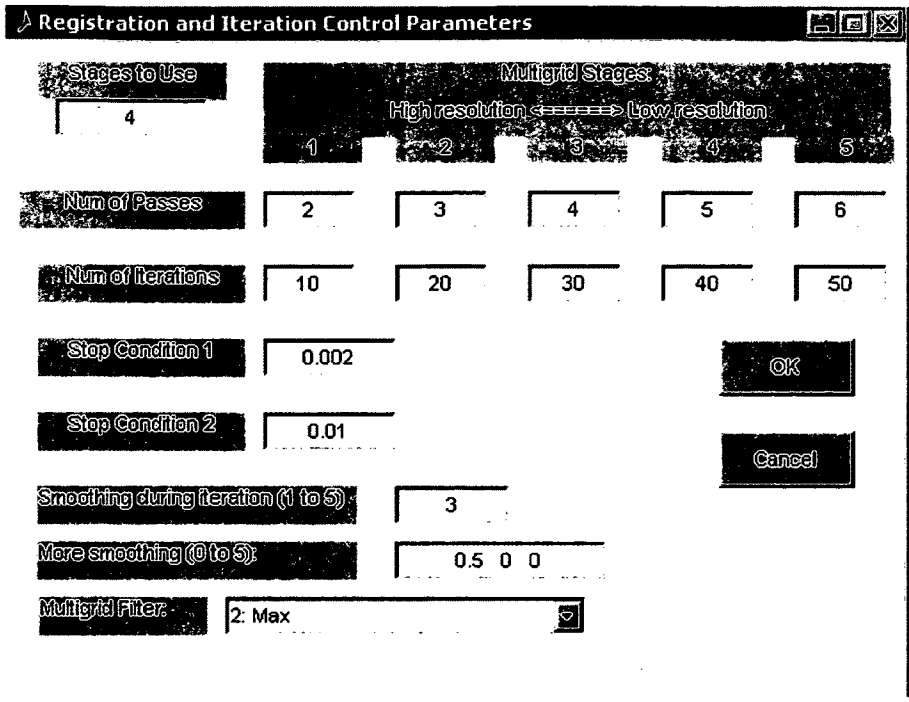


**Figure 3.1** Deformable image registration parameters (top) and example of deformable vector field superimposed on a coronal view of the lung and the diaphragm. Both figures were generated using modified versions of the DIRART open source package.

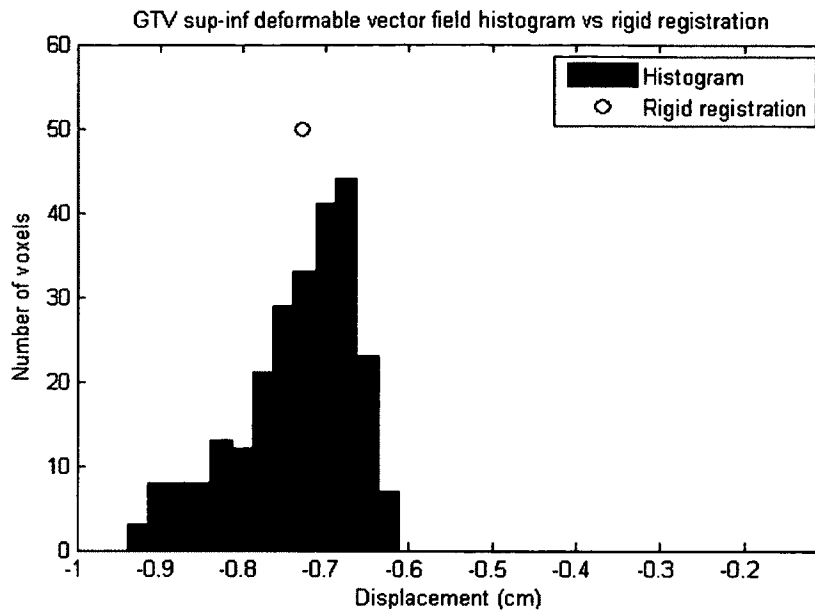


**Figure 3.2** Histogram of GTV voxel displacement in the sup-inf direction with respect to a reference phase (e.g., exhale) based on deformable image registration. The result based on rigid registration is also shown as a circle for validation purposes. (Source: Paper II reproduced with permission)

example of a histogram about the displacement of the GTV voxels with respect to a reference phase using both DIR and rigid registration. The low level of tumour deformation ( $< 2$  mm) is consistent with studies reported in the literature (Wu *et al.*, 2009). The position of the tumour in each breathing phase is defined as the centroid of the GTV contour. To minimize the amount of tumour motion between each breathing phase density matrices, DVFs were used to convert the ten 4D-CT density matrices (phase binning) to about seven density matrices with equally space tumour position as shown in figure 3.3.

To allow calculation in the continuous range of breathing phase, we implemented two methods in the DOSXYZnrc user code to modify the patient geometry (transport grid

densities) as a function of time during the Monte Carlo simulation. As discussed in section 2.2.1, a random time value between 0 and 1 is associated to each particle and its progeny at the beginning of each history in the accelerator head. This time value represents the cumulative MU (normalized to the total MU) rather than the exact time measured by a clock at which the particle was emitted during treatment. Using this time variable, the simulation geometry in the accelerator head is changed interactively for each history as the transported particle enters each component module. This time variable is also transferred to the patient geometry where it is used to change the patient densities. To avoid unnecessarily processing a large amount of patient data for each transported particle, the density is changed individually for required voxels as part of the boundary crossing algorithms.

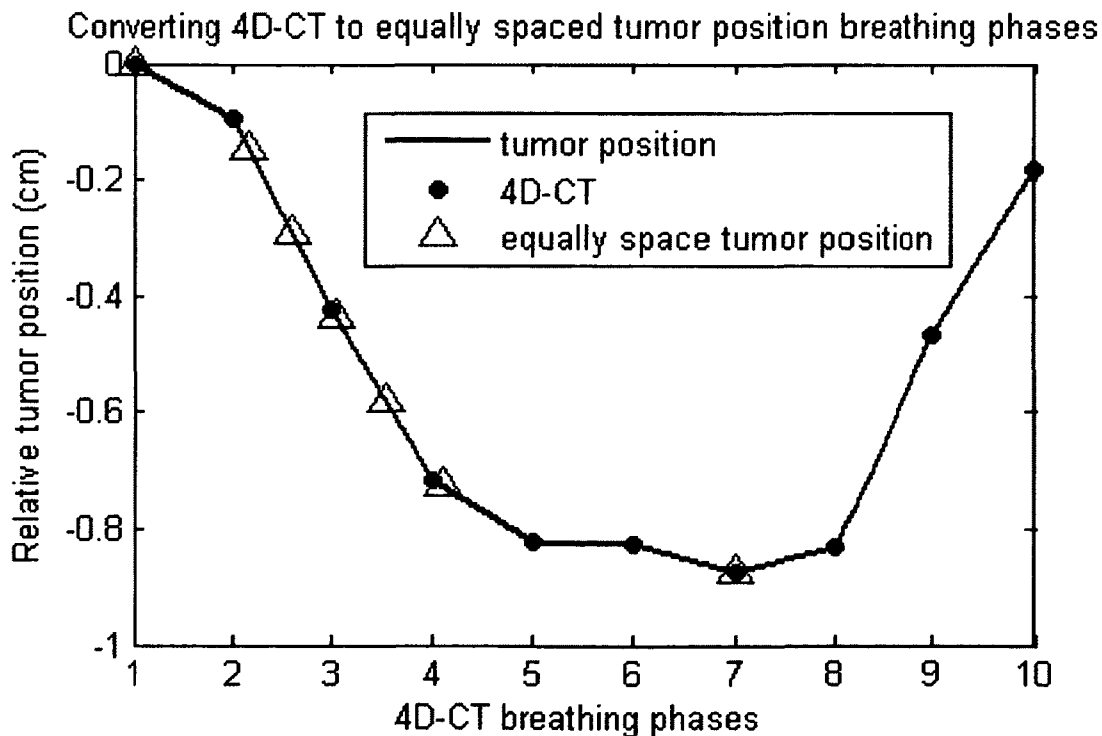


Figure 3.3 Position of the tumour with respect to a reference phase for ten 4D-CT breathing phases and seven breathing phases with equally spaced tumour position. (source: Paper II rep. with permission )

### ***3.2.1.2 Density interpolation***

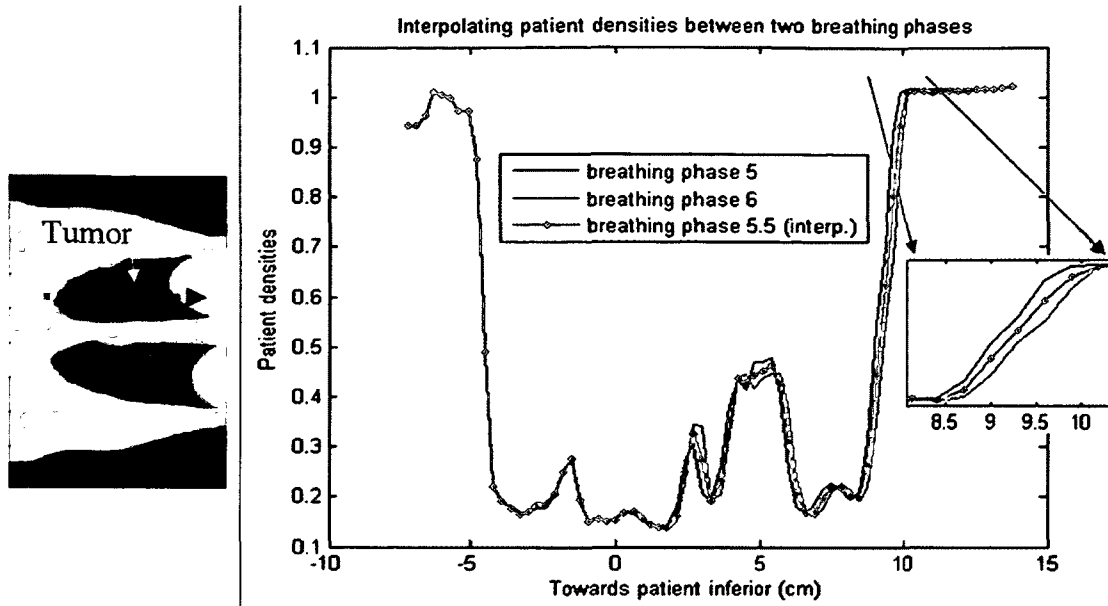
The first approach is defined as density interpolation. Several density matrices are provided in input files together with an interpolation function or table to associate time values with the corresponding breathing phase number. A simple example may be defined for a case with a constant treatment unit dose rate of 10 MU/s and a patient breathing cycle of 10 seconds. Assuming ten 4D-CT breathing phases equally spaced in time, the patient will spend 1 second (or 10 MU) in each phase. In this case, the interpolation table to associate time (actually MU) with breathing phases will be defined as follows:

[ (time breathing phase) ; (0 1) ; (10 2) ; (20 3) ; (30 4) ; (40 5) ; (50 6) ; (60 7) ; (70 8) ; (80 9) ; (90 10) ; (100 1) ; (110 2) ; (120 3) ; (130,4) ... ]

During the simulation, when a particle crosses a voxel boundary in the transport grid, the time associated to this particle is converted to a breathing phase number and the density of the new voxel is then determined by interpolating densities between the two nearest breathing phase density matrices. The use of interpolation is simple but not rigorous since a moving voxel is translating or deforming rather than linearly fading away. However, by minimizing the amount of motion between each breathing phases (e.g. less than 1-2 mm) relative to the voxel size (e.g. 2.5 mm), this approximation may be justified as shown in figure 3.4(a) and figure 3.4(b) (the diaphragm is translating properly between the two phases).

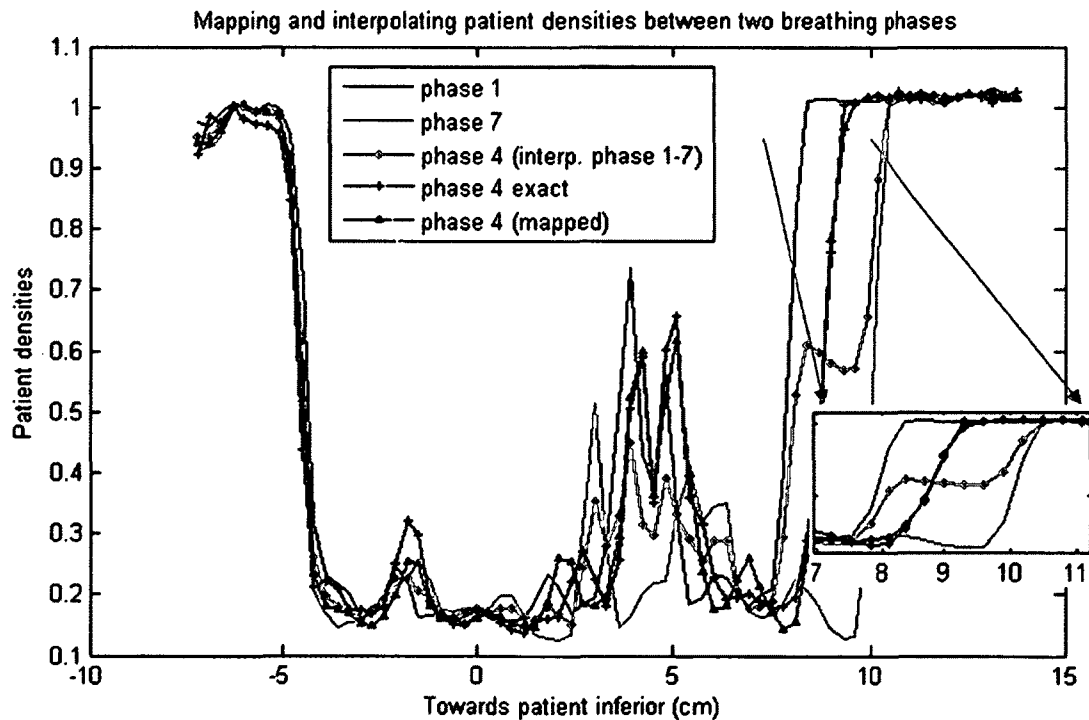
### 3.2.1.3 Density mapping

The second approach is defined as density mapping and is more appropriate for cases where the interpolation approximation fails. During the simulation, when a particle crosses a voxel boundary in the transport grid, the backward DVF at the center of the new voxel is used to find the density of the corresponding reference voxel. This density is then scaled with a volume scaling factor (VSF) to account for volume compression or dilatation. VSF is represented in figure 3.5(a) as the ratio between the area of the square voxel (right) and the deformed voxel (left). The values of VSF are calculated before the simulation for several breathing phases and are provided in an input file with the backward DVF for simulation purposes. The VSFs are calculated by deforming reference voxel shapes using forward DVFs and segmenting the deformed shapes into tetrahedra to extract the volume as proposed by Heath and Seuntjens (Heath and Seuntjens, 2006). During the simulation, using the time associated to each transported particle, the backward DVF and the VSFs are linearly interpolated between the two nearest breathing phases. Figure 3.4(c) shows an example of density mapping from the reference breathing phase to the breathing phase 4 using the DVF of breathing phase 4. The figure also shows an example where the density interpolation between breathing phase 1 and breathing phase 7 clearly fails (particularly in the diaphragm –see figure insert). This is done for demonstration purposes and the density interpolation method for this case would actually use an interpolation between breathing phase 3 and breathing phase 5. One disadvantage of the density mapping method is that the density is dependent on the accuracy of the DVF and its ability to conserve mass upon compression/dilatation.



(a)

(b)



(c)

**Figure 3.4** (a) Coronal view of patient voxelized densities. (b) The density profile for breathing phase 5.5 was interpolated between the density profile of breathing phase 5 and 6. (c) The density profile for breathing phase 4 was interpolated between the density profile of breathing phase 1 and 7. The density profile for breathing phase 4 was also mapped with deformable vector fields using the density profile of breathing phase 7 and compared with the exact density profile of breathing phase 4. (source: Paper II reproduced with permission)

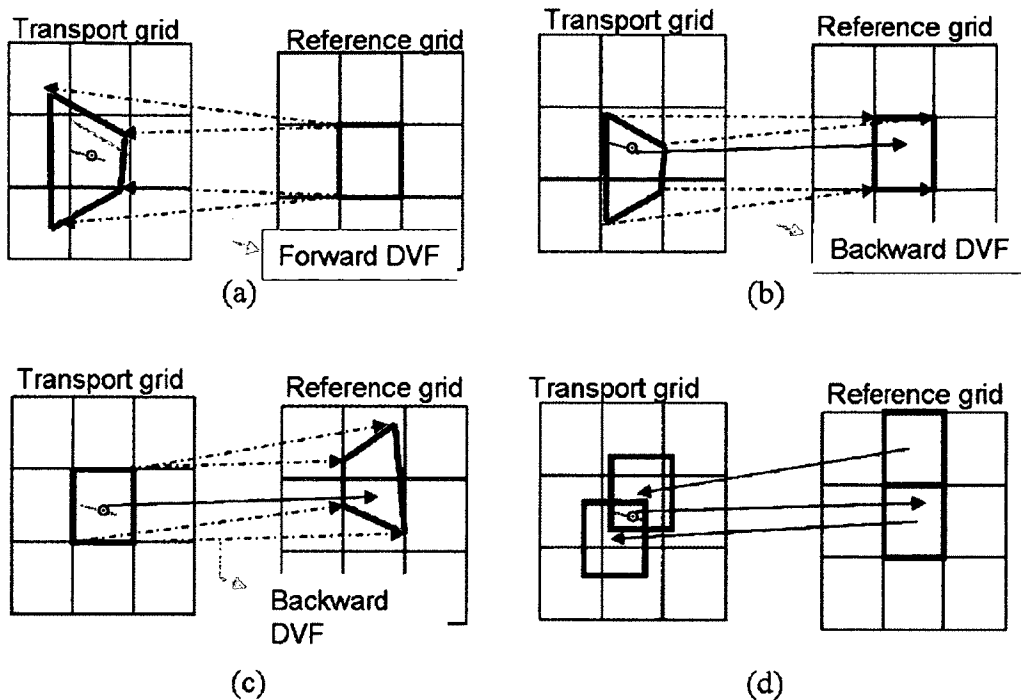


**Figure 3.5** (a) Deformed reference volume using forward deformable vector fields (DVF). The ratio between the reference grid volume and the transport grid volume is defined as the volume scaling factor (VSF). (b) Collecting volume for the reference voxel using spatially interpolated backward DVF. (c) Another view of the backward DVF as stored in the input file for Monte Carlo simulation (at the corner of each voxel). For the volume average dose mapping method, the location of the particle is randomly sampled along the deposition path and mapped back to the reference grid using a spatially interpolated backward DVF. (d) For the voxel center dose mapping method, the backward DVF is used to find the reference grid voxel. Forward DVF and non-deformed collecting volume (cubes) are used to check that energy deposition should be done in both red and green voxels. (source: Paper II reproduced with permission)

The use of non-unit VSF values is questionable in cases where the DIR algorithm is strictly based on a mean square error or other image intensity based metric with no consideration for mass conservation.

### 3.2.2 Registration of energy deposition

This section describes two methods to register the energy deposited in the time dependant transport grid to a reference grid.

### 3.2.2.1 Voxel average energy mapping

The first approach is a modification of an existing method (Zhong and Siebers, 2009) where the objective is to calculate the average dose in each reference voxel as they are deformed in other breathing phases. For each energy deposition event, the location of the particle in the rectilinear transport grid is randomly sampled along the deposition path and mapped back to the reference grid using a spatially interpolated backward deformation vector as shown in figure 3.5(b) and figure 3.5(c). The advantage of this approach compared with other methods (Heath *et al.*, 2011) is that the particle transport is performed in rectilinear geometry which allows the ability to map energy in regions of discontinuous motion (e.g., lung-chest wall interface, rotations). A drawback of the method is that it is more sensitive to DVF errors and requires correction factors (see section 3.2.2.3). The method proposed by Zhong and Siebers (Zhong and Siebers, 2009) was used in their study to calculate dose from a single deformed phase to a reference phase (e.g. from exhale to inhale). The method was extended in our study by providing backward DVFs for additional breathing phases and interpolating between nearest phases during the simulation. To avoid unnecessary interpolation of a large amount of data for each transported particle, the interpolation is done individually only for required voxels as part of the energy mapping process.

### **3.2.2.2 Voxel center energy mapping**

The second option is defined as a voxel center approach because the objective is to calculate the dose of each reference voxel center as the voxel is deformed in other breathing phases. The voxel dose calculated by MC methods in standard simulations is therefore considered here a surrogate for the point dose at the center of the voxel. This is a valid approximation for small voxel size (less than 2-3 mm) where dose variations are linear within the voxel. For each energy deposition event, the location of the particle in the transport grid is randomly sampled along the deposition path and mapped back to the reference grid using a backward DVF. However, compared with the voxel average approach defined above, the voxel shapes or collecting volume are not deformed and conserve their original size as shown in figure 3.5(d). This implies that some of the energy deposition may be mapped to none or more than one of the reference voxels. To accommodate this possibility, an extra step is required as part of the energy mapping process to check if energy deposition should also be done at neighboring reference voxels. The drawback of this method, compared to the voxel average approach, is that it requires deformation vectors in both directions to perform this check, which increases the memory requirements.

### **3.2.2.3 *Mass conservation correction factor***

As observed by (Zhong and Siebers, 2009), the voxel average approach assumes a perfect inverse consistency DVF when mapping energy from the transport grid to the reference grid. This is never exactly the case and correction factors are required to account for the

lack of mass conservation. For example, if two voxels of density  $1 \text{ g/cm}^3$  (transport grid) are mapped back to one voxel of density  $2 \text{ g/cm}^3$  (reference grid), the correction factor is unity since mass is conserved. However, if the final voxel is of density  $1.8 \text{ g/cm}^3$ , then the correction factor would be 0.9 to correct for the missing mass in the reference grid. Those correction factors may be large in a clinical lung case. For example, a small DVF error (1-2 mm) may result in energy mapped from a voxel of density  $1.2 \text{ g/cm}^3$  (bone/chest wall) to a similar size voxel of density  $0.2 \text{ g/cm}^3$  (lung), creating a dose about 6 times too high if no correction factor is used. The dose is defined in each reference voxel as mapped energy divided by mass of the reference voxel. The correction factor method used is the same regardless of whether the dose mapping or the density approach is used in the simulation. When a particle is depositing energy in the transport grid, the energy must be corrected using equation 3.1 before mapping it to the reference grid:

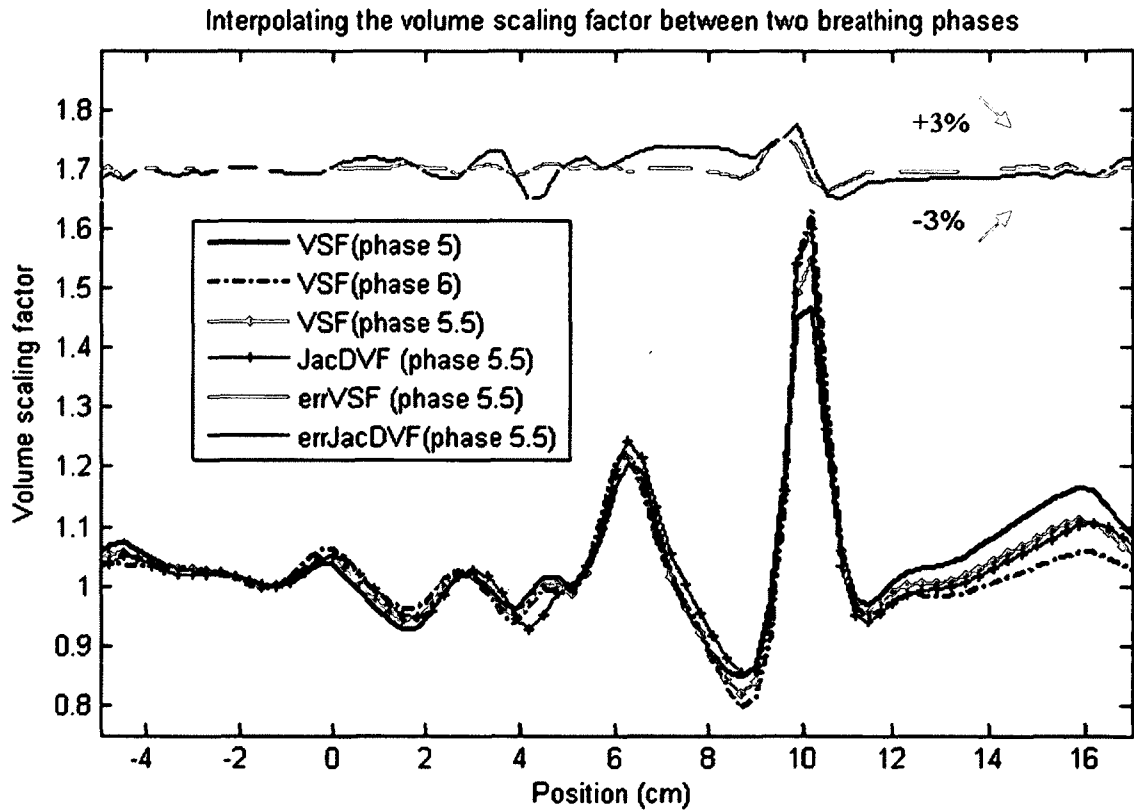
$$\text{mapped energy} \equiv \text{energy deposited} \times \frac{\rho_{\text{ref}}}{\rho_{\text{trans}}} \times \text{VSF} \quad (3.1)$$

where the factor  $\rho_{\text{ref}} / \rho_{\text{trans}}$  is a density ratio between the reference and the transport grid. In this project, our MC implementation was simplified by using water material cross-sections with electron densities for tissue characterization, which explains the absence of a mass stopping power ratio in equation (3.1). The correction performed in equation (3.1) is different than that done by (Zhong and Siebers, 2009) and it is equivalent to assuming that each reference voxel is deforming uniformly for dose mapping purposes (more information in the discussion section). The VSF factor in equation (3.1) is the same volume scaling factor as defined earlier in section 3.2.1.3 and it is set to 1 for the voxel

center dose mapping approach. This factor is fast to calculate prior to the simulation and may be interpolated exactly.

However, because the VSF is calculated with the forward DVF and the mapping is done with the backward DVF, the equation (3.1) might not be exact for non-ideal inverse consistency DIR. This uncertainty may be represented by the ratio of the deformed area shown in figure 3.5(a) and 3.5(b). Figure 3.5(a) shows the deformed reference voxel used to calculate VSF while figure 3.5(b) shows the more appropriate collecting volume for the same reference voxel. To determine the uncertainty, we calculated the ratio between the VSF and the exact value. The exact value was calculated using a point based ray tracing method similar to the one used by (Zhong and Siebers, 2009) except that we use volume instead of mass. Basically, the transport grid voxels are filled with  $N^3$  ( $N=20-40$ ) points which are then mapped to the reference grid using the DVF. This procedure is approximating the MC mapping process and the number of points scored in each reference voxel is an estimate of the exact value. The calculation times were long and the convergence was slow so we also used a faster voxel based method for clinical cases with low compression/dilatation levels. The method is similar to the one used by (Heath *et al.*, 2011) and relies on a recursive algorithm (Lasserre, 1983) to calculate the intersecting portion of voxel volumes that were previously segmented as tetrahedra. Figure 3.6 shows a VSF profile for breathing phase 5 and 6 as well as the interpolation for breathing phase 5.5. The figure also shows the ratio for this profile between the VSF and the exact value. A histogram is also used to demonstrate the range of values for the full patient coronal slice shown in figure 3.4(a). We also considered the possibility of using the determinant of the Jacobian of the DVF instead of the VSF since

the calculation is even faster. The agreement was inferior when compared with the scaling factor as shown in figure 3.6.



(d)

Figure 3.6 The volume scaling factor (VSF) profile for breathing phase 5.5 was interpolated between the VSF profile of breathing phase 5 and 6. The ratio between the VSF and the exact value is shown for the profile and a histogram shows the range of values for the full patient slice. Similar information is shown for the determinant of the Jacobian of the DVF. See figure 3.4 (a) to visualize the profile location in the patient anatomy. The peak at 6 cm is at the location of the dense tumor and that at 10 cm at the lung/diaphragm interface. (source: Paper II reproduced with permission)

### **3.2.3 Validation**

#### **3.2.3.1 Mathematical phantom**

Methods described in section 3.2.1 and 3.2.2 were implemented in the DOSXYZnrc user code. Various combinations of density and dose mapping methods were tested using simple homogeneous and heterogeneous mathematical phantoms. One example of a test is to use a mathematical phantom (10x10x10 cm<sup>3</sup> water cube, 0.25 cm voxel size) for both the transport grid and the reference grid combined with deformation vectors set to zero to check that the software maintains its original functionality. Another test is to use the same phantom combined with deformation vectors set to 1 cm in one direction to confirm that the dose profiles are shifted by the same amount. These validation tests (and others) were very similar to those already described in detail in several publications (Zhong and Siebers, 2009; Heath and Seuntjens, 2006; Siebers and Zhong, 2008; Peterhans *et al.*, 2011).

The method was also tested using more representative clinical examples for specific checks. For example, figure 3.7 (left) shows a nasopharynx clinical case treated with HT and figure 3.7 (right) shows the dose and the large variation in density along a profile. It also shows the result of a dose calculation performed with the density interpolation and the voxel center method. In this example, the same densities were used for both transport and reference grid and an artificial DVF of half the voxel size was used. This is forcing a mapping of the energy from half the volume of each neighboring voxel into one reference voxel. The figure shows the agreement between the resulting

dose (distance axis shifted back by half a voxel) and the original dose (with DVF set to zero). Due to the large variation of density from one voxel to another, this example indicates the appropriate use of the density ratio  $\rho_{\text{ref}} / \rho_{\text{trans}}$  defined in equation (3.1).

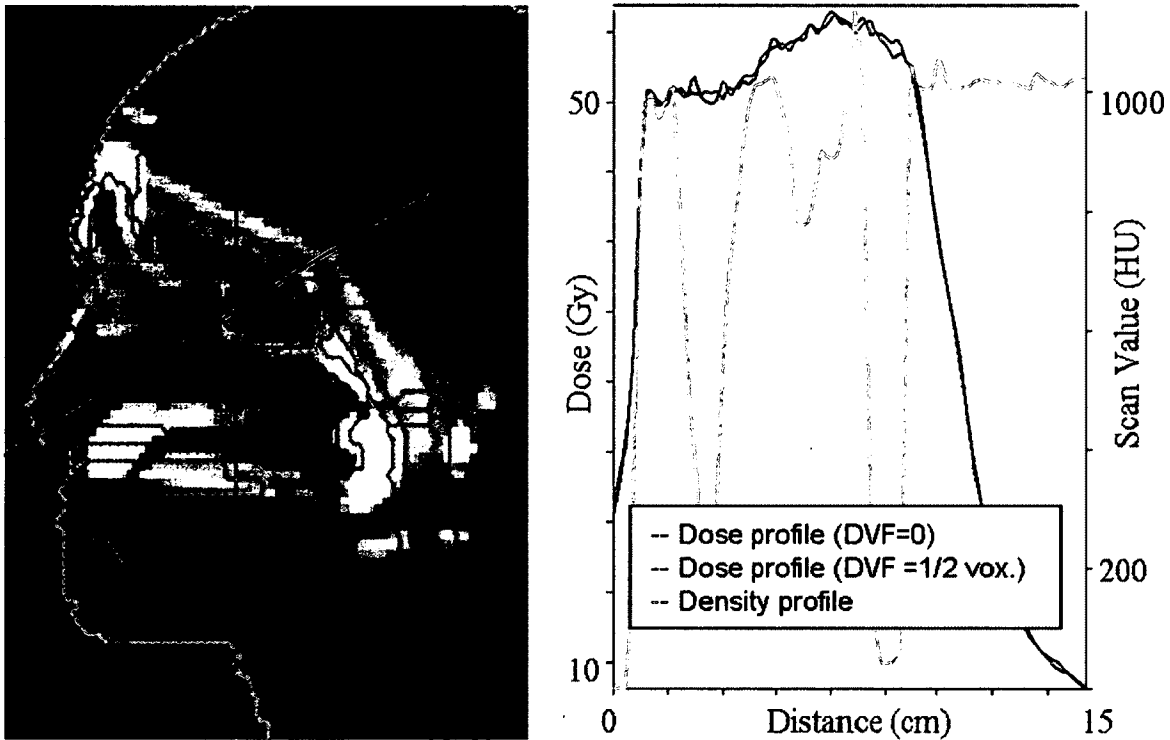


**Figure 3.7** Sagittal representation of the dose distribution and densities for a nasopharynx clinical case treated with helical tomotherapy (left). The right side shows the dose and a large variation in density along a profile. Also shown is the dose calculated with density interpolation / voxel center methods and a deformable vector field of half the voxel size to validate the appropriate use of the density ratio factor in equation 3.1. This dose profile was shifted back by half a voxel to facilitate the comparison. (source: Paper II reproduced with permission)

### 3.2.3.2 Measurements

As an additional test on the method, we measured the dose using an A1SL 0.056 cc ionization chamber located in a programmable moving phantom (QUASAR, Modus Medical Devices, London, Ontario, Canada). The setup is shown in figure 3.9(a). The phantom was first scanned and no effort was made to model the chamber explicitly in the

voxelized geometry. A single voxel was used as a surrogate for the dose in the chamber and standard TG51 correction factors were used. The phantom was then positioned on the treatment couch and the cedar insert was set to move with amplitude of 2 cm at a sinusoidal period of 3 seconds, 8 seconds and 0 seconds (no motion). While the phantom was moving, the linear accelerator (Elekta SynergyS, Elekta AB., Stockholm, Sweden) was delivering a sweeping field of 3 cm size by moving the leaves at a speed of about 11 mm/s across a distance of 4 cm (back and forth). The phantom was modified to include a positioning switch designed to convert in real time the position to electrometer reading. A large volume A17 ionization chamber was used to record transmitted dose through the MLC/jaws as a function of time. The switch position, the A17 chamber and the A1SL chamber signals were simultaneously read by a multi-channel electrometer at every 100 ms. At the same time, an iCom® listening software (provided by G. Wilson, Princess Margaret Hospital) was used to record and process data from the linear accelerator. These data are identical to that sent in real time to the record and verify system and it is more complete than standard accelerator log files for the purpose of this test. The iCom data contains machine state as a function of MU at a sampling period of about 250 ms. Absolute time in the experiment was defined as the time associated to the electrometer reading. The A17 chamber signal was later used to convert time into MU for simulation purposes. It was not possible to use the absolute time reported in the iCom data since it was found to include network related delay. The iCom data (e.g., MLC position vs. MU) were also corrected to account for known leaf calibration error based on our machine quality assurance results. A similar procedure may also be done eventually for actual

patient treatments. For example, figure 3.8 shows the gantry angle as a function of time for a test plan delivered on the machine and compared with the required gantry angle

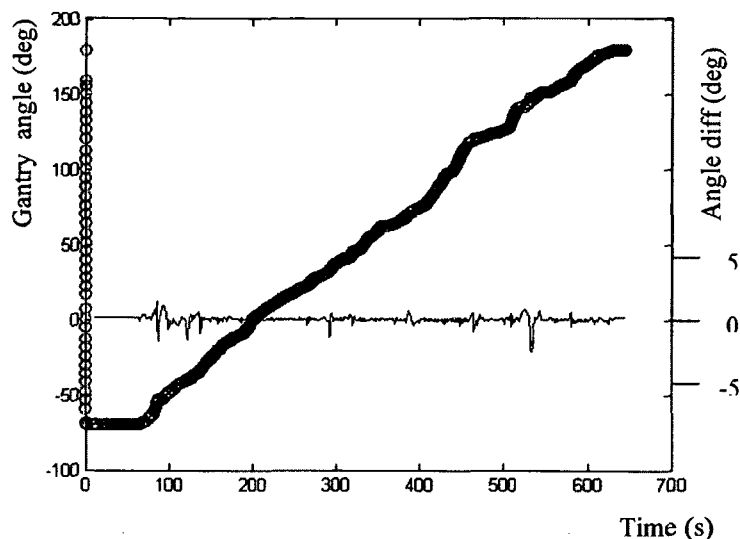
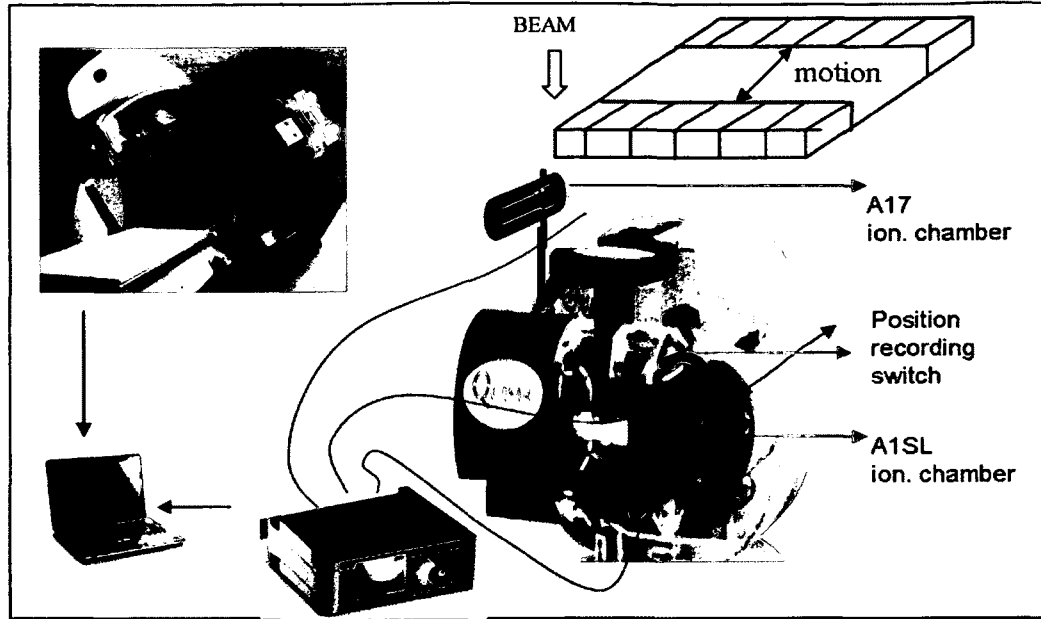
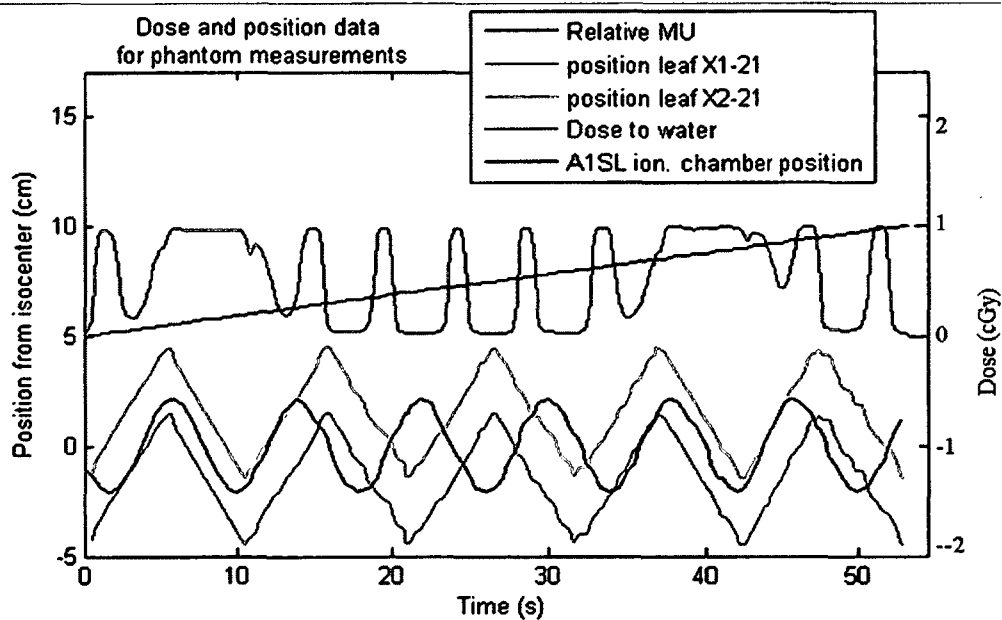


**Figure 3.8 Gantry angle vs. time for a test treatment. The recorded (iCom) gantry angle (red) and the required treatment planning system gantry angle (blue) are plotted. The difference between the two is also plotted in green. The machine allows a specified amount of error to properly adapt to rapid change in gantry speed (step function).**

based on the TPS. Figure 3.9(b) shows an example of measurement results after processing that is specific to this moving phantom study. The uncertainty of the measurement (not shown in the figure for clarity) depends on several factors. One of the most important is the electrometer time resolution of 100 ms which limits our ability to detect the time when the irradiation starts. Since the leaf speed is about 11 mm/s and the phantom speed may be as high as 8 to 21 mm/s, a 100 ms sampling time implies an error of 0.8 to 2 mm so up to 8 to 20 % when leaves are crossing the chamber (high gradient region  $\sim 10$  %/mm). This was improved greatly by using prior knowledge of beam startup features for doing more appropriate extrapolation. The A1SL ionization chamber measurements were compared with MC simulations using different combination of dose



(a)



(b)

**Figure 3.9 (a) Measurement setup that includes a programmable moving phantom and a cedar insert with an ionization chamber. The linear accelerator is delivering a sweeping field in the same direction as the phantom motion. A switch is recording the patient motion, a large volume ionization chamber is recording the transmitted dose and an iCom listening software is used to record the position of the leaves. (b) Example of measurement results after processing (phantom period is 8 seconds). The dose to water in (b) is the dose recorded by the ionization chamber per electrometer sample and it may also be interpreted as a dose rate. (source: Paper II reproduced with permission)**

mapping and density approaches. Since the phantom motion insert is rigid and the displacement is known, it was also possible to provide explicit DVFs and a 3D-CT scan in one reference breathing phase instead of using DIR with 4D-CT.

MC methods are slow and not necessarily adequate to calculate dose for a very large number of breathing patterns to search for worst cases. There are other faster but less accurate algorithms available to calculate dose in a continuously changing geometry. The expectation is that the MC method will provide a benchmark or a second order correction (heterogeneity correction, continuous motion) to those algorithms. We used this phantom measurement to test two of those faster algorithms. Those algorithms do not use heterogeneity corrections and the assumption is that the ratio of dose with motion and without motion would be correct to a first order, at least enough to provide information on the type of breathing patterns that may amplify interplay effects (resonance). The first algorithm is an in-house standard pencil beam algorithm. The pencil beam is represented as a truncated Gaussian function and the dose to the chamber was calculated by summing independent static dose calculation done at every 10 ms. The second algorithm is a point based calculation done in the beams-eye-view (BEV) coordinate system. For each planned control point, the matrix of phantom coordinates at the beginning and at the end of the control point are translated according to DVF and rotated by 3 matrices (couch, gantry, collimator) to put them in the BEV coordinate system. For each control point, a lookup table is used to find the output factor and the percent depth dose. For each active leaf pairs within the control point, the penumbra is modeled using a simple sigmoid function. The overall penumbra factor for a given control point must account for the combined motion of the leaf pair and a phantom point in the BEV coordinate system. The

motion is assumed linear within each small control point and the overall penumbra for each of the leaf boundary is approximated by equation (3.2):

$$\text{penumbra factor} \equiv 2 \ln(1 + e^{0.5d1}) - 2 \ln(1 + e^{0.5d2}) \quad (3.2)$$

where the logarithmic function is the integral of a sigmoid function and d1 and d2 are the distance between the leaf boundary and a phantom point at start/end of a control point.

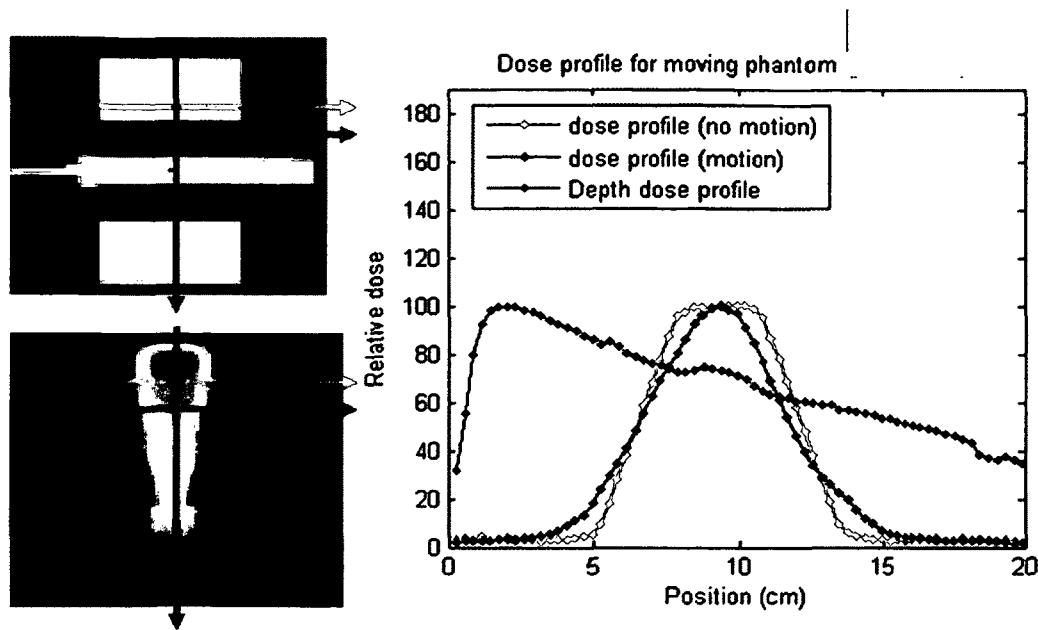
### **3.3 Results**

Figure 3.10(a) shows one example result for the phantom simulation for a motion period of 8 seconds. The dose represented is the cumulative dose so it represents the total dose received by the phantom during the measurement. Figure 3.10(a) (right) shows profiles taken in moving and non-moving parts of the phantom and the dose blurring effect of the motion. It also shows a typical depth dose profile with buildup effect at various interfaces (PMMA / cedar insert, cedar insert / chamber). The DOSXYZnrc code was modified to export not only cumulative dose but also dose at various time intervals for a subset of the reference geometry (ion chamber). Figure 3.10(b) shows the dose measurement in the chamber as a function of time. The measured data are compared with a simple pencil beam calculation and an example of MC simulation based on voxel average dose mapping and density mapping methods. The agreement is within measurement uncertainty except at 3 to 4 seconds where the Monte Carlo simulation deviates from both the pencil beam calculation and the measurements. More work is needed to understand the cause of this deviation.

### **3.4 Discussion**

Four dimensional Monte Carlo methods have been used in the past to calculate the combined impact of patient deformation and machine motion. To our knowledge, only two studies (Paganetti *et al.*, 2004; Rao *et al.*, 2012) have used dose calculation methods to incorporate deformation of the patient, full heterogeneity correction and discretized interplay effect between the machine and the patient motion. The first study by (Paganetti *et al.*, 2004) was specific to lung proton treatment and the second study was specific to lung stereotactic treatment using VMAT. In both case, the patient anatomy was modified for each discretized treatment segment (or sub-segment) in the dose calculation process by choosing one of 10 possible voxelized geometries based on the available 4D-CT images. In our study, we have presented methods (density interpolation and density mapping) to update the transport grid densities continuously as a function of time during the simulation. Similar use of DVF interpolation to map densities between two breathing phases was also used in previous studies (Heath *et al.*, 2006) to correct motion artifacts in 4D-CT. The application here is similar and allows clear improvements when compared with density interpolation as shown by figure 3.4(c) for cases where there is a large amount of motion between breathing phases. One disadvantage of the method is that the density is dependant on the accuracy of the DVF and its ability to conserve mass compression/dilatation. More work is needed to appropriately compare the uncertainties associated with each method.

We also presented methods (voxel center and voxel average) to map back the energy deposited in the time dependant transport grid to a reference grid. The use of the



(a)

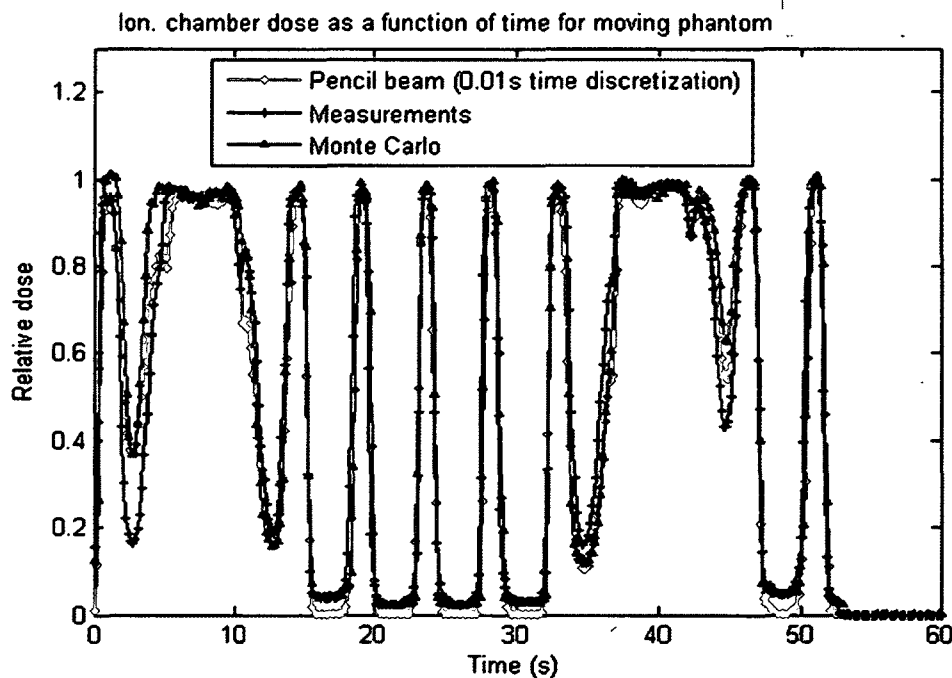
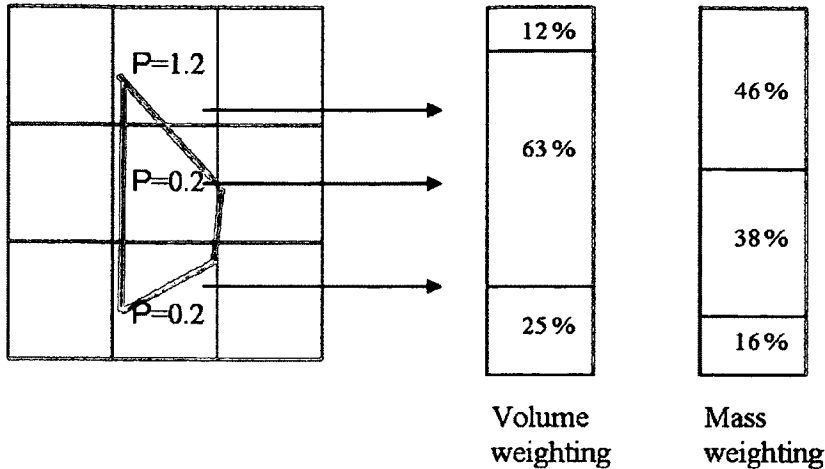


Figure 3.10 (a) Sagittal representation of the cumulative dose distribution and densities for the Monte Carlo phantom simulation (left). Dose profile in moving and non moving parts of the phantom (right). Phantom motion period was 8 seconds and density mapping / voxel average methods were used for this example of Monte Carlo simulation. (b) Dose measurement in the chamber as a function of time compared with pencil beam and Monte Carlo simulations (beams-eye-view fast algorithm is similar but not shown for clarity). Uncertainties were discussed in section 2.3.2 but not shown for clarity. (source: Paper II reproduced with permission)

voxel average or voxel center approaches are both to some degree incomplete representations of the dose received by the various cells located inside the voxels, particularly when using large voxels in regions of large dose gradient. This issue is exacerbated in the case of highly deformed voxels since it is then possible to get even larger dose variation across voxels. Both approaches converge as the voxel sizes are decreased and they provide complementary representation of the dose distribution. The voxel center method is similar in principle to a traditional dose interpolation method performed with forward DVF. The voxel average method is an extension of the method proposed by (Zhong and Siebers, 2009). As mentioned in their study, the assumption of perfect inverse consistency DVF is not exact and correction factors are required to account for the lack of mass conservation. To overcome the problem, they proposed an energy mass congruent mapping method including a correction factor (defined here as mass weighting) to scale each voxel dose in the reference grid at the end of the simulation. This correction factor is different from the correction factor used in our method (defined as volume weighting) as illustrated in figure 3.11. Volume weighting assigns equal weight to the secondary particles depositing energies in two voxels of different densities.

The choice of using a volume weighting correction factor was based on the following reasons. First, mass weighting correction factors were found to be difficult to interpolate between breathing phases due to the discontinuous nature of mapping voxels, the large values of the factors and the lack of smooth variation over small distances in



**Figure 3.11 Comparison between volume weighting and mass weighting when mapping energy deposition from the transport grid to the reference grid. In this method, the use of volume weighting assigns equal weight to the secondary particles depositing energies in two voxels of different densities. (source: Paper II reproduced with permission)**

some patient areas. Second, mass weighting is indeed in principle a better approximation as demonstrated by Zhong and Siebers (Zhong and Siebers, 2009) if we assume perfect inverse consistency DVFs and ideal voxelized geometry. However, the situation illustrated in figure 3.11 may also be caused by a small error in the DVF, particularly at a patient discontinuity when using large smoothing factors in DIR as discussed by (Heath et al. (Heath et al., 2011)). The deformed patient voxel in figure 3.11 is associated with a lung voxel located next to the chest wall. It is unlikely in reality that a lung voxel would expand in such a way as to create this very discontinuous density distribution. In this case, the mass weighting approach tends to give a too large weighting to the high density voxel, a situation that may create errors in region of high dose gradients. More work is needed to properly compare the uncertainties associated with both methods when using non ideal DVF typically obtained with existing DIR. More work is also need to address the impact of unavoidable differences between the densities used for transporting the

particles and the corrected densities used for energy mapping purposes (e.g., buildup region).

As discussed in section 3.2.2.3, the use of the VSF factor in equation 3.1 is an approximation and figure 3.6 shows the uncertainty associated with this approximation. It is assumed that a part of this error will cancel out during the simulation since this error is different for each breathing phase and it is also different at each interpolation position between two breathing phases. More work is needed to validate this assumption. We also considered using an exact value for this factor but chose not to for the following reasons. The calculation of the exact value for several breathing phases was performed and it was found that it could not be interpolated exactly due to the discontinuous nature of voxel mapping. It was also found that the level of uncertainty is similar to that of the VSF factor. It was therefore decided to keep using the VSF factor because it is much faster to calculate.

### **3.5 Conclusion**

The aim of this study was to calculate realistic dose distributions that include the continuous motion of organs and machine using 4D Monte Carlo methods. In this study, the DOSXYZnrc user code was modified to account for the continuous intra-fraction deformation of the patient geometry. We implemented in the user code two methods (density interpolation, density mapping) to update the patient geometry (transport grid densities) as a function of treatment time and two energy mapping methods (voxel average, voxel center) to map back the energy deposited in the time dependant transport

grid to a reference grid. We provided information on the measurements performed to validate the implementation of this method.

## 4 SABR lung treatment planning study

### 4.1 Introduction

SABR lung treatment for Stage 1 non-small-cell lung cancers has been shown to result in superior local control rates compared with conventionally fractionated radiotherapy (Grutters *et al.*, 2010). The use of improved techniques that may lower the treatment time and reduce the risk of late toxicities is the subject of many ongoing investigations. A challenge with many of those techniques is the difficulty of incorporating intra-fraction organ deformation in the dose calculation algorithms to generate more accurate and realistic dose distributions. As described in section 1.6.3.3, the dosimetric impact of intra-fraction organ motion for lung stereotactic treatments has been studied by several groups in the past using measurements, planning studies or a combination of both. The aim of this section is to use more accurate 4D MC methods developed in this work to calculate realistic SABR lung treatment dose distributions that include the continuous deformation of organs and motion of treatment machines for both VMAT and HT. The 4D MC method used is not really adequate to calculate dose for a very large number of breathing patterns (>1000) for each patient to investigate worst case scenarios because it is too time consuming. The expectation is also that the MC method will provide a second order correction (heterogeneity correction, continuous motion) to faster but less accurate algorithms described in section 3.2.3.2. However, as a demonstration or a feasibility study, we chose to apply the 4D MC method to a SABR lung treatment planning study of 8 patients.

## **4.2 Materials and method**

Four dimensional MC methods developed in section 2 and section 3 were applied to study more specifically the impact of intra fraction motion for small targets in the lung. Treatment plans were generated for 8 patients for 3 types of treatment techniques. For the conventional accelerator, a ~12-field 3D-CRT SABR lung treatment plan was generated using a fast multigrid convolution superposition dose calculation algorithm (XiO 5.4, Elekta CMS Inc., Maryland Heights, MO). A similar case was also planned using aperture-based inverse optimization for VMAT (Monaco 3.0.01, Elekta CMS Software Inc., Maryland Heights, MO). Monaco is based on MC dose calculation algorithm (e.g. accounts for machine continuous motion) and makes use of a virtual source model and the XVMC calculation package. HT plans were generated using inverse optimization and a 2.5 cm jaw field (Hi-Art 4.0, Tomotherapy Inc., Madison, WI). The planning modulation factor was set to 1.7 and the pitch varied from 0.144 to 0.215. The HT TPS is based on a convolution superposition algorithm that approximates the continuous gantry motion by 51 static projections per rotation. An overview of patient characteristics is found in Table 2. The location of the tumor for each patient is described in the table with three letters. The first letter (U –upper- or L –lower-) refers to the superior or inferior part of the lung. The second letter (L) refers to the pulmonary lobe. The third letter (L –left- or R –right) refers to the lung position with respect to the patient view. For example, ULR refers to the upper right pulmonary lobe. Those patients are considered representative of typical clinical cases and standard planning strategies were used to minimize the impact of patient motion. No effort was made to increase the modulation and the results are expected to reflect our clinical practice.

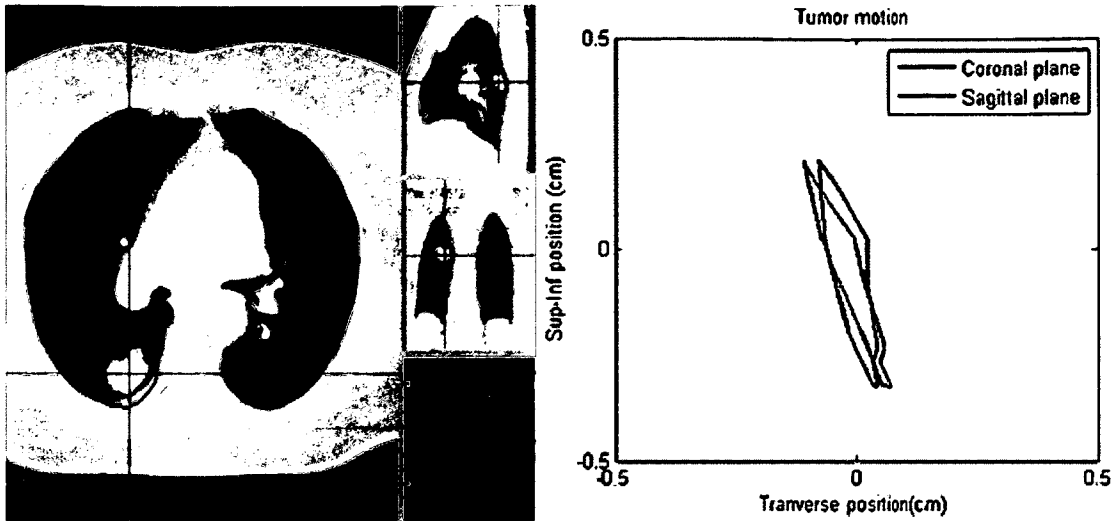
The dynamic plans (VMAT, HT) and the 4D-CT patient data were automatically processed to calculate the impact of breathing motion using MC simulation. The interface used scripts written in MATLAB partially based on modification of open source packages (Yang *et al.*, 2011a; Deasy *et al.*, 2003). The simulations were run on the Carleton University physics cluster (~600 cores). Average time for a simulation (uncertainty 1-2 %) using 150 cores was ~30 minutes. The tumor position as a function time in each breathing cycle follows the 4D-CT tumor trajectory as discussed in section 3.2.1.1. The breathing cycle was repeated and the frequency was varied from 2 to 8 seconds in steps of 0.5 seconds. Ten different starting points were used for each breathing pattern for a total of 140 breathing patterns per patient. The overall amplitude of motion ranged from 1.4 to 9.7 mm depending on the patient. All dose calculations are done with a MC method based on voxel center dose mapping and a density interpolation approach.

### **4.3 Results and Discussion**

Figure 4.1(a) shows an example of a clinical case (patient #5) with a typical target motion displayed in both coronal and sagittal planes. Figure 4.1(b) shows an example of GTV DVHs for this patient for the HT plan. The figure includes only MC calculated DVHs and shows a range of DVHs for various breathing patterns with no setup error (left) and with a setup error of 5 mm (right). This patient case was also investigated for VMAT treatment as shown in figure 4.2. These data are very representative of other clinical cases for both HT and VMAT and shows a change of the DVH of less than 2 Gy scored at 10 % and 90% of the volume.

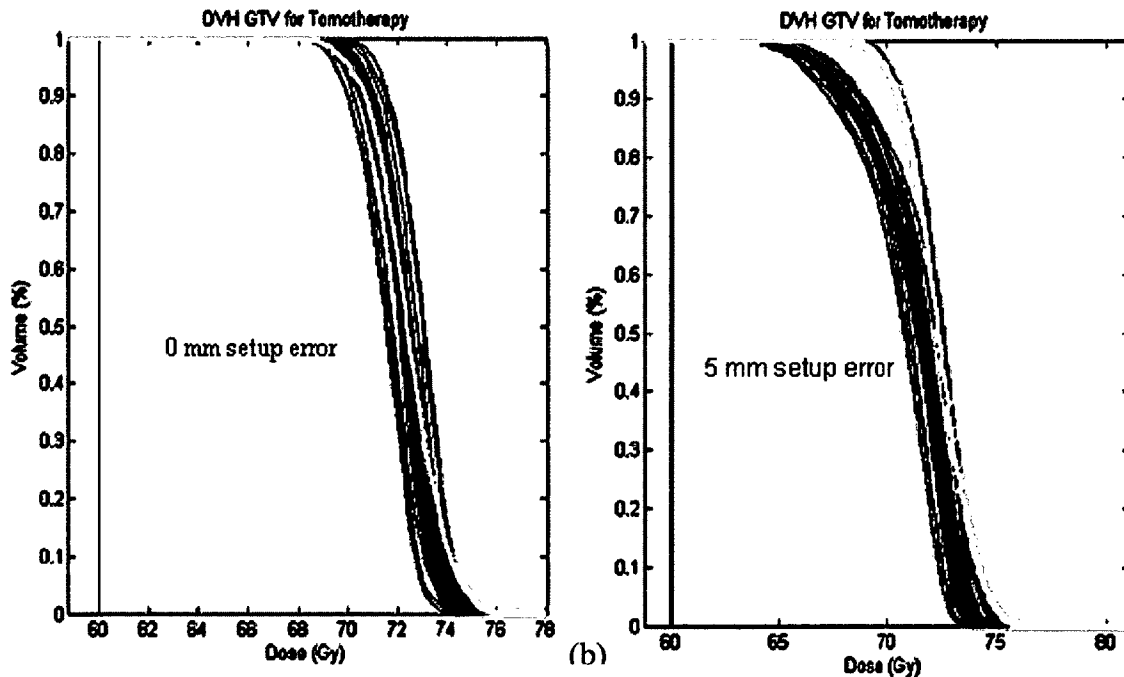
**Table 2 Overview of patient characteristics used to study the impact of intra-fraction motion in SABR lung treatments. The tumour-isocentre distance is specific to helical tomotherapy and represents the distance between the machine isocenter (center of a transverse CT image) and the location of the tumor center (GTV centroid). A larger tumor-isocentre distance increase the impact of gantry angle discretization as explained in figure 2.11. (Source: Paper II reproduced with permission)**

Patient number	Tumour density (g/cc)	Largest tumour size in patient left-right and anterior-posterior directions (cm)	Maximum motion for a GTV voxel (mm)	Tumour position (cm)	Total Dose/ fractions (Gy/fx)	Tumour- iso distance (cm)
1	0.68	1.4 x 2.2	5.1	LLR	60/5	8.9
2	0.42	1.2 x 3.0	2.7	ULL	54/3	10.0
3	0.58	1.5 x 3.3	2.1	ULL	60/5	5.5
4	0.98	1.0 x 1.2	9.7	LLL	54/3	8.9
5	0.49	2.7 x 3.0	5.7	LLR	60/5	7.5
6	0.88	1.8 x 2.4	1.4	ULR	54/3	4.7
7	0.82	2.3 x 3.0	7.6	LLR	60/5	10.5
8	0.81	2.3 x 1.9	4.7	LLR	54/3	9.3



(a)

- Dose prescription
- Expiration scan (no tumor motion)
- Free breathing scan (no tumor motion, continuous gantry)
- Free breathing scan (no tumor motion, discrete gantry)
- Interplay effect



(b)

Figure 4.1 (a) Example of patient treated with a lung stereotactic treatment (patient #5) with a typical tumour motion displayed in both coronal and sagittal planes. (b) GTV dose volume histogram for helical tomotherapy plan simulations using various breathing patterns (blue) with (right) and without (left) a 5 mm setup error. Monte Carlo simulations were done using density interpolation / voxel center methods. Simulations were also performed with no breathing motion on the free breathing and the exhale patient geometries (red) for comparison purposes. The free breathing simulations were performed with both continuous (green) and discrete (yellow – Tomotherapy only-) gantry motion. The free breathing simulations in the right figure do not include the setup error to facilitate the appreciation of the changes caused by the setup error. (Source: Paper II rep. with permission)

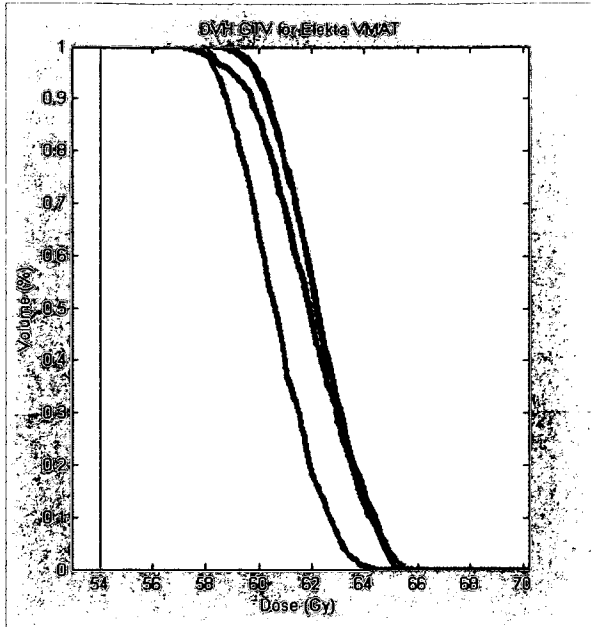


Figure 4.2 Example of patient treated with a lung stereotactic treatment (patient #5) using VMAT. Monte Carlo simulations were also performed with no breathing motion on the free breathing (green) and the exhale patient geometries (red) for comparison purposes.

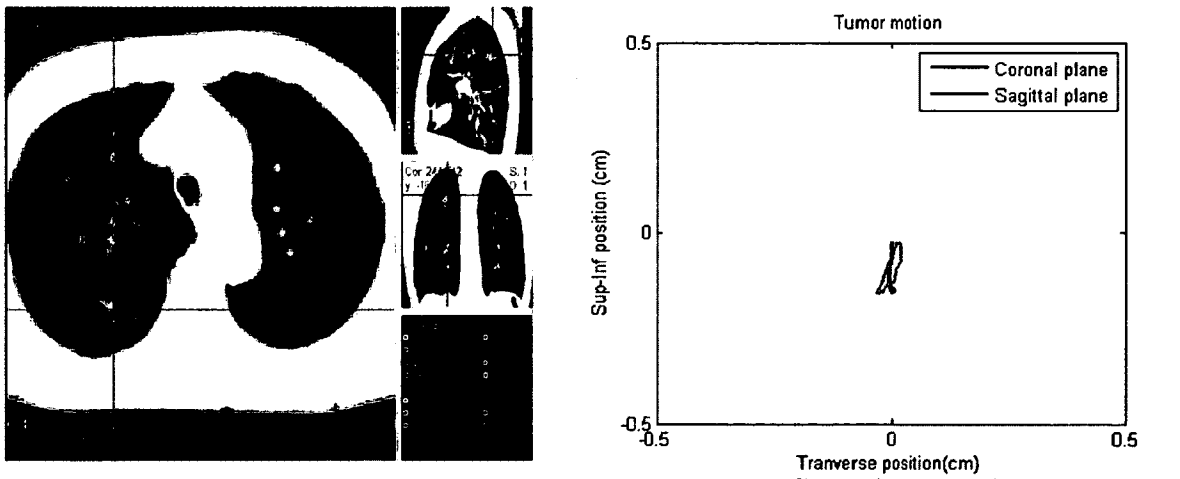


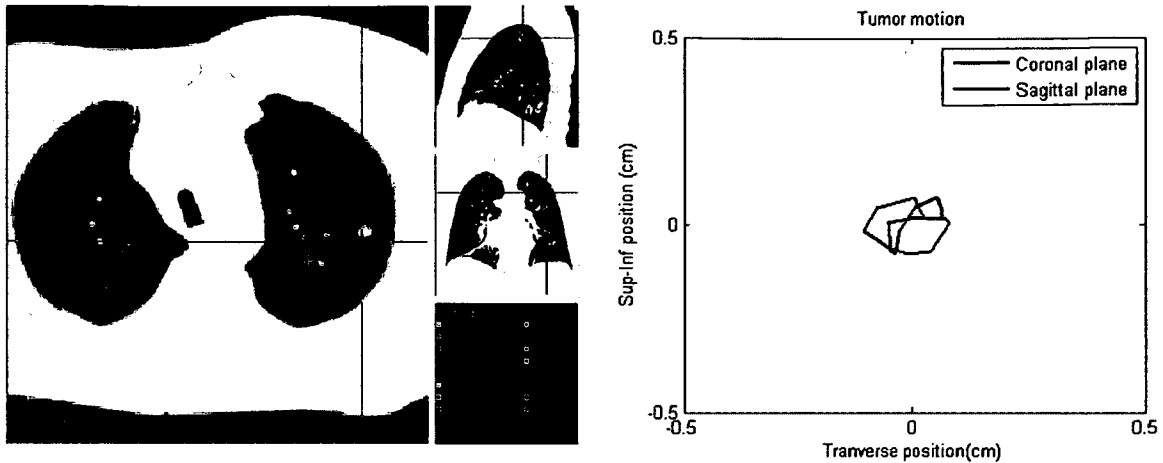
Figure 4.3 (a) View of the lung anatomy and target contours (left) for patient #6 treated with a stereotactic lung treatment. Tumour motion is displayed (right) in both coronal and sagittal planes.

For one of the patients (patient #6), it was decided to not perform the MC simulation since the amount of tumour motion was too small (see figure 4.3). Similar information (patient anatomy, contours, motion amplitude, dose volume histogram) is also shown for several patients in figures 4.4 to 4.8. For patient #8, a second tumour was artificially created in the contralateral lung (left lung) in an attempt to introduce a different pattern of intensity modulation and report the impact on the first tumour. For this case, a combined double tumour HT treatment plan was optimized and the resulting change in the MLC sinogram and the dose volume histogram are shown in figure 4.9. The increase plan complexity did not increase the amount of interplay effect.

#### ***4.4 Discussion and conclusion***

The aim of this study was to calculate realistic dose distributions that include the continuous motion of organs and treatment machine using 4D MC methods for both VMAT and HT SABR lung treatments. The results shown are restricted to the tumour because the validation of the result of deformable image registration for other organ is still in progress. The results shown in this section are all based on Monte Carlo calculations to have a consistent comparison between dose distributions calculated with and without patient motion. A full comparison between the clinical treatment planning systems and our MC dose calculations and an assessment of the different treatment modalities comparative advantages is ongoing.

The 4D Monte Carlo method used in this work is based on EGSnrc user codes which are known to be less efficient than several other proprietary codes. However, they are freely available, open source, flexible, well benchmarked for a large range of materials and



- Dose prescription
- Expiration scan (no tumor motion)
- Free breathing scan (no tumor motion, continuous gantry)
- Free breathing scan (no tumor motion, discrete gantry)
- Interplay effect

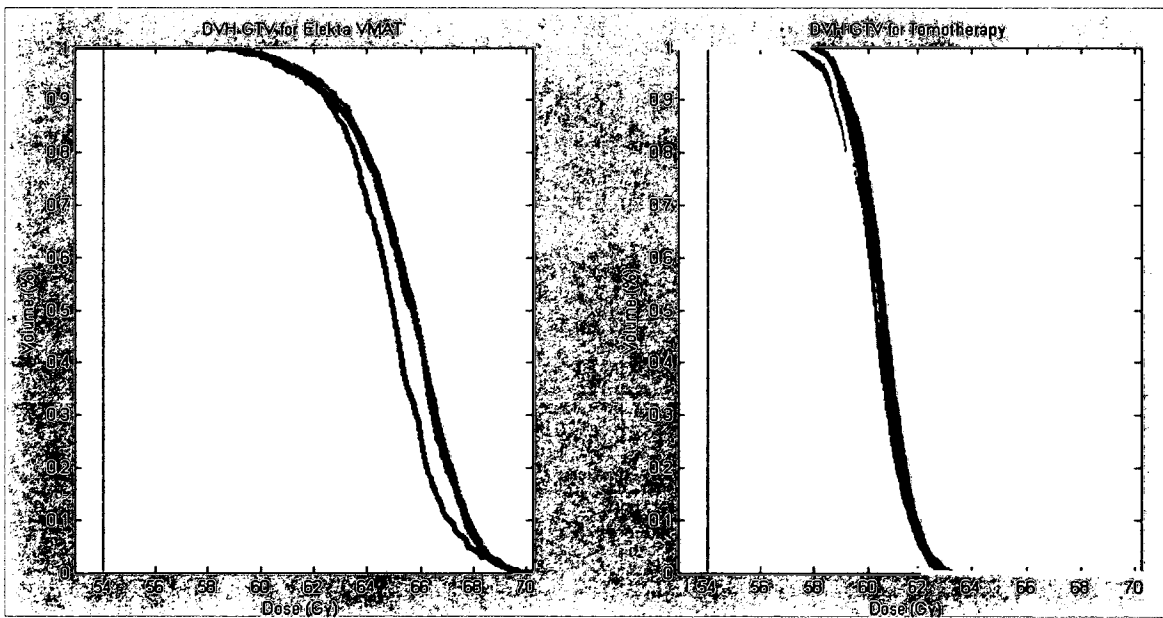
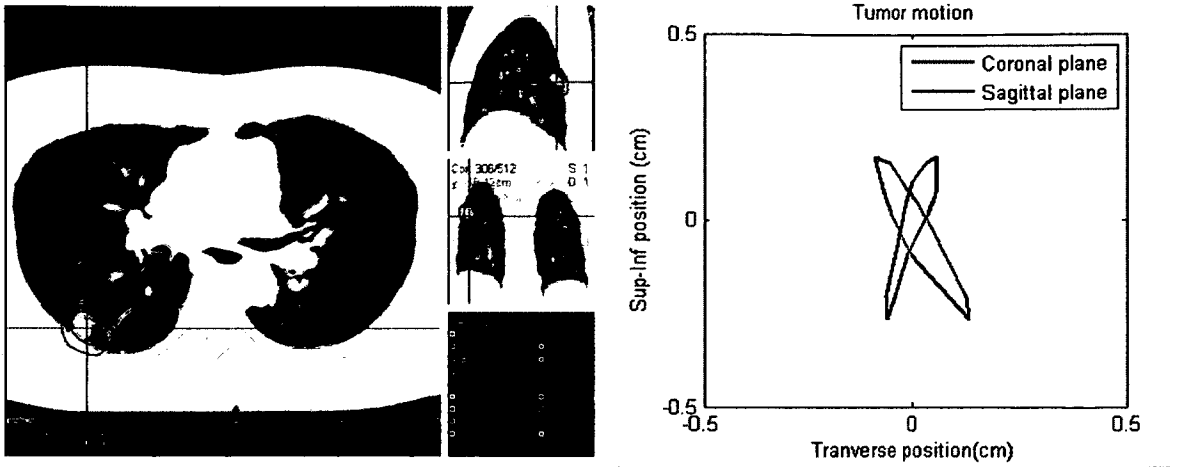
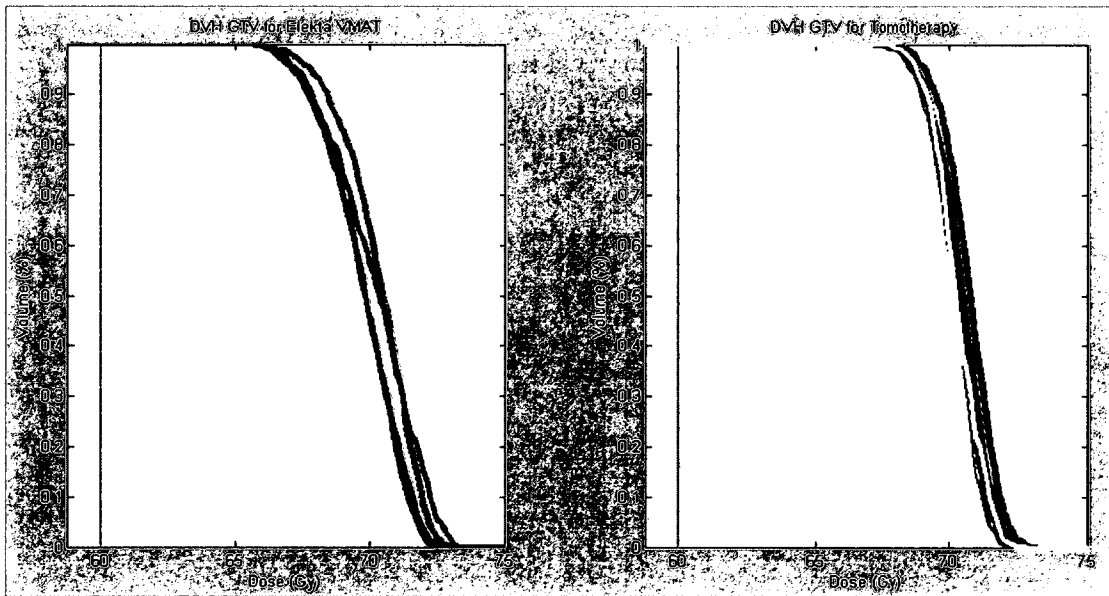


Figure 4.4 (a) View of the lung anatomy and target contours (left) for patient #2 treated with a SABR lung treatment. Tumour motion is displayed (right) in both coronal and sagittal planes. (b) GTV dose volume histogram for VMAT (left) and helical tomotherapy (right) 4D MC simulations using various breathing patterns. Simulations were also performed with no breathing motion on the free breathing and the exhale patient geometries (red) for comparison purposes. The free breathing simulations were performed with both continuous (green) and discrete (yellow) gantry motion.



- Dose prescription
- Expiration scan (no tumor motion)
- Free breathing scan (no tumor motion, continuous gantry)
- Free breathing scan (no tumor motion, discrete gantry)
- Interplay effect



**Figure 4.5 (a)** View of the lung anatomy and target contours (left) for patient #1 treated with a SABR lung treatment. Tumour motion is displayed (right), in both coronal and sagittal planes. **(b)** GTV dose volume histogram for VMAT (left) and helical tomotherapy (right) 4D MC simulations using various breathing patterns. Simulations were also performed with no breathing motion on the free breathing and the exhale patient geometries (red) for comparison purposes. The free breathing simulations were performed with both continuous (green) and discrete (yellow) gantry motion.

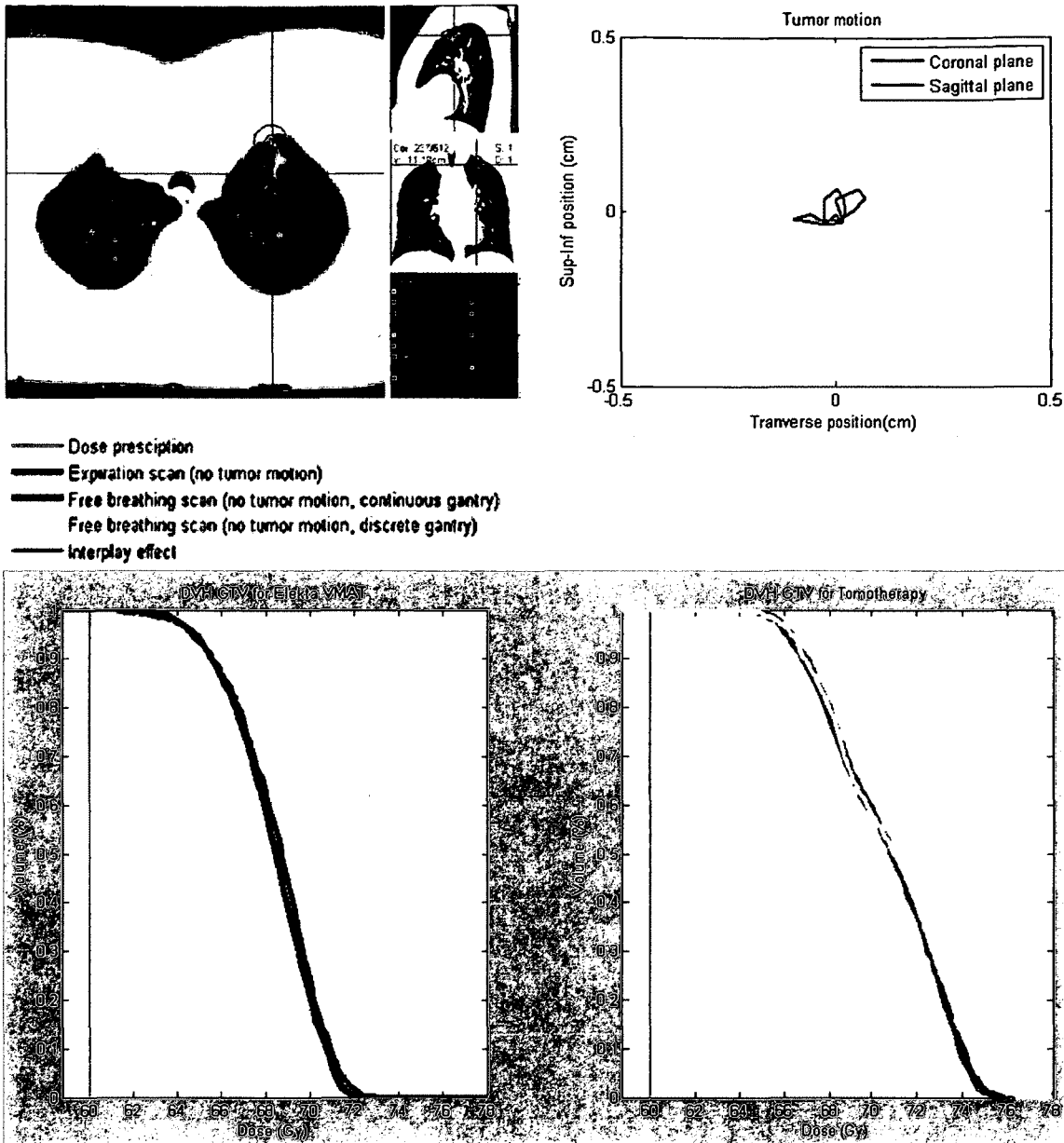


**Figure 4.6 (a)** View of the lung anatomy and target contours (left) for patient #3 treated with a SABR lung treatment. Tumour motion is displayed (right), in both coronal and sagittal planes. **(b)** GTV dose volume histogram for VMAT (left) and helical tomotherapy (right) 4D MC simulations using various breathing patterns. Simulations were also performed with no breathing motion on the free breathing and the exhale patient geometries (red) for comparison purposes. The free breathing simulations were performed with both continuous (green) and discrete (yellow) gantry motion.

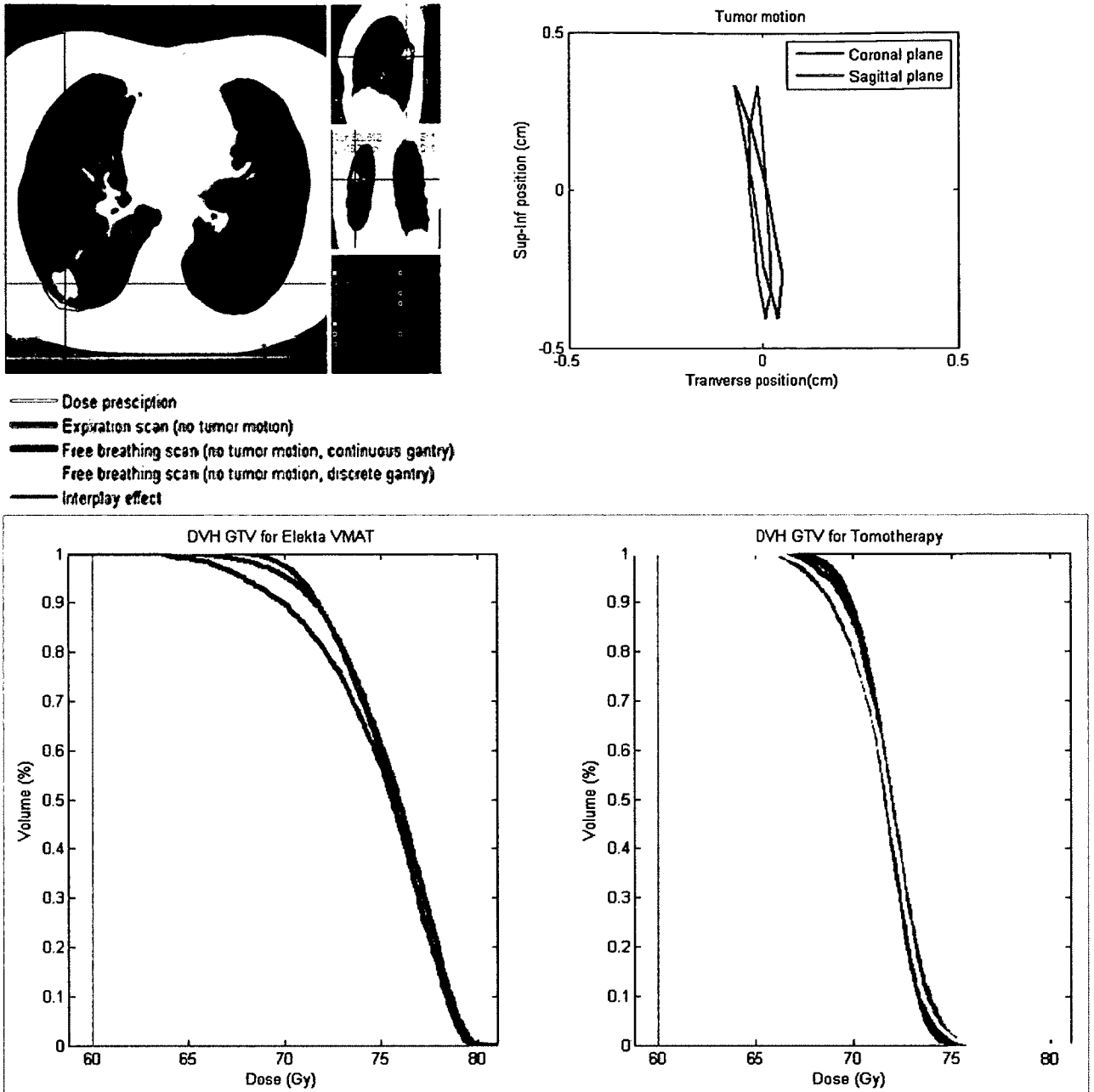
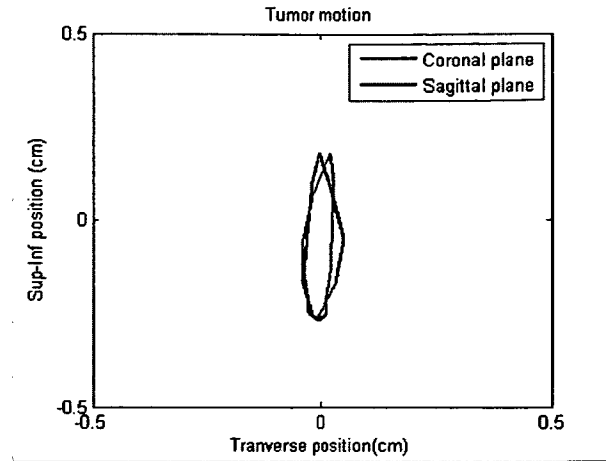
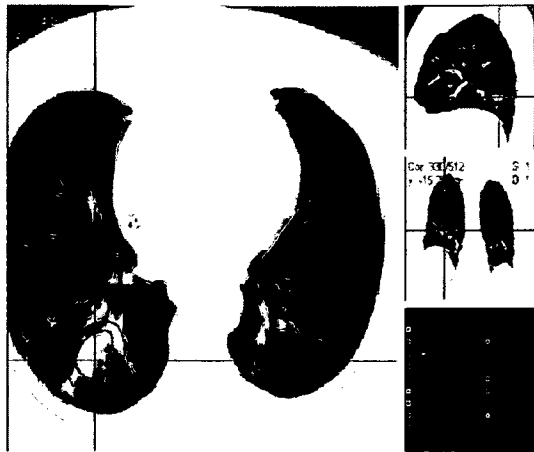


**Figure 4.7 (a)** View of the lung anatomy and target contours (left) for patient #7 treated with a SABR lung treatment. Tumour motion is displayed (right), in both coronal and sagittal planes. **(b)** GTV dose volume histogram for VMAT (left) and helical tomotherapy (right) 4D MC simulations using various breathing patterns. Simulations were also performed with no breathing motion on the free breathing and the exhale patient geometries (red) for comparison purposes. The free breathing simulations were performed with both continuous (green) and discrete (yellow) gantry motion.



- Dose prescription
- Expiration scan (no tumor motion)
- Free breathing scan (no tumor motion, continuous gantry)
- Free breathing scan (no tumor motion, discrete gantry)
- Interplay effect

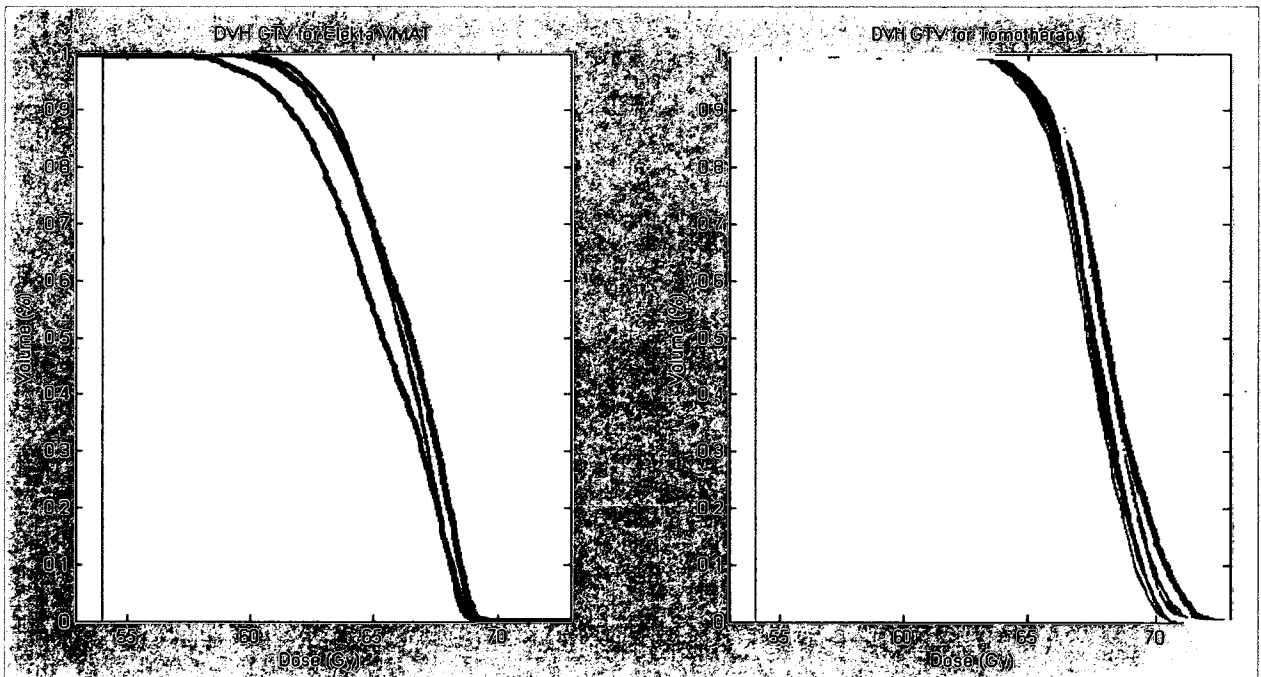
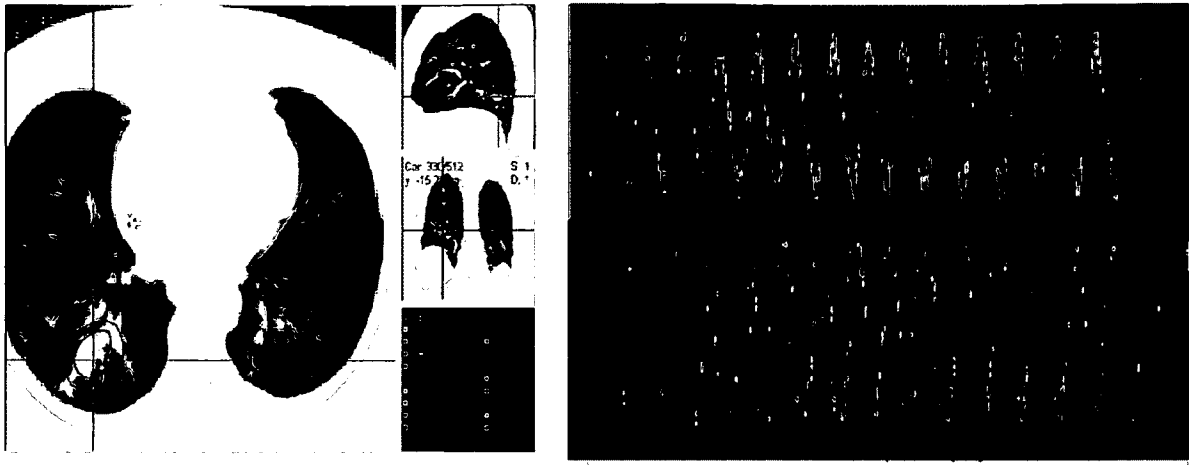


**Figure 4.8 (a)** View of the lung anatomy and target contours (left) for patient #8 treated with a SABR lung treatment. Tumour motion is displayed (right), in both coronal and sagittal planes. **(b)** GTV dose volume histogram for VMAT (left) and helical tomotherapy (right) 4D MC simulations using various breathing patterns. Simulations were also performed with no breathing motion on the free breathing and the exhale patient geometries (red) for comparison purposes. The free breathing simulations were performed with both continuous (green) and discrete (yellow) gantry motion.



- Dose prescription
- Expiration scan (no tumor motion)
- Free breathing scan (no tumor motion, continuous gantry)
- Free breathing scan (no tumor motion, discrete gantry)
- Interplay effect

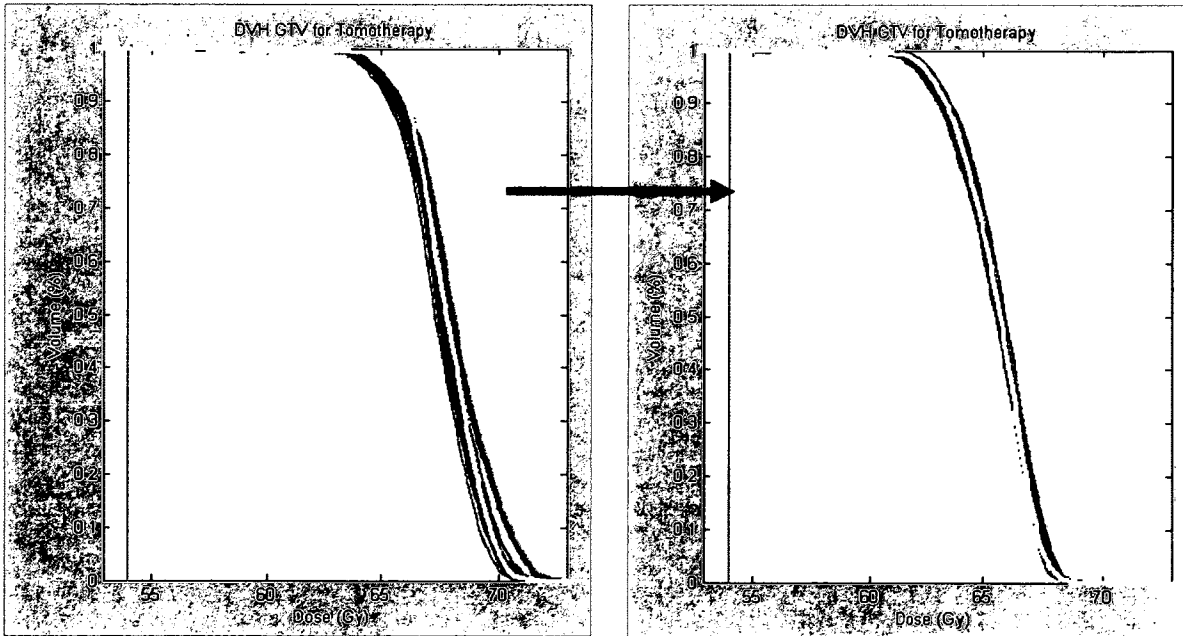


**Figure 4.9 (a)** View of the lung anatomy and target contours (left) for patient #8 treated with a SABR lung treatment. A second tumour was artificially created in the left lung to maximize the treatment impact on the first tumour. A combined double tumour HT treatment plan was optimized. The resulting change in the MLC sinogram – from top to bottom - and the dose volume histogram are shown.

energies, and the speed is suitable for research purposes. The 4D MC method presented in this study is not adequate to calculate dose for a very large number of breathing patterns (>1000) to search for worst cases since a typical simulation takes about 30 minutes with 150 cores. The methods introduced in this study are making the overall calculation time (from the electron impinging on the target to the patient dose) slower by about 30%. The expectation is that the MC method will provide a benchmark or a second order correction (heterogeneity correction, continuous motion) to faster but less accurate algorithms as described in section 2.3.2. However, as a demonstration, we applied the method to an SBRT planning study of 8 patients. Four dimensional MC was used to confirm that breathing motion is properly addressed with the ITV method for the range of breathing patterns tested. We also tested one more patient treated simultaneously for two SABR treatments and the results were similar. This confirms the results of other studies (Ong et al., 2011; Court et al., 2010; Rao et al., 2012; Kissick et al., 2008; Kim et al., 2009) about the safety of commonly used planning strategies to account for tumour motion.

More work is needed to properly distinguish the actual motion interplay effect from the effect of dose heterogeneity in the target, a situation that may also be captured approximately using dose convolution methods or by simply changing the isocenter position. Four dimensional MC methods may be useful in cases where the tumour is located next to a bone structure (as shown in figure 4.1) and where the modulated fluence is used to compensate the increase in density at the periphery of the target. In this case, 4D MC allows combination of the convoluted contribution of setup error and time dependant heterogeneity correction caused by patient and machine motion. More work is

also needed to extend this study to more challenging techniques where the interplay effect might have a bigger role (e.g., HT with dynamic jaws and couch, robotic tracking of irregular target without using rotation). Such techniques may reduce treatment time or increase treatment plan quality at the expense of a larger risk of getting dose deviation due to the interplay effect. Those results combined with the measurements discussed in section 3.3 also represent a first step to quantify parameters to be used to calculate dose for each patient treatment for adaptive purposes.

## 5 Summary

The aim of this study was to calculate for the first time realistic dose distributions that include the continuous motion of organs and treatment machines using 4D MC methods for both VMAT and HT SABR lung treatments.

In chapter 2, we presented a method to perform position-probability-sampled MC dose calculations in the BEAMnrc and DOSXZYNrc user codes of EGSnrc. The method includes full accelerator head simulation of a conventional and HT treatment units and a realistic representation of machine continuous motion via the sampling of a time variable. The method simplifies the simulation process, improves the dose calculation accuracy and involves an acceptably small change in computation time. Absolute dose agreement for static fields between MC calculations and measurements is within 2 % / 1 mm. Absolute dose agreement between MC and TPS for four types of treatment techniques was determined to be within 3 % / 3 mm. As shown for a brain case, a TMI case and as observed for many other clinical cases retrospectively, the effect of using discretized machine motion in commercial treatment planning system is clinically negligible for most clinical cases. However, for specific helical tomotherapy treatment plans when this may not be the case (small tumor size, large off-axis tumor position, low modulation factor), the impact on the dose distribution should be analyzed carefully in an appropriate plane as part of the plan quality assurance process. The MC method implemented as part of this project is therefore a valuable tool to extend the quality assurance process done with measurements to the full 3D patient geometry and to incorporate at the same time the additional impact of tissue heterogeneities and patient motion. As an example, an helical tomotherapy clinical case was provided in this study where the MC simulation

and the measurements had dose differences well above 10 % / 5 mm near the edge of the PTV when compared with the commercial treatment planning system..

In chapter 3, the DOSXYZnrc user code was modified to account for the first time for the continuous intra-fraction deformation of the patient geometry using 4D MC methods. We implemented in the user code two methods (density interpolation, density mapping) to update the patient geometry (transport grid densities) as a function of time and two methods (voxel average, voxel center) to map back the energy deposited in the time dependant transport grid to a reference grid. We then derived correction factors to account for non-ideal deformable vector field inverse consistency and mass conservation. Finally, we provided information on the measurements performed to validate the implementation of this method. Those measurements also represent a first step to quantify parameters to be used to calculate dose for each patient treatment for adaptive purposes. The 4D MC methods developed in this work may be useful in clinical cases where the tumour is located next to a bone structure and where the modulated fluence is used to compensate the increase in density at the periphery of the target. In this case, 4D MC allows combination of the convoluted contribution of setup error and time dependant heterogeneity correction caused by patient and machine motion. The method could also be used to study more challenging techniques where the interplay effect might have a bigger role (e.g., HT with dynamic jaws and couch, robotic tracking of irregular target without using rotation, using smaller planning target volume margin for cases where the tumor is located very close to a radiosensitive organ).

In chapter 4, we presented an example of application of the method for lung stereotactic treatments with intra-fraction motion. The results showed that breathing

motion is properly addressed with the ITV method for the case studied. For both HT and VMAT SABR lung treatments, the impact of interplay effect is a change of the target DVH of less than 2 Gy scored at 10 % and 90% of the volume.

## 6 References

- Adler J R, Jr., Chang S D, Murphy M J, Doty J, Geis P and Hancock S L 1997 The Cyberknife: a frameless robotic system for radiosurgery *Stereotact Funct Neurosurg* 69 124-8
- Agostinelli S 2003 GEANT4—a simulation toolkit *Nucl. Instrum. Methods Phys* 506
- Ahnesjo A 1989 Collapsed cone convolution of radiant energy for photon dose calculation in heterogeneous media *Med Phys* 16 577-92
- Ahnesjo A and Aspradakis M M 1999 Dose calculations for external photon beams in radiotherapy *Phys Med Biol* 44 R99-155
- Ahunbay E and Li X A 2007 Investigation of the reliability, accuracy, and efficiency of gated IMRT delivery with a commercial linear accelerator *Med Phys* 34 2928-38
- Al-Mayah A, Moseley J, Velec M, Hunter S and Brock K 2010 Deformable image registration of heterogeneous human lung incorporating the bronchial tree *Med Phys* 37 4560-71
- Balog J, Olivera G and Kapatoes J 2003 Clinical helical tomotherapy commissioning dosimetry *Med Phys* 30 3097-106
- Balog J P, Mackie T R, Wenman D L, Glass M, Fang G and Pearson D 1999 Multileaf collimator interleaf transmission *Med Phys* 26 176-86
- Balter J M, Pelizzari C A and Chen G T 1992 Correlation of projection radiographs in radiation therapy using open curve segments and points *Med Phys* 19 329-34
- Balter J M, Ten Haken R K, Lawrence T S, Lam K L and Robertson J M 1996 Uncertainties in CT-based radiation therapy treatment planning associated with patient breathing *Int J Radiat Oncol Biol Phys* 36 167-74
- Beddar A S, Mason D J and O'Brien P F 1994 Absorbed dose perturbation caused by diodes for small field photon dosimetry *Med Phys* 21 1075-9
- Berger M J, Coursey J S, Zucker M A and J. C 2012a Stopping-Power and Range Tables for Electrons, Protons, and Helium Ions <http://www.nist.gov/pml/data/star/index.cfm>
- Berger M J, Hubbell J H, Seltzer S M, Chang J, Coursey J S, Sukumar R, Zucker D S and Olsen K 2012b XCOM: Photon Cross Section Database (version 1.5) <http://physics.nist.gov/xcom>
- Berlinger K, Sauer O, Vences L and Roth M 2006 A simple method for labeling CT images with respiratory states *Med Phys* 33 3144-8
- Bielajew A F 1995 HOWFAR and HOWNEAR: Geometry Modeling for Monte Carlo Particle Transport *NRCC Reports PIRS-0341*
- Bissonnette J P, Balter P A, Dong L, Langen K M, Lovelock D M, Miften M, Moseley D J, Pouliot J, Sonke J J and Yoo S 2012 Quality assurance for image-guided radiation therapy utilizing CT-based technologies: A report of the AAPM TG-179 *Med Phys* 39 1946-63
- Bortfeld T, Jiang S B and Rietzel E 2004 Effects of motion on the total dose distribution *Semin Radiat Oncol* 14 41-51
- Bortfeld T, Jokivarsi K, Goitein M, Kung J and Jiang S B 2002 Effects of intra-fraction motion on IMRT dose delivery: statistical analysis and simulation *Phys Med Biol* 47 2203-20
- Boyer A L and Li S 1997 Geometric analysis of light-field position of a multileaf collimator with curved ends *Med Phys* 24 757-62
- Bradley J D, Nofal A N, El Naqa I M, Lu W, Liu J, Hubenschmidt J, Low D A, Drzymala R E and Khullar D 2006 Comparison of helical, maximum intensity projection (MIP), and averaged intensity (AI) 4D CT imaging for stereotactic body radiation therapy (SBRT) planning in lung cancer *Radiother Oncol* 81 264-8
- Briesmeister J F 2000 MCNP—A general Monte Carlo N-Particle Transport Code, Version 4C *Technical report No LA-13709 Los Alamos National Laboratory*
- Brock K K 2010 Results of a multi-institution deformable registration accuracy study (MIDRAS) *Int J Radiat Oncol Biol Phys* 76 583-96
- Brock K K, Sharpe M B, Dawson L A, Kim S M and Jaffray D A 2005 Accuracy of finite element model-based multi-organ deformable image registration *Med Phys* 32 1647-59
- Brock K M, Balter J M, Dawson L A, Kessler M L and Meyer C R 2003 Automated generation of a four-dimensional model of the liver using warping and mutual information *Med Phys* 30 1128-33

- Brown W T, Wu X, Amendola B, Perman M, Han H, Fayad F, Garcia S, Lewin A, Abitbol A, de la Zerda A and Schwade J G 2007a Treatment of early non-small cell lung cancer, stage IA, by image-guided robotic stereotactic radioablation--CyberKnife *Cancer J* 13 87-94
- Brown W T, Wu X, Fayad F, Fowler J F, Amendola B E, Garcia S, Han H, de la Zerda A, Bossart E, Huang Z and Schwade J G 2007b CyberKnife radiosurgery for stage I lung cancer: results at 36 months *Clin Lung Cancer* 8 488-92
- Brown W T, Wu X, Wen B C, Fowler J F, Fayad F, Amendola B E, Garcia S, De La Zerda A, Huang Z and Schwade J G 2007c Early results of CyberKnife image-guided robotic stereotactic radiosurgery for treatment of lung tumours *Comput Aided Surg* 12 253-61
- Bush K, Townson R and Zavgorodni S 2008 Monte Carlo simulation of RapidArc radiotherapy delivery *Phys Med Biol* 53 N359-70
- Chang S D, Main W, Martin D P, Gibbs I C and Heilbrun M P 2003 An analysis of the accuracy of the CyberKnife: a robotic frameless stereotactic radiosurgical system *Neurosurgery* 52 140-6; discussion 6-7
- Chen Q, Chen M and Lu W 2011 Ultrafast convolution/superposition using tabulated and exponential kernels on GPU *Med Phys* 38 1150-61
- Chetty I J, Rosu M, McShan D L, Fraass B A, Balter J M and Ten Haken R K 2004 Accounting for center-of-mass target motion using convolution methods in Monte Carlo-based dose calculations of the lung *Med Phys* 31 925-32
- Chi A, Jang S Y, Welsh J S, Nguyen N P, Ong E, Gobar L and Komaki R 2011 Feasibility of helical tomotherapy in stereotactic body radiation therapy for centrally located early stage nonsmall-cell lung cancer or lung metastases *Int J Radiat Oncol Biol Phys* 81 856-62
- Chi A, Liao Z, Nguyen N P, Xu J, Welsh J S, Jang S Y, Howe C and Komaki R 2012 Dosimetric selection for helical tomotherapy based stereotactic ablative radiotherapy for early-stage non-small cell lung cancer or lung metastases *PLoS One* 7 e35809
- Chow J C, Wong E, Chen J Z and Van Dyk J 2003 Comparison of dose calculation algorithms with Monte Carlo methods for photon arcs *Med Phys* 30 2686-94
- Christensen G E, Rabbitt R D and Miller M I 1994 3D brain mapping using a deformable neuroanatomy *Phys Med Biol* 39 609-18
- Court L E, Seco J, Lu X Q, Ebe K, Mayo C, Ionascu D, Winey B, Giakoumakis N, Aristophanous M, Berbeco R, Rottman J, Bogdanov M, Schofield D and Lingos T 2010 Use of a realistic breathing lung phantom to evaluate dose delivery errors *Med Phys* 37 5850-7
- Curry III T S, Dowdey J E and Murphy JR R C 1990 Christensen's Physics of Diagnostic Radiology (fourth edition) *Lippincott Williams & Wilkins*
- De Vlaminck K, Palmans H, Verhaegen F, De Wagter C, De Neve W and Thierens H 1999 Dose measurements compared with Monte Carlo simulations of narrow 6 MV multileaf collimator shaped photon beams *Med Phys* 26 1874-82
- Deasy J O, Blanco A I and Clark V H 2003 CERR: a computational environment for radiotherapy research *Med Phys* 30 979-85
- Duan J, Shen S, Fiveash J B, Popple R A and Brezovich I A 2006 Dosimetric and radiobiological impact of dose fractionation on respiratory motion induced IMRT delivery errors: a volumetric dose measurement study *Med Phys* 33 1380-7
- Dunlap N, McIntosh A, Sheng K, Yang W, Turner B, Shoushtari A, Sheehan J, Jones D R, Lu W, Ruchala K, Olivera G, Parnell D, Larner J L, Benedict S H and Read P W 2010 Helical tomotherapy-based STAT stereotactic body radiation therapy: Dosimetric evaluation for a real-time SBRT treatment planning and delivery program *Med Dosim* 35 312-9
- Ehler E D, Nelms B E and Tome W A 2007 On the dose to a moving target while employing different IMRT delivery mechanisms *Radiother Oncol* 83 49-56
- Ehler E D and Tome W A 2008 Lung 4D-IMRT treatment planning: an evaluation of three methods applied to four-dimensional data sets *Radiother Oncol* 88 319-25
- Engelsman M, Damen E M, De Jaeger K, van Ingen K M and Mijnheer B J 2001 The effect of breathing and set-up errors on the cumulative dose to a lung tumour *Radiother Oncol* 60 95-105
- Evans P M, Coolens C and Nioutsikou E 2006 Effects of averaging over motion and the resulting systematic errors in radiation therapy *Phys Med Biol* 51 N1-7

- Fippel M 1999 Fast Monte Carlo dose calculation for photon beams based on the VMC electron algorithm *Med Phys* 26 1466-75
- Fippel M, Haryanto F, Dohm O, Nusslin F and Kriesen S 2003 A virtual photon energy fluence model for Monte Carlo dose calculation *Med Phys* 30 301-11
- Flampouri S, Jiang S B, Sharp G C, Wolfgang J, Patel A A and Choi N C 2006 Estimation of the delivered patient dose in lung IMRT treatment based on deformable registration of 4D-CT data and Monte Carlo simulations *Phys Med Biol* 51 2763-79
- Ford E C, Mageras G S, Yorke E and Ling C C 2003 Respiration-correlated spiral CT: a method of measuring respiratory-induced anatomic motion for radiation treatment planning *Med Phys* 30 88-97
- Gagne I M and Robinson D M 2004 The impact of tumour motion upon CT image integrity and target delineation *Med Phys* 31 3378-92
- Gagne I M, Robinson D M, Halperin R and Roa W 2005 The use of phase sequence image sets to reconstruct the total volume occupied by a mobile lung tumour *Med Phys* 32 2211-21
- Gibbs I C and Loo B W, Jr. 2010 CyberKnife stereotactic ablative radiotherapy for lung tumours *Technol Cancer Res Treat* 9 589-96
- Grutters J P, Kessels A G, Pijls-Johannesma M, De Ruyscher D, Joore M A and Lambin P 2010 Comparison of the effectiveness of radiotherapy with photons, protons and carbon-ions for non-small cell lung cancer: a meta-analysis *Radiother Oncol* 95 32-40
- Guckenberger M, Wilbert J, Meyer J, Baier K, Richter A and Flentje M 2007 Is a single respiratory correlated 4D-CT study sufficient for evaluation of breathing motion? *Int J Radiat Oncol Biol Phys* 67 1352-9
- Guo B, Xu X G and Shi C 2011 Real time 4D IMRT treatment planning based on a dynamic virtual patient model: proof of concept *Med Phys* 38 2639-50
- Hartmann G H 1995 Quality Assurance Program on Stereotactic Radiosurgery: Report from a Quality Assurance Task Group *Springer-Verlag*
- Heath E and Seuntjens J 2003 Development and validation of a BEAMnrc component module for accurate Monte Carlo modelling of the Varian dynamic Millennium multileaf collimator *Phys Med Biol* 48 4045-63
- Heath E and Seuntjens J 2006 A direct voxel tracking method for four-dimensional Monte Carlo dose calculations in deforming anatomy *Med Phys* 33 434-45
- Heath E, Seuntjens J, Keall P, Collins L and DeBlois F 2006 SU-FF-J-130: Validation of Non-Linear Image Registration-Based Correction Method for Motion Artifacts in 4D-CT *Med Phys (AAPM conference abstract)* 33
- Heath E, Tessier F and Kawrakow I 2011 Investigation of voxel warping and energy mapping approaches for fast 4D Monte Carlo dose calculations in deformed geometries using VMC++ *Phys Med Biol* 56 5187-202
- Heath E, Unkelbach J and Oelfke U 2009 Incorporating uncertainties in respiratory motion into 4D treatment plan optimization *Med Phys* 36 3059-71
- Henkelman R M and Mah K 1982 How important is breathing in radiation therapy of the thorax? *Int J Radiat Oncol Biol Phys* 8 2005-10
- Hodge W, Tome W A, Jaradat H A, Orton N P, Khuntia D, Traynor A, Weigel T and Mehta M P 2006 Feasibility report of image guided stereotactic body radiotherapy (IG-SBRT) with tomotherapy for early stage medically inoperable lung cancer using extreme hypofractionation *Acta Oncol* 45 890-6
- Horn B K P and Schunck B G 1981 Determining optical flow *Artificial Intelligence* 17 185-204
- Hsieh C H, Chang H T, Lin S C, Chen Y J, Wang L Y, Hsieh Y P, Chen C A, Chong N S, Lin S L, Chen C Y and Shueng P W 2010 Toxic risk of stereotactic body radiotherapy and concurrent helical tomotherapy followed by erlotinib for non-small-cell lung cancer treatment--case report *BMC Cancer* 10 696
- Huang T C, Liang J A, Dilling T, Wu T H and Zhang G 2010 Four-dimensional dosimetry validation and study in lung radiotherapy using deformable image registration and Monte Carlo techniques *Radiat Oncol* 5 45
- ICRU 1993 ICRU Report 50: Prescribing, Recording, and Reporting Photon Beam Therapy
- Jensen M D, Abdellatif A, Chen J and Wong E 2012 Study of the IMRT interplay effect using a 4DCT Monte Carlo dose calculation *Phys Med Biol* 57 N89-99

- Johns H E and Cunningham J 1983 *The Physics of Radiology* 4th edition *Charles C Thomas* 163
- Kawrakow I 2000 Accurate condensed history Monte Carlo simulation of electron transport. I. EGSnrc, the new EGS4 version *Med Phys* 27 485-98
- Kawrakow I and Fippel M 2000 Investigation of variance reduction techniques for Monte Carlo photon dose calculation using XVMC *Phys Med Biol* 45 2163-83
- Kawrakow I, Fippel M and Friedrich K 1996 3D electron dose calculation using a Voxel based Monte Carlo algorithm (VMC) *Med Phys* 23 445-57
- Kawrakow I, Rogers D W and Walters B R 2004 Large efficiency improvements in BEAMnrc using directional bremsstrahlung splitting *Med Phys* 31 2883-98
- Kawrakow I and Rogers D W O 2000 The EGSnrc Code System: Monte Carlo simulation of electron and photon transport *Technical report PIRS-701 NRC*
- Kawrakow I and Walters B R 2006 Efficient photon beam dose calculations using DOSXYZnrc with BEAMnrc *Med Phys* 33 3046-56
- Keall P J, Kini V R, Vedam S S and Mohan R 2001a Motion adaptive x-ray therapy: a feasibility study *Phys Med Biol* 46 1-10
- Keall P J, Mageras G S, Balter J M, Emery R S, Forster K M, Jiang S B, Kapatoes J M, Low D A, Murphy M J, Murray B R, Ramsey C R, Van Herk M B, Vedam S S, Wong J W and Yorke E 2006 The management of respiratory motion in radiation oncology report of AAPM Task Group 76 *Med Phys* 33 3874-900
- Keall P J, Siebers J V, Arnfield M, Kim J O and Mohan R 2001b Monte Carlo dose calculations for dynamic IMRT treatments *Phys Med Biol* 46 929-41
- Keall P J, Starkschall G, Shukla H, Forster K M, Ortiz V, Stevens C W, Vedam S S, George R, Guerrero T and Mohan R 2004 Acquiring 4D thoracic CT scans using a multislice helical method *Phys Med Biol* 49 2053-67
- Kessler M L, Pitluck S, Petti P and Castro J R 1991 Integration of multimodality imaging data for radiotherapy treatment planning *Int J Radiat Oncol Biol Phys* 21 1653-67
- Kim B, Chen J, Kron T and Battista J 2009 Motion-induced dose artifacts in helical tomotherapy *Phys Med Biol* 54 5707-34
- Kissick M W, Flynn R T, Westerly D C, Hoban P W, Mo X, Soisson E T, McCall K C, Mackie T R and Jeraj R 2008 On the impact of longitudinal breathing motion randomness for tomotherapy delivery *Phys Med Biol* 53 4855-73
- Kissick M W, Mackie T R and Jeraj R 2007 A delivery transfer function (DTF) analysis for helical tomotherapy *Phys Med Biol* 52 2355-65
- Kleshneva T, Muzik J and Alber M 2006 An algorithm for automatic determination of the respiratory phases in four-dimensional computed tomography *Phys Med Biol* 51 N269-76
- Kodak 2002 Radiographic film *Film digitizer manual*
- Kron T 1999 "Dose measuring tools" in *Modern technology of radiation oncology Medical Physics Publishing*
- Kuo J S, Yu C, Petrovich Z and Apuzzo M L 2003 The CyberKnife stereotactic radiosurgery system: description, installation, and an initial evaluation of use and functionality *Neurosurgery* 53 1235-9; discussion 9
- Langen K M, Meeks S L, Poole D O, Wagner T H, Willoughby T R, Kupelian P A, Ruchala K J, Haimeri J and Olivera G H 2005 The use of megavoltage CT (MVCT) images for dose recomputations *Phys Med Biol* 50 4259-76
- Lasserre J B 1983 An analytical expression and an algorithm for the volume of a convex polygon in  $R^n$  *J. Optim. Theory Appl.* 39 363-77
- Laub W, Alber M, Birkner M and Nusslin F 2000 Monte Carlo dose computation for IMRT optimization *Phys Med Biol* 45 1741-54
- Leow A, Huang S C, Geng A, Becker J, Davis S, Toga A and Thompson P 2005 Inverse consistent mapping in 3D deformable image registration: its construction and statistical properties *Inf Process Med Imaging* 19 493-503
- Li X A, Ma L, Naqvi S, Shih R and Yu C 2001 Monte Carlo dose verification for intensity-modulated arc therapy *Phys Med Biol* 46 2269-82
- Litzenberg D W, Hadley S W, Tyagi N, Balter J M, Ten Haken R K and Chetty I J 2007 Synchronized dynamic dose reconstruction *Med Phys* 34 91-102

- Liu H H, Verhaegen F and Dong L 2001 A method of simulating dynamic multileaf collimators using Monte Carlo techniques for intensity-modulated radiation therapy *Phys Med Biol* 46 2283-98
- Low D A, Nystrom M, Kalinin E, Parikh P, Dempsey J F, Bradley J D, Mutic S, Wahab S H, Islam T, Christensen G, Politte D G and Whiting B R 2003 A method for the reconstruction of four-dimensional synchronized CT scans acquired during free breathing *Med Phys* 30 1254-63
- Ma C-M, Reckwerdt P, Holmes M A, Rogers D W O, Geiser B and Walters B R 1996 DOSXYZ Users Manual *NRCC Report PIRS-0509B*
- Ma C M, Pawlicki T, Jiang S B, Li J S, Deng J, Mok E, Kapur A, Xing L, Ma L and Boyer A L 2000 Monte Carlo verification of IMRT dose distributions from a commercial treatment planning optimization system *Phys Med Biol* 45 2483-95
- Ma C M and Rogers D W O 1995 Beam characterization: a multiple-source model *Technical report PIRS-509d NRC*
- Mackie T R, Holmes T, Swerdloff S, Reckwerdt P, Deasy J O, Yang J, Paliwal B and Kinsella T 1993 Tomotherapy: a new concept for the delivery of dynamic conformal radiotherapy *Med Phys* 20 1709-19
- McGarry R C, Papiez L, Williams M, Whitford T and Timmerman R D 2005 Stereotactic body radiation therapy of early-stage non-small-cell lung carcinoma: phase I study *Int J Radiat Oncol Biol Phys* 63 1010-5
- Mechalacos J, Yorke E, Mageras G S, Hertanto A, Jackson A, Obcemea C, Rosenzweig K and Clifton Ling C 2004 Dosimetric effect of respiratory motion in external beam radiotherapy of the lung *Radiother Oncol* 71 191-200
- Miften M, Wiesmeyer M, Monthofer S and Krippner K 2000 Implementation of FFT convolution and multigrad superposition models in the FOCUS RTP system *Phys Med Biol* 45 817-33
- Monaco A, Caruso C, Giammarino D, Cianciulli M, Pressello M C and Donato V 2012 Radiotherapy for inoperable non-small cell lung cancer using helical tomotherapy *Tumouri* 98 86-9
- Murphy M J 2004 Tracking moving organs in real time *Semin Radiat Oncol* 14 91-100
- Murphy M J, Martin D, Whyte R, Hai J, Ozhasoglu C and Le Q T 2002 The effectiveness of breath-holding to stabilize lung and pancreas tumours during radiosurgery *Int J Radiat Oncol Biol Phys* 53 475-82
- Nakamura K, Shioyama Y, Nomoto S, Ohga S, Toba T, Yoshitake T, Anai S, Terashima H and Honda H 2007 Reproducibility of the abdominal and chest wall position by voluntary breath-hold technique using a laser-based monitoring and visual feedback system *Int J Radiat Oncol Biol Phys* 68 267-72
- NCI 2011 Cancer: Lung and Bronchus Incidence & Mortality <http://seer.cancer.gov/>
- NCIC 2011 Canadian Cancer Statistics
- Nehbrass J, Samsi S, Chaves J C, Unpingco J, Guilfoos B, Ahalt S, Krishnamurthy A, Chalker A and Gardiner J 2006 Interfacing PC-based MATLAB Directly to HPC Resources *Proceedings of the HPCMP Users Group Conference* 440-4
- Nioutsikou E, Richard N S-T J, Bedford J L and Webb S 2006 Quantifying the effect of respiratory motion on lung tumour dosimetry with the aid of a breathing phantom with deforming lungs *Phys Med Biol* 51 3359-74
- Niu C J, Foltz W D, Velec M, Moseley J L, Al-Mayah A and Brock K K 2012 A novel technique to enable experimental validation of deformable dose accumulation *Med Phys* 39 765-76
- Nohadani O, Seco J and Bortfeld T 2010 Motion management with phase-adapted 4D-optimization *Phys Med Biol* 55 5189-202
- Nuyttens J J, Prevost J B, Praag J, Hoogeman M, Van Klaveren R J, Levendag P C and Pattynama P M 2006 Lung tumour tracking during stereotactic radiotherapy treatment with the CyberKnife: Marker placement and early results *Acta Oncol* 45 961-5
- Oliver M, Gladwish A, Staruch R, Craig J, Gaede S, Chen J and Wong E 2008a Experimental measurements and Monte Carlo simulations for dosimetric evaluations of intrafraction motion for gated and ungated intensity modulated arc therapy deliveries *Phys Med Biol* 53 6419-36
- Oliver M, Staruch R, Gladwish A, Craig J, Chen J and Wong E 2008b Monte Carlo dose calculation of segmental IMRT delivery to a moving phantom using dynamic MLC and gating log files *Phys Med Biol* 53 N187-96

- Ong C, Verbakel W F, Cuijpers J P, Slotman B J and Senan S 2011 Dosimetric impact of interplay effect on RapidArc lung stereotactic treatment delivery *Int J Radiat Oncol Biol Phys* 79 305-11
- Otto K 2008 Volumetric modulated arc therapy: IMRT in a single gantry arc *Med Phys* 35 310-7
- Ozhasoglu C and Murphy M J 2002 Issues in respiratory motion compensation during external-beam radiotherapy *Int J Radiat Oncol Biol Phys* 52 1389-99
- Paganetti H 2004 Four-dimensional Monte Carlo simulation of time-dependent geometries *Phys Med Biol* 49 N75-81
- Paganetti H, Jiang H, Adams J A, Chen G T and Rietzel E 2004 Monte Carlo simulations with time-dependent geometries to investigate effects of organ motion with high temporal resolution *Int J Radiat Oncol Biol Phys* 60 942-50
- Pan T 2005 Comparison of helical and cine acquisitions for 4D-CT imaging with multislice CT *Med Phys* 32 627-34
- Panetti V, Wennberg B, Gagliardi G, Duch M A, Ginjaume M and Lax I 2007 SBRT of lung tumours: Monte Carlo simulation with PENELOPE of dose distributions including respiratory motion and comparison with different treatment planning systems *Phys Med Biol* 52 4265-81
- Papanikolaou N, Mackie T R, Meger-Wells C, Gehring M and Reckwerdt P 1993 Investigation of the convolution method for polyenergetic spectra *Med Phys* 20 1327-36
- Paskalev K 2002 Dosimetry of very small photon fields *M.Sc. Thesis (McGill University)*
- Peterhans M, Frei D, Manser P, Aguirre M R and Fix M K 2011 Monte Carlo dose calculation on deforming anatomy *Z Med Phys* 21 113-23
- Podgorsak E B 2003 Review of Radiation Oncology Physics : A Handbook for Teachers and Student *IAEA Educational Reports Series*
- Podgorsak E B and Podgorsak M B 1999 "Stereotactic irradiation" in Modern Technology of Radiation Oncology *Medical Physics Publishing*
- Popescu C C, Olivotto I A, Beckham W A, Ansbacher W, Zavgorodni S, Shaffer R, Wai E S and Otto K 2010 Volumetric modulated arc therapy improves dosimetry and reduces treatment time compared to conventional intensity-modulated radiotherapy for locoregional radiotherapy of left-sided breast cancer and internal mammary nodes *Int J Radiat Oncol Biol Phys* 76 287-95
- Ragan D, Starkschall G, McNutt T, Kaus M, Guerrero T and Stevens C W 2005 Semiautomated four-dimensional computed tomography segmentation using deformable models *Med Phys* 32 2254-61
- Rao M, Wu J, Cao D, Wong T, Mehta V, Shepard D and Ye J 2012 Dosimetric Impact of Breathing Motion in Lung Stereotactic Body Radiotherapy Treatment Using Image-Modulated Radiotherapy and Volumetric Modulated Arc Therapy *Int J Radiat Oncol Biol Phys*
- Rice R K, Hansen J L, Svensson G K and Siddon R L 1987 Measurements of dose distributions in small 6MV x-rays *Phys. Med. Biol.* 32 1087-99
- Rietzel E and Chen G T 2006 Deformable registration of 4D computed tomography data *Med Phys* 33 4423-30
- Rikner G and Grusell E 1986 General specifications for silicon semiconductors for use in radiation dosimetry *Phys. Med. Biol.* 32 1109-17
- Rogers D W, Faddegon B A, Ding G X, Ma C M, We J and Mackie T R 1995 BEAM: a Monte Carlo code to simulate radiotherapy treatment units *Med Phys* 22 503-24
- Rosenzweig K E, Hanley J, Mah D, Mageras G, Hunt M, Toner S, Burman C, Ling C C, Mychalczak B, Fuks Z and Leibel S A 2000 The deep inspiration breath-hold technique in the treatment of inoperable non-small-cell lung cancer *Int J Radiat Oncol Biol Phys* 48 81-7
- Rosu M, Chetty I J, Balter J M, Kessler M L, McShan D L and Ten Haken R K 2005 Dose reconstruction in deforming lung anatomy: dose grid size effects and clinical implications *Med Phys* 32 2487-95
- Rosu M, Chetty I J, Tatro D S and Ten Haken R K 2007 The impact of breathing motion versus heterogeneity effects in lung cancer treatment planning *Med Phys* 34 1462-73
- Ruchala K J, Olivera G H, Schloesser E A, Hinderer R and Mackie T R 2000 Calibration of a tomotherapeutic MVCT system *Phys Med Biol* 45 N27-36

- Russo J K and Rosen L 2011 TomoTherapy stereotactic body radiation therapy (SBRT) for the salvage treatment of locally recurrent esophageal adenocarcinoma following trimodality therapy: a case report *Tumouri* 97 406-10
- Saini A S and Zhu T C 2002 Temperature dependence of commercially available diode detectors *Med Phys* 29 622-30
- Salvat F, Fernandez-Varea J and Acosta E 2003 A code system for Monte Carlo simulation of electron and photon transport *Workshop Proc. Issy-les-Moulineaux France*
- Schaefer M, Munter M W, Thilmann C, Sterzing F, Haering P, Combs S E and Debus J 2004 Influence of intra-fractional breathing movement in step-and-shoot IMRT *Phys Med Biol* 49 N175-9
- Schweikard A, Glosser G, Bodduluri M, Murphy M J and Adler J R 2000 Robotic motion compensation for respiratory movement during radiosurgery *Comput Aided Surg* 5 263-77
- Seco J, Sharp G C, Turcotte J, Gierga D, Bortfeld T and Paganetti H 2007 Effects of organ motion on IMRT treatments with segments of few monitor units *Med Phys* 34 923-34
- Seppenwoolde Y, Shirato H, Kitamura K, Shimizu S, van Herk M, Lebesque J V and Miyasaka K 2002 Precise and real-time measurement of 3D tumour motion in lung due to breathing and heartbeat, measured during radiotherapy *Int J Radiat Oncol Biol Phys* 53 822-34
- Shimamoto S, Inoue T, Shiomi H, Sumida I, Yamada Y and Tanaka E 2002 CyberKnife stereotactic irradiation for metastatic brain tumours *Radiat Med* 20 299-304
- Shimizu S, Shirato H, Kagei K, Nishioka T, Bo X, Dosaka-Akita H, Hashimoto S, Aoyama H, Tsuchiya K and Miyasaka K 2000 Impact of respiratory movement on the computed tomographic images of small lung tumours in three-dimensional (3D) radiotherapy *Int J Radiat Oncol Biol Phys* 46 1127-33
- Shirato H, Seppenwoolde Y, Kitamura K, Onimura R and Shimizu S 2004 Intrafractional tumour motion: lung and liver *Semin Radiat Oncol* 14 10-8
- Siebers J V, Keall P J, Nahum A E and Mohan R 2000 Converting absorbed dose to medium to absorbed dose to water for Monte Carlo based photon beam dose calculations *Phys Med Biol* 45 983-95
- Siebers J V and Zhong H 2008 An energy transfer method for 4D Monte Carlo dose calculation *Med Phys* 35 4096-105
- Sikora M, Dohm O and Alber M 2007 A virtual photon source model of an Elekta linear accelerator with integrated mini MLC for Monte Carlo based IMRT dose calculation *Phys Med Biol* 52 4449-63
- Solberg T D, DeMarco J J, Holly F E, Smathers J B and DeSalles A A 1998 Monte Carlo treatment planning for stereotactic radiosurgery *Radiother Oncol* 49 73-84
- Spencer L V and Attix F H 1955 A theory of cavity ionization *Radiat. Res.* 3 239
- Spezi E, Lewis D G and Smith C W 2002 A DICOM-RT-based toolbox for the evaluation and verification of radiotherapy plans *Phys Med Biol* 47 4223-32
- Sterpin E, Salvat F, Cravens R, Ruchala K, Olivera G H and Vynckier S 2008 Monte Carlo simulation of helical tomotherapy with PENELOPE *Phys Med Biol* 53 2161-80
- Sterzing F, Uhl M, Hauswald H, Schubert K, Sroka-Perez G, Chen Y, Lu W, Mackie R, Debus J, Herfarth K and Oliveira G 2010 Dynamic jaws and dynamic couch in helical tomotherapy *Int J Radiat Oncol Biol Phys* 76 1266-73
- Stock M, Kontrisoova K, Dieckmann K, Bogner J, Poetter R and Georg D 2006 Development and application of a real-time monitoring and feedback system for deep inspiration breath hold based on external marker tracking *Med Phys* 33 2868-77
- Thirion J P 1998 Image matching as a diffusion process: an analogy with Maxwell's demons *Med Image Anal* 2 243-60
- Tomita N, Kodaira T, Matsuo M, Furutani K, Tachibana H, Daimon T and Shimizu H 2010 Helical tomotherapy for solitary lung tumour: feasibility study and dosimetric evaluation of treatment plans *Technol Cancer Res Treat* 9 407-15
- Tomotherapy 2011 Field safety notice 5089
- Tyldesley S, Boyd C, Schulze K, Walker H and Mackillop W J 2001 Estimating the need for radiotherapy for lung cancer: an evidence-based, epidemiologic approach *Int J Radiat Oncol Biol Phys* 49 973-85

- Vaandering A, Lee J A, Renard L and Gregoire V 2009 Evaluation of MVCT protocols for brain and head and neck tumour patients treated with helical tomotherapy *Radiother Oncol* 93 50-6
- Vahdat S, Oermann E K, Collins S P, Yu X, Abedalthagafi M, Debrito P, Suy S, Yousefi S, Gutierrez C J, Chang T, Banovac F, Anderson E D, Esposito G and Collins B T 2010 CyberKnife radiosurgery for inoperable stage IA non-small cell lung cancer: 18F-fluorodeoxyglucose positron emission tomography/computed tomography serial tumour response assessment *J Hematol Oncol* 3 6
- Van de Walle J, Martens C, Reynaert N, Palmans H, Coghe M, De Neve W, De Wagter C and Thierens H 2003 Monte Carlo model of the Elekta SLiplus accelerator: validation of a new MLC component module in BEAM for a 6 MV beam *Phys Med Biol* 48 371-85
- van Herk M and Kooy H M 1994 Automatic three-dimensional correlation of CT-CT, CT-MRI, and CT-SPECT using chamfer matching *Med Phys* 21 1163-78
- Vanderstraeten B, Reynaert N, Paelinck L, Madani I, De Wagter C, De Gerssem W, De Neve W and Thierens H 2006 Accuracy of patient dose calculation for lung IMRT: A comparison of Monte Carlo, convolution/superposition, and pencil beam computations *Med Phys* 33 3149-58
- Verhaegen F and Liu H H 2001 Incorporating dynamic collimator motion in Monte Carlo simulations: an application in modelling a dynamic wedge *Phys Med Biol* 46 287-96
- Vinogradskiy Y Y, Balter P, Followill D S, Alvarez P E, White R A and Starkschall G 2009 Verification of four-dimensional photon dose calculations *Med Phys* 36 3438-47
- Waghorn B J, Meeks S L and Langen K M 2011 Analyzing the impact of intrafraction motion: correlation of different dose metrics with changes in target D95% *Med Phys* 38 4505-11
- Waghorn B J, Shah A P, Ngwa W, Meeks S L, Moore J A, Siebers J V and Langen K M 2010 A computational method for estimating the dosimetric effect of intra-fraction motion on step-and-shoot IMRT and compensator plans *Phys Med Biol* 55 4187-202
- Webb S, Bortfeld T, Stein J and Convery D 1997 The effect of stair-step leaf transmission on the 'tongue-and-groove problem' in dynamic radiotherapy with a multileaf collimator *Phys Med Biol* 42 595-602
- Wilkins D, Li X A, Cygler J and Gerig L 1997 The effect of dose rate dependence of p-type silicon detectors on linac relative dosimetry *Med Phys* 24 879-81
- Wu J, Lei P, Shekhar R, Li H, Suntharalingam M and D'Souza W D 2009 Do tumours in the lung deform during normal respiration? An image registration investigation *Int J Radiat Oncol Biol Phys* 75 268-75
- Yang D, Brame S, El Naqa I, Aditya A, Wu Y, Goddu S M, Mutic S, Deasy J O and Low D A 2011a Technical note: DIRART--A software suite for deformable image registration and adaptive radiotherapy research *Med Phys* 38 67-77
- Yang D, Li H, Low D A, Deasy J O and El Naqa I 2008 A fast inverse consistent deformable image registration method based on symmetric optical flow computation *Phys Med Biol* 53 6143-65
- Yang W, Jones R, Lu W, Geesey C, Benedict S, Read P, Larner J and Sheng K 2011b Feasibility of non-coplanar tomotherapy for lung cancer stereotactic body radiation therapy *Technol Cancer Res Treat* 10 307-15
- Yu C X, Jaffray D A and Wong J W 1998 The effects of intra-fraction organ motion on the delivery of dynamic intensity modulation *Phys Med Biol* 43 91-104
- Zhao Y L, Mackenzie M, Kirkby C and Fallone B G 2008 Monte Carlo calculation of helical tomotherapy dose delivery *Med Phys* 35 3491-500
- Zhong H and Siebers J V 2009 Monte Carlo dose mapping on deforming anatomy *Phys Med Biol* 54 5815-30